MICRO-NEUROCIRCUITRY: MODELING BRAIN CIRCUITRY WITH INDUCED NEURONS FOR THE STUDY OF NEUROPSYCHIATRIC DISORDERS

By

JOSEPH ANDREW FANTUZZO

A dissertation submitted to the

School of Graduate Studies

Rutgers, The State University of New Jersey

In partial fulfillment of the requirements

For the degree of

Doctor of Philosophy

Graduate Program in Biomedical Engineering

Written under the direction of

Dr. Jeffrey Zahn

And approved by

_____

_____

_____

_____

_____

_____

New Brunswick, New Jersey

January 2018

ABSTRACT OF THE DISSERTATION

Micro-neurocircuitry: modeling brain circuitry with induced neurons for the study of neuropsychiatric disorders

By JOSEPH ANDREW FANTUZZO

Dissertation Director:

Dr. Jeffrey Zahn

Neuropsychiatric disorders which target defined neural circuits in the brain have been difficult to treat, due to the complexity of the human brain and inaccessibility to tissue for study. As a result, there has been a dearth of successful pharmaceutical therapies available to treat these disorders, which is largely due to inadequate predictive models of efficacy. Human iPSC-derived neurons hold promise as one such system, but to date have been primarily used in single neuronal population studies focused toward unraveling complex neurological disease mechanisms and genetic studies. While this is an important step toward the goal of better therapeutic development, these cell cultures have been removed from their neural circuit contexts, which may also remove important disease endophenotypes which can only be seen in circuit models. We have therefore developed microfluidic-based circuit models using human neurons which can capture certain aspects of these neural circuits. These microdevices are designed for compartmentalization of distinct neuronal sub-

types, resembling the connections between varying brain nuclei. Here, we demonstrate that human induced neurons establish functional synaptic contacts and exhibit circuit network activity within and between device compartments. These circuits can be excited by small molecules or optogenetics and altered using receptor antagonists, and their functional activity measured by either patch clamp or calcium imaging. Furthermore, we have developed additional computational tools which aid in the processing of large amounts data, thereby accelerating the interpretation of data and facilitating high-throughput screening studies.

ACKNOWLEDGEMENTS

I would like to thank my advisor Dr. Jeffrey Zahn for his support and guidance during my graduate school career. I would also like to thank Drs. Zhiping Pang and Ronald Hart who brought me in as extended lab members, and shared their time and resources with me for these projects. Thank you also to my committee members: Dr. Li Cai, Dr. Bonnie Firestein, and Dr. Prabhas Moghe.

Lastly, I would like to thank my funding sources: The National Institute on Drug Abuse grants: DA035594 and DA039686.

DEDICATION

This work is dedicated to:

My wife, Rebecca, whose love and support are greatly appreciated, and who shared in my struggles and successes over the past few years

and

SSgt Christopher R. Goski and SFC Michael J. Goski, twin brothers in the U.S. military who were affected by the trauma of their experiences and the pharmacological treatments offered to them. May our growing understanding of the brain and psychiatric treatments better serve those who serve our country.

TABLE OF CONTENTS

LIST OF TABLES

LIST OF FIGURES

CHAPTER 1: INTRODUCTION

Neuropsychiatric disorders, which are disorders focused on the brain and its function, often have devastating effects. From minor behavioral changes to physical abuse of loved ones, these symptoms have a substantial impact on the lives and relationships of those suffering from them. Due to the complexity of these disorders and the challenge thus far to study disorder onset and progression in human patients, many with these disorders have little successful and long-lasting therapeutic options available. In addition to personal effects, these disorders also have a substantial societal and economic burden. Between direct and indirect costs, there is a global financial burden of $2.5 trillion, as estimated in 2010,[4] and make up 40% of all lost years due to disability in North America and Europe.[5] Furthermore, disease incidence is on the rise[6], which will eventually lead to increases in these costs. Treatments have been scarce, primarily because the diseases can be difficult to diagnose and the mechanisms difficult to understand. Do all diseases have principally a genetic etiology, or are their etiologies behavioral or socially-meditated, or a combination? It is often difficult to understand, due to the complexity of the human brain, and since disease onset can be brought about through different means. For example, disorders occur after injury (as in traumatic brain injury), viral infection[7], or existing with genetic code from birth.[5,8] While pharmacological or behavioral interventions exist in addition to pharmacological treatments in some cases, many diseases still lack a lasting treatment, or, due to patient-to-patient variability, do not work for all.[5] This highlights the need for improved modeling systems, leading to

greater understanding of the pathogenesis and mechanisms of disease, and eventually to personalized medicine. While animal models have played a role in drug development, no single animal model can adequately account for the complexity of the human brain and appropriately deal with species differences in such as a way as to improve therapeutic predictive outcomes.[6, 9] Therefore, to facilitate therapeutic development, there is a demand for a greater understanding of CNS disease pathology in human and adequate modeling paradigms for study. This of course requires a greater understanding of how the human brain functions generally.

The human brain is a complex network of neurons and glia, which interact between brain regions to form neural circuits. Diseases and disorders of the brain affect the function of neural circuits, which ultimately impacts behavior. These neurons exist in distinct brain regions and as many different subtypes. Distinct brain regions are usually dominated by a large population of one subtype, which is defined by the type of neurotransmitter released. Excitatory neurons release glutamate and inhibitory neurons typically release GABA as their neurotransmitter. Other neurons, such as dopaminergic neurons release dopamine, and serve as modulators of their circuit. Indeed, there are many other subtypes which contribute to the complex network of neural circuits. Together, these different neurons provide a strict control and balance of the function of the brain, complete with feedback systems to regulate neuronal firing. While the functional unit of the brain remains the neuron, newer insight into brain function suggests that groups of neurons or neuronal ensembles, functioning as a unit, provide almost an equally basic function for the brain.[10] Circuit studies have grown in importance[11], notably when trying to un-

derstand their role in psychiatric disorders such as autism, schizophrenia, or substance abuse. While the understanding of neural circuits has grown in popularity, many researchers focus on more basic questions of neuronal function as it relates to genetics.

Genetics of psychiatric disorders

When considering the onset of neuropsychiatric diseases, etiology is not always clear, but genetics has taken a primary role. Prompted by observations of heritability between siblings and twins, researchers have placed a focus on the role of genetic variation.[12-14] Studies have shown that there is indeed a relationship between certain diseases, e.g., autism[15] and schizophrenia,[16] and familial penetrance, which flags the genome as a key element in disease onset. The sequencing of the human genome and novel sequencing techniques enable greater investigation into the role of polymorphisms and genetic variation. Genome-wide association studies (GWAS) have identified potential mutations that may provide links between disease and phenotype, and which may also identify genes which mediate risk for certain disorders.[17] Genomic sequencing of patients with psychiatric disorders has demonstrated links between neuronal genes and genetic variation, but there are many cases where a risk gene is found only in one twin or sibling[5] or where the genetic mutation from birth is not enough to bring about disease, suggesting that there is a role for *de novo* mutations as well. In order to understand how genetics play a role and the impact a particular gene or variant has on a neural circuit, human neurons should serve as the ideal model system for *in vitro* studies.

Until the advent of stem cell technology, these resources have been difficult to come by, and animal models have been the primary source of intact neural circuits as well as the behavioral paradigm for neuropsychiatric disorder studies. A great deal of progress has been made through the study of animal models in understanding the function of disorder in neural circuits—particularly when the genetic targets have human homologs, as in the case of neuroligin-3 and autism.[18, 19] Clever experimental approaches have also been put to use to regulate genes of interest, e.g., use of Cre recombinase to turn specific genes on and off. Links between a particular gene and its function within a developing or fully developed neural circuit have begun to be established, however the full impact a mutation has on a population of neurons within a circuit context has been difficult to elucidate, primarily due to the complexity of the human brain, prompting the need to not only continue genetic studies, but investigate how these affected genes alter the neural circuits of which they are a part. The question then becomes, how can we maximize the value obtained through neurogenomics and/or patient-specific cell lines to advance our understanding of neuropsychiatric disorders? The answer has focused toward investigation of single neuronal subtypes, and more recently, incorporation of these subtypes into functional circuit models.

Effects of psychiatric disorders on neural circuits

Understanding the function of neural circuits has gone hand-in-hand with the development of new techniques, such as optogenetics[20, 21] and neuroimaging.[5] These techniques, discussed below, enable researchers to probe different regions of the brain and investigate circuit-level effects. Neurons existing in a circuit add fur-

ther complexity to the study of neuropsychiatric disorders, which affect not only single populations of neurons, but also the circuits of which those neurons are a part.[22, 23] Much of what is known about psychiatric disorders has been studied in animal models, where intact circuits can be manipulated either through optogenetics or electrophysiological methods.[24] For example, drug addiction and substance abuse is a disorder of the reward pathway, namely, the mesolimbic dopamine pathway, which is comprised of connections primarily from the nucleus accumbens (NAc), ventral tegmental area (VTA), and the prefrontal cortex (PFC) (Figure 1.1).[22, 25, 26] Most drugs of abuse increase the levels of dopamine in the NAc, which has downstream circuit effects on the reward pathway. Substance abuse targeting one of these brain regions re-wires the circuit toward impaired reward evaluation, prompting additional abuses through compulsive relapse.[22] Synaptic plasticity also plays a role as it changes synaptic structure to alter and to further lock in place the effects of a disordered circuit. These plastic changes make recovery more difficult, and, in the case of drug addiction, lead to relapse and withdrawal. These elements of plasticity and propagating circuit effects is not exclusive to addiction, but impact many different neuropsychiatric disorders. In these cases, transient improvements through pharmacological intervention may be achieved, but often therapies lose efficacy throughout the treatment process, as the targeted circuit likely readapts to accommodate the change. The pharmaceutical target therefore is always moving and has presented a vast challenge for the industry.

Drug addiction as a neuropsychiatric disorder: altered learning

Focusing on drug addiction as a circuit-level disorder, it is best defined as a state of compulsive drug seeking and abuse.[26] When considering drug addiction or substance abuse, a disordered state is produced as a progression toward a diseased state, that is, as the addict engages in substance abuse, the disorder progresses further toward a more permanent state.[22] Indeed, there are risk factors that have been implicated in drug addiction,[27-29] but neither these plus *de novo* mutations can alone produce the disordered state of drug addiction. The onset of drug addiction is best understood as a choice of the addict to engage in drug abuse. Many have partaken in substance abuse, but drugs do not affect all

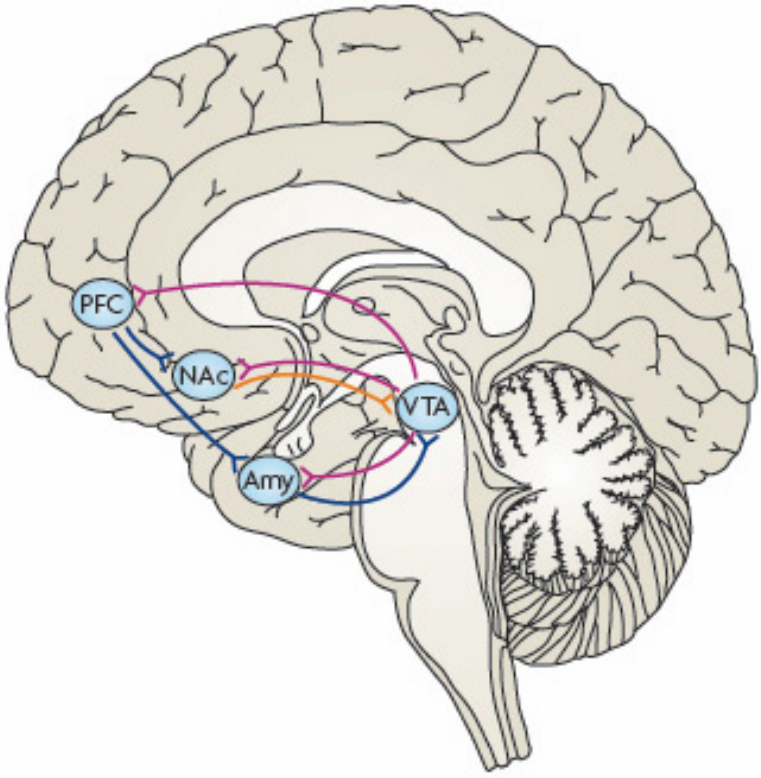

Figure 1.1. Mesolimbic dopamine pathway. The mesolimbic dopamine pathway, also called the reward pathway, is comprised of the prefrontal cortex, nucleus accumbens, ventral tegmental area, and amygdala. Projections from these nuclei form the reward circuit, which is targeted in substance abuse and eating disorders. (Figure used with permission. Source: Eric Nestler, M.D., Mount Sinai School of Medicine.)[25]

users equivalently. Here, risk variants may play a role, moving an abuser much more quickly toward the disordered state (a state characterized by compulsive relapses) than an abuser without the variant. When the abuser has come under a state of compulsive relapses and frequent drug seeking, this is the hallmark of addiction and it is considered a neuropsychiatric disorder.

As mentioned above, drugs of abuse target the mesolimbic dopamine pathway, which mediates reward processing.[23, 30] Through a variety of mechanisms, almost all drugs result in the increase of dopaminergic tone in the nucleus accumbens (NAc). The NAc receives inputs from prefrontal cortex, ventral tegmental area, and amygdala, and it likewise projects back outward to these nuclei. Animal models targeting this pathway have been successful in demonstrating various aspects of the addicted phenotype, such as drug seeking and withdrawal,[31] but no model to date has been capable of reproducing all aspects of the human disorder. The best approach may be a combination of animal model and *in vitro* models.

Industrial departure from neuropsychiatric disease research and development

After substantial failure to produce efficacious pharmaceutical interventions, there has been a gradual departure of the pharmaceutical industry from pursing psychiatric drugs remedies. As most drugs can cost up to a billion dollars to produce, lack of clinical translation and production of blockbusters has given psychiatric targets a negative outlook in the eyes of investors. Current animal models unfortunately have demonstrated low predictive power for developing therapeutics[9], as both symptom and treatment can be hard to define in animals. While there have been successes in rodent models, many of these fail to demonstrate efficacy in

human clinical trials.[32] As a result, the pharmaceutical industry over the past decade has reduced CNS drug candidates in their pipelines due to the lack of translation of candidates into the market.[6, 33, 34] With decreased investment from the pharmaceutical industry into neuropsychiatric disease treatments, how then can we bridge the gap between this decreasing interest on the one hand and increasing incidence of disease on the other? Great progress can be made to address this discrepancy by the pursuit of disease mechanism and through generation of better predictive models of drug efficacy[33], however there is much more to accomplish to improve these therapeutic outcomes.

Animal models for therapeutic development

To understand how best to bridge the gap, it is important to know what animal models can and cannot offer. Animal models are excellent sources of information for pathology and drug development, and have greatly aided in the generation of many therapeutics in non-psychiatric disorders. For psychiatric disorders, there is a bit more complexity due to the differences between the animal and the human brain and due to a lack of understanding of human brain function. Therefore, careful experimental setup must be performed so as not to over-interpret or misjudge results. Since psychiatric disorders alter behavior, behavioral-based models can yield insight into shared molecular mechanisms which produce a specific behavioral change. Neuroethology, that is, selection of an appropriate model system, must be performed carefully in order to provide the most meaningful result. Researchers typically consider three different types of validity for establishing and choosing appropriate animal model systems. The first is face validity, which based

on the comparison of the animal behavior to the human behavior. High face validity means that the behaviors are highly similar.[35] Face validity can work for many behaviors such as fear or anxiety, but are often difficult for other symptoms (e.g., sadness) or are non-existent or at least not measureable in animals (e.g., suicidal thoughts/actions).[9] Construct validity, that is, recapitulation of the etiology of a disease between model and human[35] also has its challenges. Central to the concern over construct validity is an adequate understanding of disease pathology in the first place. The nature and influence of certain risk genes, the presence of these genes in animal models, and the underlying circuitry must first be more greatly elucidated in order to determine the extent of construct validity offered by a given model.[9] Lastly, predictive validity refers to the ability of a model to predict the physiological response of a drug in human. It is this last validity type which has been lacking in animal models of neuropsychiatric disorders, much to the frustration and chagrin of the pharmaceutical industry. While there have been cases of success, there has been a large withdrawal of the industry from neuropsychiatric disorder therapeutic research due to clinical failure. Surely, greater understanding of disease mechanism and affected circuitry will improve the generation and validation of animal models. It is not easy to pinpoint exactly why animal models have not been useful for psychiatric disease modeling, but it may be due simply to species differences. Ultimately, animal models play a role in revealing a portion of the picture of neuropsychiatric disease mechanism and its connection to behavior, but researchers have also begun to pursue other cellular models of disease, which can be more "humanized".

Stem cells as a model for disease mechanism and screening

Since the discovery of the Yamanaka factors[36, 37], induced pluripotent stem cells (iPSCs) have provided promising opportunity for health care and drug development. The potential for stem cells to be used as a modeling platform has been extensively reviewed.[38-44] Differing induction protocols allow researchers to produce many difference cell types, from direct conversion to mature neurons[45-47] to progression through a progenitor stage, enabling the study of developmental disorders.[48] Human-based neuronal cells allow researchers to focus on the role of specific human genes and proteins in mediating disease phenotypes (Figure 1.2). Furthermore, mechanism is more easily studied in controlled, *in vitro* systems than in complex animal models. Mechanistic studies have provided additional insight into the formation of disordered states, but most studies are limited to 2D culture systems which do not preserve intact brain circuitry. These mechanistic studies indeed serve an important role to understand how human cell lines with known genetic background can be altered in a disordered state, but there may be circuit-level phenotypes that are lost within the system. To better utilize stem cells for disease modeling, novel approaches, circuit designs can be produced to fully harness the modeling power of iPSCs.

Tools for research

In vivo model systems certainly have their advantages, namely, intact brain circuits, a full physiological system, and importantly, for behavioral disorders, an animal that behaves and can thus be studied in that manner. Animal models however can be complex to generate and expensive to maintain. An advantage of *in*

vitro systems on the other hand is their ease of use and generally low cost. Furthermore, dissociated neurons can be cultured in clever devices designed to capture various aspects of cellular function that is difficult to draw out from animal models

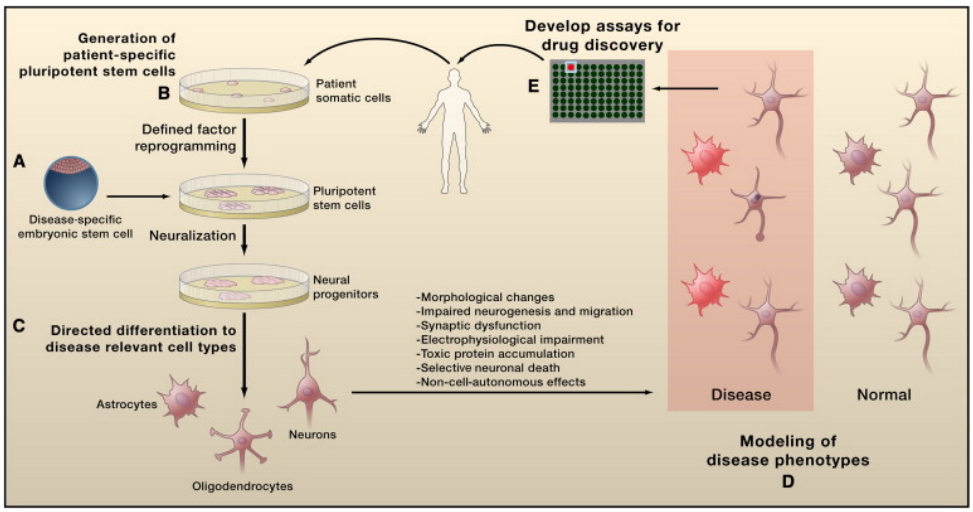

Figure 1.2. Stem cell modeling as a tool for therapeutic discovery. Stem cells can be obtained from both disease-presenting or healthy individuals and transformed into neurons for construction of cellular models. Embryonic or somatic cells induced into stem cells (induced pluripotent stem cells) are transformed into a variety of lineages for modeling. Here, diseased, that is, cells possessing an abnormal phenotype and normal cells can be compared, and novel drugs can be screened against the two different cell lines. Ultimately, this provides a personalized treatment opportunity for therapeutic development. (Figure reproduced with permission from Han et al. 2011.)[49]

or slice cultures. The advent of optogenetic and chemogenetic tools further facilitates the ability of the researcher to probe neuronal cultures for aberrant (or normal) functional activity.

Optogenetics is a technique that uses light as a means of stimulation. Photosensitive ion channels, isolated from green algae, can function as optical triggers of neuronal activity.[50-53] For example, channel-rhodopsin 2 (ChR2) is an ion channel that, in the presence of blue light (470 nm), opens and causes neuronal depolarization. This approach has been advantageous for *in vivo* work, enabling researchers to alter animal behavior with light, and to do so through manipulations of specific

brain regions. Distinct cells are infected with virus expressing ChR2 (or other opsins) and, at precise times defined by the experimenter, a population of neurons can be stimulated. Furthermore, when the opsin gene is combined with *in vivo* Cre-recombinase strategy, only distinct cell populations with a floxed opsin gene coupled to Cre-recombinase will express the protein, facilitating the elucidation of distinct circuit connections within animal models.[54] This approach can be used *in vitro* also. In the area of compartmentalized cultures, neuronal populations can be stimulated with light to provide signals between chambers.[1, 2] Optogenetics therefore provides a useful tool for the development of such circuits, and allows spatiotemporal control over distinct cellular populations.

As an analogous approach, chemogenetics can be utilized for stimulation of subpopulations of neurons. Most notably, a series of G-protein coupled receptors called designer-receptors-exclusively-activated-by-designer-drugs (DREADDs) have been developed and present a unique opportunity for controlling cells with small molecules.[55] One such example, hM3D (a mutant human muscarinic type 3 receptor) protein was altered to be inert to all endogenous stimulation. This rendered an ion channel which could only be opened in the presence of unique, non-endogenous small molecules, in this case, Clozapine-N-oxide (CNO)[56] or Compound 21. While this approach initially grew in popularity for *in vivo* studies[57-59], researchers have begun to move away from it due to new data suggesting that CNO does not directly stimulate cells *in vivo*, but rather does so through its conversion to Clozapine.[60] Clozapine is known to have affinity for other receptors as well as a high affinity for hM3D, and therefore high concentrations of CNO, metabolizing

into its derivative Clozapine, may generate non-specific neuronal targeting.[61] While this has important consequences for *in vivo* studies, DREADD technology as a tool may still be useful for *in vitro* studies, where CNO metabolism, conversion, and non-specific Clozapine activation is less likely to occur on a time scale with direct CNO activity. There are, however, few reports of using DREADD technology for *in vitro* cultures.[62, 63] In spite of recent skepticism, chemogenetics, along with optogenetics, provide novel opportunity for stimulation of neuronal circuits, and offer precise spatial and temporal control within model systems.

In addition to molecular tools for probing neural circuits, a number of mechanical/electrical techniques have been developed to aid in the unraveling of neuronal communication. Of particular interest is the role multi-electrode arrays (MEAs) have played as a means of tracking functional activity in an active circuit *in vitro*.[64-68] The MEA setup exists as an array of electrode pads patterned underneath a culture surface. Neurons growing, projecting axons, and firing action potentials on top of the electrode pads provide local depolarizations, which are then recorded by the electrodes. Each electrode can be recorded individually, allowing the experimenter to collect network information of the neuronal culture, with both spontaneous and synchronous events.[69] Multi-electrode arrays have the advantage of providing easily accessible, non-invasive functional data that is analogous to electrophysiology and does not require the addition of fluorophores, as in calcium imaging. On the other hand, MEAs are not scalable, as it is difficult to provide enough access for wires for all electrode pads. Furthermore, MEAs can be expensive, which also makes high-throughput studies difficult to perform.

With respect to capturing network activity, calcium imaging, both through calcium indicators such as Fluo-4 and more recently, genetically-encoded calcium indicators (GECIs), have been widely used.[1, 70-73] In these cases, intracellular calcium is used as a proxy for neuronal activity. Calcium imaging offers better spatial control than MEAs, provided that the regions of interest (ROIs) are properly identified. The time resolution can also be set as fast as a camera can capture a frame, allowing the experimenter to dissect out single action potentials.[74] Along with MEAs, calcium imaging also offers the advantage of ability to screen circuit activity. Multiple cells within the imaging field can all be monitored simultaneously, which conveys both spatial and temporal information. Additionally, many automated analysis systems have been developed to fast-track data analysis.[75-77]

Indeed, there are many tools available for *in vitro* neural circuit studies. These tools either serve to stimulate circuits (opto- and chemo-genetics) or readout the data (MEAs and calcium imaging). As the question of how to set up these circuits in a compartmentalized format, most have turned to using microfluidic technology to development such systems.

Microfluidics as a tool for circuit modeling

Earliest compartmentalized devices utilized a plastic divider combined with microgrooves scratched into the culture surface.[78-80] These devices, known as Campenot chambers, are still used today[81], but they do not offer the same level of design and reproducibility as do devices produced from soft lithography. Researchers have utilized soft lithography to take advantage of neuron structure, where projecting processes can be isolated from somata through the creation of

lithographically-defined microchannels. These microchannels have a reduced height, typically 3 μm, which significantly inhibits the entry of cell bodies, while allowing neurites to travel through the microchannels. This concept was first introduced by the work of Taylor et al. in 2003 by the Jeon lab at University of California Irvine (Figure 1.3).[82, 83] This work demonstrated a two-layer lithographic process that defined both microchannels for axonal outgrowth and compartments for cell bodies. While these investigators were primarily interested in producing an axonal injury model, this approach has been widely used to produce 2D compartmentalized systems.[1, 2, 84-88] With regard to questions focused on modeling neural circuits, the task has been more daunting, as there are additional features to consider.

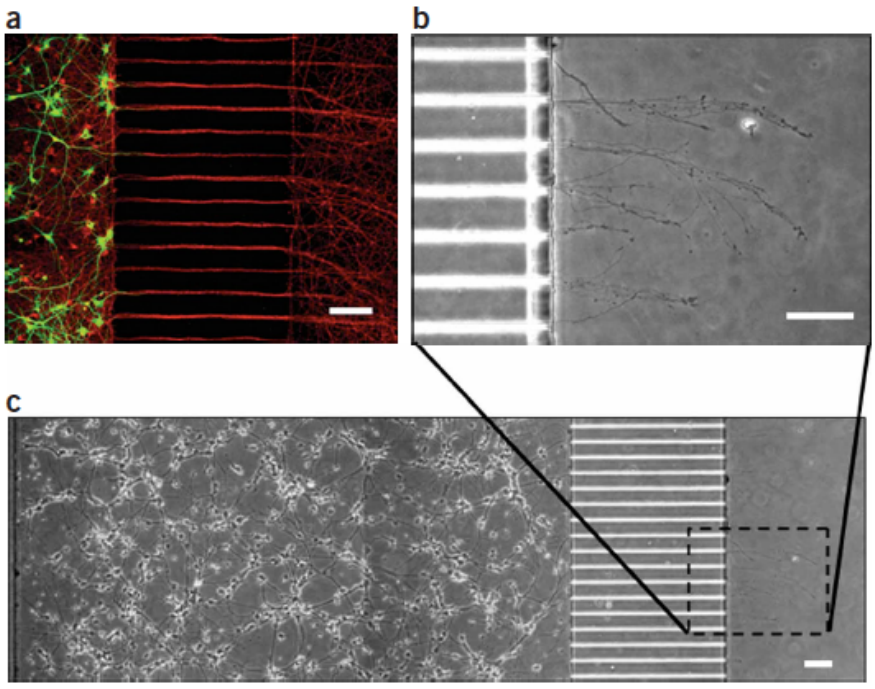

Figure 1.3. Microchannels as an approach for neuronal compartmentalization. This approach, originally designed from the Jeon group at UC Irvine, used photolithography to produce compartmentalization, where in neurons can project axons from one compartment to the other. As shown, dendrites are retained in the source compartment, as the microchannel length is too long to traverse. (Figure reproduced with permission from Park et al. 2006.)[82]

One recent review covers some of the various techniques researchers have used to address the complex formation of neural circuits on a chip.[89] Researchers have demonstrated the ability to segregate neuronal populations either by micropatterning[i] or through physical devices produced through soft lithography. Micropatterned compartmentalized devices have shown differences between neuronal segregation and random mixed culture[90, 91], and can provide the benefit of quick replication molding, but over time, projecting processes may extend across barriers in unintended ways.[92] Researchers have also realized the utility for constructing directionality in circuit models. Directional models are constructed using the micro channel approach rather than the stamping approach, since 3D lithographic structures offer clever and unique means of allowing axonal projections to travel in one direction rather than the other. One simple way to provide directionality is to seed one population of neurons in a compartment before the other.[2, 93] This allows one population of neurons to largely fill the volume of the microchannels before the other population is able to. Similarly, this may also be the case in neurons which mature at different rates. GABA-ergic induced neurons appear to mature more slowly, and thus are outcompeted by faster-maturing neurons, such as excitatory induced neurons.

Directionality though can be established using clever lithography design (Figure 1.4). Tapered channels known as "Axon Diodes" have been developed, stochastically reduce the number of axons entering a narrow channel on the one

[i] Using microfluidics, regions of distinct surface chemistries can be achieved which provide specific cell attachment sites. Non-favorable surface chemistries for cell attachment provide barriers for cellular interaction, and therefore segregate cultures to defined areas.

side, but increase entry on the channel's wider end.[88] Additionally, an axonal edge guidance approach has been devised, where one side is permitted a free path to the other side, but axons from the other chamber are presented with returning channels

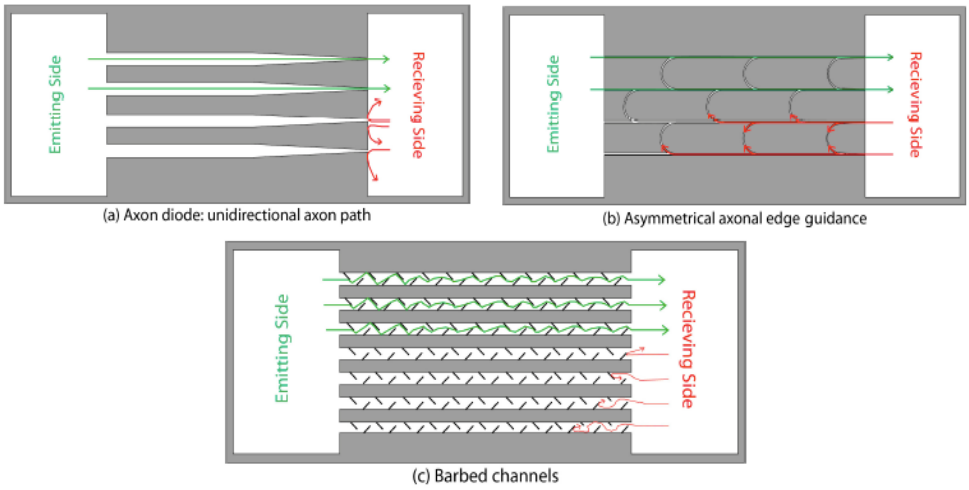

Figure 1.4. Directionality techniques in compartmentalized circuit models. These three approaches provide directionality in circuit models. (a) Axon diodes mitigate entry of processes from the receiving side by making channel entry more difficult. (b) Axon edge guiding returns axons from the receiving side back to the compartment of origin. (c) Barbed channels also restrict passage of receiving-side axons into the other chamber. (Figure reproduced from Hasan and Berdichevsky[89].)

to their chamber of origin.[94] Barbed channels have also been developed, where again, projecting axons from one side are allowed to freely travel to the other, but the reverse side encounters blockades which restrict entry to the other chamber.[95]

One recent report (Renault et al.) demonstrates the ability to form a functional neural circuit model using a combination of optogenetic stimulation and calcium imaging readout (Figure 1.5).[1] The device was designed to have two opposing chamber, with microchannels tapered at the one end to provide directionality in the circuit. To stimulate and measure activity, Renault et al. use Channel-rhodopsin 2, a light sensitive ion channel in combination with a red-shifted calcium indicator,

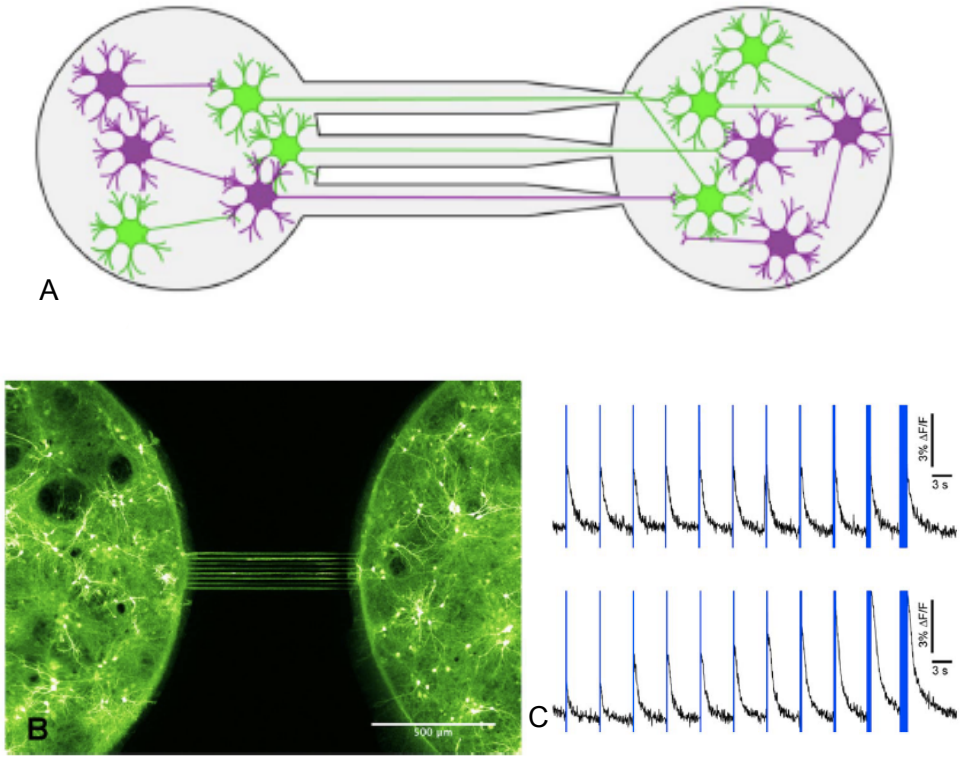

Figure 1.5. Microfluidic device combining optogenetics and calcium imaging. Renault et al.[1] previous designed a device for the compartmentalization of different neuronal populations. They demonstrate the utility of the approach for the combination of optogenetics (via ChR2) and calcium imaging. A) Device schematic demonstrating distinct compartments. Microchannels have tapered ends on right-hand side to mitigate axonal migration to the left chamber. B) ChR2-YFP labeled primary embryonic rat neurons (E19). C) Calcium signals are time-coupled to light pulses, indicating ChR2-mediated signaling. (Figure reproduced from Renault et al. 2015[1], with modifications).

Calcium Orange. In this report, the authors demonstrated communication between compartments via calcium imaging and stimulation of neurons via Channelrhodopsin 2. They also showed that circuit directionality produced a differing signal (either non-existent or delay) between chambers. This important work for neural circuit modeling serves as a proof-of-concept for human induced neuronal studies. The same techniques can be used to generate human neural circuit models.

While these compartmentalized systems described above do have some advantages, namely, ease of production and experimentation, there are some draw-

backs. Many of them are not open to patch clamp apparatus and so functional studies are limited to imaging procedures. Furthermore, circuit connections are stochastically determined, and so it is difficult to understand the readout of any individual population of neurons, especially when the subtypes are mixed (e.g., excitatory and inhibitory). For compartmentalized systems, one cannot know how many projections move from one chamber to another, and there may be large variation within the systems. Additionally, many of these studies have only demonstrated utility for primary hippocampal cultures, which serve the purpose of demonstrating network activity, but cannot directly serve as a model for human psychiatric disease. Human stem cells have been recently introduced into these systems with the goal of providing a more "humanized" model, with the advantage of being able to generate different neuronal subtypes from known genetic backgrounds. In order to demonstrate their utility of circuit modeling and drug screening, these models must provide the following: 1. Human-derived neurons for more precise genetic background. Due to the failure of therapeutic translation from rodent models, therapeutic targets may be more appropriately identified if human cells are used. 2. Ease of morphological and functional analysis. Functional analyses ideally would include either electrophysiology or calcium imaging, as per research need. 3. Defined circuit metrics. If the functional or morphological readout of the system is unclear or obfuscated because of circuit noise, this makes the model system data difficult to interpret. Overall, these systems must be carefully setup to provide the right answers to the right questions.

In light of the need for new and improved model systems, we have developed two approaches that take advantage of these techniques and approaches. *We hypothesize that human induced neuronal technology can be combined with microfluidics to generate specific circuit models for therapeutic development.* The tools described above can be used to stimulate and readout activity, and assay platforms can be development for therapeutic screening. Furthermore, induced neuron technology enables the researcher to produce a variety of different neuronal subtypes, and therefore more accurate inter-nuclei circuit models can be established to further our understanding on how neural circuits behave in diseased and normal conditions.

CHAPTER 2: GENERATION OF A MULTI-CHAMBERED DEVICES FOR THE FORMATION OF FUNCTIONAL CIRCUIT MODELS

Introduction

It has been previously shown that compartmentalized devices can successfully segregate neuronal somata and neurites into distinct compartments. Most studies however have focused on the communication of two types of neurons to each other in a two-chamber configuration.[1, 88] While two-chambered models certainly have utility for investigating neuronal communication, brain circuits are often generated by the connections from many different nuclei. Regarding the mesolimbic dopamine pathway, the nucleus accumbens (NAc) can receive inputs from both prefrontal cortex (PFC) and ventral tegmental area (VTA).[96, 97] We therefore sought to develop a model in which one population of neurons, in this case, analogous to medium spiny neurons in the NAc, receives input from two communicating side chambers (excitatory neurons analogous to PFC and dopaminergic neurons analogous to VTA). The proposed device has a total of five chambers: four communicating side chambers, that is, side chambers with microchannels to the large central chamber, which is open to patch clamp. This setup allows us to investigate the role of different neuronal populations which are separate from each other but which interact with central chamber neurons, and therefore generate a 3-way circuit.

This approach can also be expanded to include an arrayed compartmentalized device. Here, due to space limitations within a microwell, two separate compartments are designed into microwells of a 96 well plate, separated again by a se-

ries of microchannels. These approaches build off previous lithographic approaches for compartmentalized models. The fabrication and assembly of both devices are described in detail below. In addition to fabrication, experimental procedures are discussed below.

Materials and Methods

Microfluidic devices were produced using soft lithography. Induced neurons were seeded into completed devices for experimentation. Subsequent analyses, e.g., patch clamp recordings, immunocytochemistry, and/or calcium imaging were then performed after 4-6 weeks in culture. Techniques used are described in detail below and outlined in Fantuzzo et al.[2]

Device Fabrication

Masks were designed using DraftSight software. Two masks were needed for each device: one for the microchannels and one for the chamber structures. For the 96 well plate, half of the plate (that is, 48 wells) was placed on one wafer. This was a limitation of the 4 inch wafer size. To generate a full plate, two complete slabs of PDMS must be used. Photolithography utilizes the reactivity of various photoresists with UV light. Once the master wafer is produced, it is used as a mold to generate polydimethylsiloxane (PDMS) prints—the process of soft lithography.[98, 99] Wafers for device fabrication were cleaned by exposing them to a series of solvents. A wafer was placed in a dish with acetone for 10 minutes, followed by a dish of isopropanol for 10 minutes, followed by a dish of distilled water for 10 minutes. The wafer was then dried and placed into a 150°C oven to ensure that it was dry prior to spin-coating photoresist. The lithographic process was per-

formed in two distinct layers: the first is a thin layer defining the microchannel structures (3 μm in height) and the second layer defines the chamber structures (approximately 320 μm in height) (Figure 2.1). To generate master wafers for these two layer devices, a thin layer of SU-8 2002 photoresist (Microchem) was spun onto a clean wafer at 1000 rpm. This generated a 3 μm resist layer according to spin protocols from the manufacturer.[100] The photoresist layer was pre-baked for 1 minute at 65°C followed by 2 minutes at 95°C. The wafer was then exposed using an EVG620 Mask aligner (EV Group, Tempe, AZ) to UV light under a photomask with a net energy of 180 mJ/cm^2. The wafer was then baked again (post-exposure bake) for 1 minute at 65°C followed by 5 minutes at 95°C. Once cool, the wafer was developed in SU-8 developer for approximately 60 seconds. The wafer was finally hard baked at 150°C for approximately 45 minutes.

The second layer for the chamber structures involved two stacked layers of SU-8. SU-8 2075 was spun onto the wafer at 1000 rpm, giving a layer of 240 μm. This layer was baked for 10 minutes at 65°C and 50 minutes at 95°C. Once cool, a layer of SU-8 2025 was spun onto the wafer at 1000 rpm, adding a thickness of 80 μm. This gave a total thickness of approximately 320 μm. This layer was baked for 10 minutes at 65°C and 50 minutes at 95°C. After the pre-bake, the wafer was exposed to UV under a photomask with a net energy intensity of 810 mJ/cm^2. The wafer was then baked for 5 minutes at 65°C and 15 minutes at 95°C to assist cross-linking. The wafer was next developed for approximately 45 minutes in SU-8 developer on a vortexer. Developer was refreshed every 20 minutes to mitigate

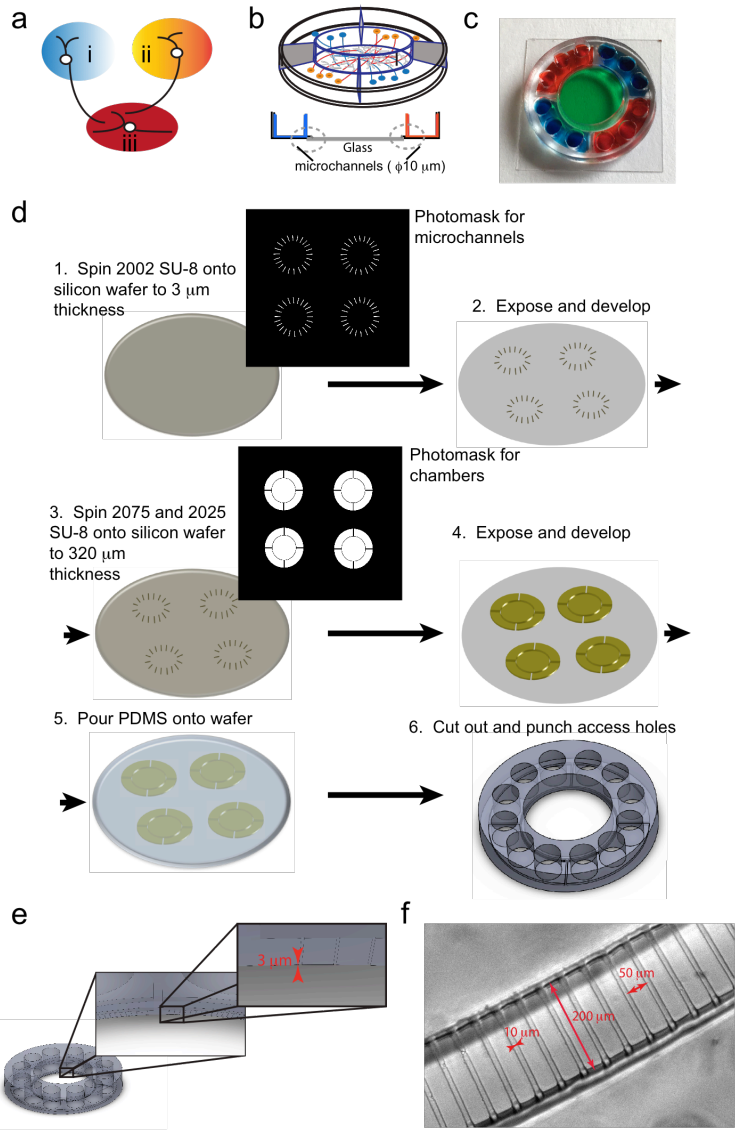

Figure 2.1. Diagram of µNeurocircuitry device designed for interconnecting three different subtype neurons. (a) Diagram of a brain nucleus receiving two inputs. (b) Device schematic. Four outer chambers surround one large central chamber. Axons project through 10 µm wide microchannels to communicate from the outer to central chamber. (c) Completed device bonded to glass cover slip. Colored dye indicates different chambers. (d) Fabrication protocol. Soft lithography was used to create a 3 µm layer followed by a 320 µm layer. PDMS is poured onto the master and cured. Holes are punched in the PDMS and the device is bonded to glass to yield the final device. (e) 3D representation of device with insets showing 3 µm channel height. (f) Bright field image of microchannels and corresponding dimensions. (Figure reproduced from Fantuzzo et al. 2017.[2])

solvent saturation. Finally, the wafer underwent a slow annealing hard bake. This hard bake was a slow ramp from room temperature (20°C) to 105°C. At 105°C, the temperature was held for 20 minutes, until it slowly ramped back down to room temperature.

Following the completion of photolithography, the wafer was coated in trichloro (1H,1H,2H,2H perfluoro-octyl) silane for 30 minutes. Sixty microliters of silane was added to the surface of a petri dish containing the wafer and placed in a vacuum chamber. The vacuum facilitates the evaporation and deposition of the silane onto the wafer surface. Once completed, a 1:10 mix of PDMS curing agent to PDMS monomer (Silgard) was added to the wafer. The PDMS mixture was degassed for approximately 2 hours. Entrained bubbles were removed using a pipettor. Once free from bubbles, the wafer with PDMS was placed in a 65°C oven overnight to cure.

Cured PDMS was removed from the wafer using a razor blade. Device chambers were punched as follows: for circular devices, the central chamber was punched with a hollow punch of diameter either 10 mm or 3/8 in. (Some devices had an central chamber diameter of 11 mm and others 10 mm. These devices were used interchangeably and seeded with the same density.) Side chambers were punched three times with a 3 mm diameter punch. The device itself was then removed from the PDMS with a 20 mm punch. The 96 well plate PDMS slab was produced in the same was as described above. To provide access holes, a 3 mm disposable punch was altered to have an oval shape by compressing the punch tip. Two punches per chamber were used to remove as much PDMS from the chamber

as possible. The PDMS slab was then removed with a razor blade. Once devices were removed, they were cleaned and bonded to their glass substrates.

Circular devices were cleaned by sonication. Devices were placed in a bottle containing acetone and were sonicated for 1 hour. Afterwards, the devices were removed and dried thoroughly in a fume hood followed by a 65°C oven overnight. Next, devices were placed in a bottle containing isopropanol and were sonicated for 40 minutes. Devices were then dried thoroughly before bonding. Devices were bonded to 0.17 mm thick coverslips (22 mm x 22 mm) using plasma oxidation with an ETP high frequency generator (Electro-technic Products, Inc., model BD-10A, Chicago , IL). The PDMS was then placed onto the glass coverslip and placed on a hotplate at 95°C under light weight for 30 minutes. Devices were then re-exposed to oxygen plasma to ensure their oxidation and placed into a 50 ml conical tube of distilled water to maintain hydrophilicity until sterilization.

Ninety-six well plates were prepared in a slightly different way. PDMS slabs were washed with isopropanol followed by water and allowed to fully dry. The PDMS was bonded to a 0.17 mm thick glass plate using oxygen plasma. Both the glass and the PDMS were placed in an oxygen plasma generator and were exposed to 60% oxygen for 1 minute at 100 W. The slab was then placed in contact with the glass plate and bonded on a hotplate at 95°C under light weight for 30 minutes. The PDMS/glass substrate was finally bonded to the bottom of a Greiner Bio-One μClear 96 well plate. To provide access to the PDMS slab, the well bottoms were removed using a 10 μl pipette tip. The tip head was pressed into the well bottom to punch out the plastic. Since PDMS was bonded to the plate bottom

which is polystyrene, the bond needed to be facilitated through a silane treatment by aminopropyltriethoxysilane (APTES). To perform the APTES treatment, the polystyrene was first exposed to a 100 W, 1 minute oxygen plasma treatment. It was then placed in a bath of 5% APTES in distilled water at 80°C for 20 minutes.[101] The polystyrene plate was then washed with distilled water and allowed to fully dry. Lastly, the plate and PDMS were exposed to oxygen plasma at 100 W for 20 seconds, and then bonded overnight in a 65°C oven under light weight. To re-oxidize the surface, the completed plate was placed in oxygen plasma at 100 W for 1 minute. Immediately following the treatment, distilled water was added to the wells to maintain their hydrophilicity. The plate was then wrapped in parafilm until sterilization.

Lentiviral production

Lentivirus is required to generate induced neurons. Lentivirus carry the genes necessary to generate neuron-specific transcription factors, which, when expressed, produced neurons from induced pluripotent stem cells (iPSCs) when doxycycline was present.[45, 47, 102, 103]

All lentivirus were produced through transfection of human embryonic kidney (HEK293) cells. HEK293 cells were plated at approximately 50% confluence when transfected. A calcium phosphate transfection was used to introduce the viral components into the HEK293 cells.[104] Prior to preparation, the HEK293 media (DMEM with 1% penicillin/streptomycin and 10% fetal bovine serum) was refreshed. Lentiviral envelope and capsid plasmids (VsVg, RRE, and Rev) were added at the appropriate ratios into a small plastic tube. To the tube were added water

and calcium (2.5 M) for a final volume of 0.5 ml. This solution was drop-wise added to a 0.5 ml solution of 2X HEPES-buffered phosphate solution. The solution was incubated at room temperature in the dark for 30 minutes, and then added to the HEK293 culture media. Addition of calcium phosphate crystals was kept to a timeframe within 1 hour of refreshing the HEK293 media.

Day 1 after transfection, the medium was discarded and refreshed. Medium was collected on days 2 and 3. When concentrated, the collected medium was spun in an ultracentrifuge at 25,000 rpm (106,490 rcf) and resuspended in 100 μl DMEM. If unconcentrated, the virus was aliquoted into microtubes at a volume of 610 μl each. The lentivirus generated from this procedure were reverse transcription transactivator (rtTa), as well as transcription factors Ngn2 (with puromycin resistance), Dlx2 (with hygromycin resistence), Ascl1 (with puromycin resistance), EN1, Fox2a, Lmx1a, Nurr1, and Pitx3.

iPSC sources and maintenance

Induced pluripotent stem cells were prepared from human primary lymphocytes using Sendai viral vectors (CytoTune™, Life Technologies, Grand Island, NY).[47, 105] Source biomaterials were from a de-identified repository and were therefore exempt from human subject regulations. Stem cells were maintained using feeder-free mTeSR1 medium (Life Technologies).

iPSC infection to generate induced neurons (iNs)

iPSCs were passaged into a 6-well plate at a density of 500,000 cells/well. The date of passage was Day -1. Cells were passaged into mTeSR™1 media

(STEMCELL technologies) with 5 μM Y-compound (Y-27632, a ROCK1 and ROCK2 inhibitory which promotes the survival of stem cells).[106] On Day 0, iPSCs media was changed to mTESR containing 5 μM Y-compound and lentivirus. Depending on the desired neuronal subtype, different lentivirus were added. Volumes of virus added for infection, along with the subtype generated, are shown below in Table 2.1.

To utilize the Tet-On induction system, all virus was also infected with rtTa lentivirus at a ratio of 1.32-1.5X the volume of the one of the other viruses (1.32 for excitatory, 1.5 for all others). For example, for Ngn2 at 2.5 μl/ml, rtTa is 3.3 μl/ml and for Dlx2 at 3 μl/ml, rtTa is 4.5 μl/ml. For electrophysiology experiments, channel-rhodopsin 2 lentivirus (with co-expressed tdTomato reporter) was also added to excitatory neurons (9 μl/ml). The virus was added on Day 3.

Table 2.1. Lentiviral vector volumes required for iPSC infections to generate induced neurons.

Transcription Factor	iN subtype	Day Added	Volume (μl/ml)	Unconc. Volume (μl/ml)
rtTa	All	0	1.32/1.5X	1.32/1.5X
Ngn2	Excitatory	0	2.5	100
Dlx2	Inhibitory	0	3	100
Ascl1	Inhibitory/DA	0	3/4	100
Nurr1	DA	0	4	
Lmx1a	DA	0	4	
Foxa2	DA	3	4	
Pitx3	DA	3	4	
EN1	DA	3	4	

Doxycycline, which is used to induce expression of Tet-On vectors, was added to mTESR with Y-compound on Day 1 at a concentration of 2 μg/ml. On

Day 2, puromycin (1 μg/ml) was added to select for iPSCs which were infected with lentivirus. Y-compound was removed and doxycycline was maintained to continue differentiation. Only cells expressing both rtTA and the corresponding vector with resistance (Ngn2 or Ascl1) will pass through selection. Additional lentivirus were added on Day 3 as applicable. For the production of dopaminergic neurons, vectors carrying DNA for EN1, Foxa2, and Pitx3 were added to induced neurons. As needed, ChR2-tdTomato was added to excitatory neurons to enable optogenetic stimulation. Vectors carrying DNA for GCaMP6 were added as needed for calcium imaging studies on either Day 0 or Day 3. Inhibitory neurons were also selected with hygromycin, since a hygromycin (25 ng/ml) resistance was built into the Dlx2 vector. Concentrations of puromycin and hygromycin were occasionally increased as needed, to more aggressively select for iNs. Induced neurons were maintained in Neurobasal media with puromycin and doxycycline until plating.

Device preparation, cell seeding and maintenance

Completed devices were removed from water (if necessary). Excess water was aspirated from all wells. Matrigel™ (Corning) was added to cover the cell surface. The devices were placed into the incubator for at least one hour to provide coating of the surface. Glia isolated from P_0 pups were seeded into the wells one day prior (Day 4-5) to iN seeding (Day 5-6). Glial cell concentration was approximately 300 cells/mm^2 (210 cells/mm^2 for the circular device central chamber). For the microplate, a 15 μl bolus of cells was added to the bottom of each well. Ap-

proximately 1 hour was given for the cells to adhere to the surface. After 1 hour, approximately 200 μl of media was added to the well. This additional step was necessary to keep cells restricted in their respective compartments during seeding. Due to the microplate design, the height of the wall separation was restricted to the skirt height of the microplate (approximately 2.5 mm)[ii]. Glia were cultured and seeded in Dulbecco's Modified Eagle Medium (DMEM) with 10% Fetal Bovine Serum (FBS) and 1% Penicillin / Streptomycin (P/S). Glial cells were removed from the flask with Trypsin/EDTA and re-seeded into the microdevice.

Induced neurons were seeded the following day at approximate concentrations of 1900 neurons/mm^2 and 1600 neurons/mm^2 for the central chamber. iNs were plated and cultured in Neurobasal with 5% FBS, 1% P/S, 10 ng/ml BDNF, 10 ng/ml GDNF, 10 ng/ml NT3, and 2 μg/ml doxycycline. Cells were removed from 6-well plates with Accutase and re-seeded into the microdevice. Circular devices were fed every 2-3 days and microplates were fed every 4 days. Due to the lidless, open design of the circular device, evaporation would occur within a few days. To reduce evaporation, circular devices were placed into 35 mm petri dishes. Two dishes were then placed into one 10 cm petri dish. To the 10 cm petri dish, approximately 1 ml of sterile water or PBS was added. This added an additional level of humidity to the environment. Circular devices were kept in culture for 4-6 weeks

[ii] This restriction is due to the operation of the GE IN Cell Analyzer 6000, for which the plate was designed. The IN Cell recognizes consistent, commercially available plates, and so the plate outer dimensions could not be altered. Having a PDMS slab thicker than the skirt height would increase the total height of the microplate, offsetting pre-defined settings in the IN Cell software.

before experimentation and 96 well plates were kept for 5-7 weeks before experimentation.

For the 96 well plates, 3,200 glia per compartment were seeded (6400/well) and 25,000 neurons were seeded per compartment. All 96 well plates were purchased with lids, and no additional measures to reduce evaporation were needed. Day 4 after seeding, 96 well plate cultures began a slow transfer onto BrainPhys™ media (Stem Cell Technologies). Induced neurons were plated as described above for glia, only using 10 μl/chamber followed by a 5 hour waiting period. At Day 4 after seeding, 50 μl was removed from each well, and 50 μl of BrainPhys™ with L-glutamine and NeuroCult™ SM1 supplements with 1% P/S, 10 ng/ml BDNF, 10 ng/ml GDNF, 10 ng/ml NT3, and 2 μg/ml doxycycline were added. At Day 8, 80 μl of media was removed from each well, followed by 100 μl of BrainPhys™ with supplements. At Day 12, 100 μl was removed from each well, and fed to approximately 250 μl in each well. Depending on well location, some wells required more media than others during each feeding due to greater evaporation. Devices were cultured for 5-7 weeks before analysis.

Immunocytochemistry

For the staining of circular devices, cells were fixed in 4% paraformaldehyde for 15 minutes. Cells were then permeabilized with 0.2% Triton X-100 for 10 minutes, followed by blocking buffer (20% normal goat serum in PBS) for 1.5 hours. (96 well plate stains used blocking buffer of 1% normal goat serum, 4% bovine serum albumin in PBS.) For the circular device, the primary antibodies used

were anti-MAP2 (Sigma, M3696, 1:750, M1406 1:1000 and 1:500), anti-tyrosine hydroxylase (Millipore AB152, 1:500), anti-vGlut2 (NeuroMab clone N29/29, 1:1000), anti-GAD6 (Sigma, G5038, 1:1000), anti-β-III-tubulin, Covance, 1:500), anti-synapsin (E028, from the Südhof lab, 1:3000), and Hoechst (1x). AlexaFluor conjugated, species matched antibodies were used as secondary antibodies.

For the 96 well plate, the same procedure was followed, but with a different blocking solution. Primary antibodies used were anti-synapsin (E028, from the Südhof lab, 1:3000), anti-HA (rat High Affinity, Sigma, 1:500, 1:2000, 1:3000), anti-MAP2 (Sigma M1406, 1:1000, Millipore 3418, 1:200), anti-vGAT (Millipore, AB5062P, 1:500). AlexaFluor conjugated, species matched antibodies were used as secondary antibodies.

Electrophysiology

The following section contained within brackets is reproduced from Fantuzzo et al. 2017.[2]

[Standard electrophysiology was performed as described by Vierbuchen et al.[103] and Pang et al.[45] Whole-cell patch clamp recordings were made in the neurons located in the central chamber. Both current and voltage clamp experiments were performed. For current clamp experiment, spontaneous action potentials were recorded at resting membrane potential; for evoked stem current clamp recordings (steps of 5 pA from -20 pA to 35 pA), negative currents were injected to keep the membrane potential at around -60 mV. For voltage clamp experiments, spontaneous post-synaptic currents (PSCs) were recorded at a holding potential of -70 mV;

whole cell current responses were collected by a step depolarization protocol (step voltage injections were given from -100 mV to 0 mV with a step size of 10 mV).

Optogenetic experiments were performed by stimulating ChR2 infected excitatory neurons with 470 nm LED light (Thorlabs). Light evoked synaptic responses were recorded from central chamber neurons at a holding potential of -70 mV. All electrophysiological experiments were performed using a rig containing a Molecular Devices 700B amplifier (Molecular Devices), a Digidata 1400 A/D converter, a Sutter 385 manipulator, and an Olympus IX50 with an infrared video camera. Data were filtered at 2 kHz and digitized at 5 kHz. Data were collected using pClamp10 software (Molecular Devices).]

Calcium Imaging

Calcium imaging experiments were performed using a IN Cell Analyzer 6000 (GE Healthcare Life Sciences). Media was removed from the 96 well plate wells and HEPES buffer was added. To approximate a final volume of 190 μl, 170 μl of HEPES was added to the culture, since there was approximately 10 μl left in each chamber after media removal. For liquid handling operations, 10 μl was removed from the matching well of the reagent plate and added to 190 μl of the analysis plate. Fifty μl added to 150 μl was also used, but this produced a disturbance artifact which may have impacted the network firing. For the addition of KCl, 80 μl of "High KCl" HEPES buffer[iii], that is, HEPES buffer with NaCl exchanged for

[iii] High KCl HEPES was used only for calcium imaging experiments. This buffer was prepared in the same way as normal HEPES, only the NaCl was exchanged for additional KCl, yielding a final concentration of 145 mM. This was to preserve osmolarity during the addition of the reagent.

KCl (to give a final concentration of 145 mM), was added to the 200 μl buffer within the analysis plate, to yield a final concentration of 41.4 mM. CNQX, a glutamate receptor antagonist, was added to the cultures during experiments at a final concentration of 20 μM. Images were collected at 9 Hz. Reagents were dispensed at frame 900 or 1200. After an additional 1500-1800 frames were collected, the analysis was completed and the reagent plates were switched.[iv] An additional 600 or 900 frames were collected after the plates were exchanged, with addition of KCl occurring at frame 300.

Production of hM3D Lentiviral construct is discussed in Chapter 4. With a goal of producing a dose response curve, different doses of CNO were applied to an excitatory – inhibitory circuit. hM3d-infected excitatory iNs were seeded on one side of each well. Inhibitory iNs were seeded on the opposite side of each well. CNO doses ran from 500 nM to 0.8 nM, as consistent with previous studies.[60, 62] Concentrations of CNO were added to different plate locations, to avoid any plate bias (shown below in table 2.2).

Table 2.2 CNO dose response experimental concentrations and setup.

Reagent Plate [CNO]	Final [CNO]	Wells
10000	500	A1, G2
2000	100	B1, F2
400	20	C1, E2
80	4	D1, D2
16	0.8	E1, C2
0	0	G1, B2 (A2)

[iv] The IN Cell Analyzer can only add one reagent per experimental run. Therefore, two runs needed to be performed to capture both the addition of the experimental reagent and KCl.

In addition to CNO, we also investigated the effects of 500 nM Clozapine on the circuit, in both DREADD-infected cultures and non-infected cultures.

IN Cell exposure was set to 0.07 ms for the FITC channel (488 nm), with image collection set to 0.01 seconds. Discrepancies in the software resulted in an average image collection time of 0.11 seconds, equivalent to 9 Hz. Exported TIFF images were grouped into three folders of 800 images, and images for KCl addition were added as a separate folder. Each folder containing 800 (or 900 images for KCl) were opened as individual stacks in ImageJ. These stacks were then concatenated and contrast adjusted to overwrite any individual image adjustments. As the images were 16-bit, contrast values of 85 and 535 were used to reset the contrast. The look up table (LUT) of the full image stack was then set to "Fire". AVI videos were saved using a 70 frame/sec rate. For region of interest analysis, ImageJ's ROI manager was used. Circles were traced around neurons responsive to KCl. Next, the Multi Measure function was used in ImageJ to collect signal intensity information. To process the data as a ratio of signal over baseline, I used a custom MATLAB script which collects the lowest intensity value from the first 200 frames as F_0. Signals were then obtained using the ratio calculation $(F-F_0)/F_0$. To compare signals prior to CNO/Clozapine addition, I used two 90 second windows on either side of the addition. The first window was from frame 80 to 898 (818 frames = 90 seconds). The second window, after the addition of CNO/Clozapine was from frame 1500 to 2318. Ten cells were then individually counted from both the non-DREADD (Inhibitory) side and the DREADD side (Excitatory) to yield the data on the effects of CNO and Clozapine.

In addition to CNO/Clozapine, glutamate receptor antagonist CNQX was added to excitatory/inhibitory circuit wells, at a final concentration of 20 μM. Similarly, number of network firing peaks were calculated on either side of the addition. Here, a blank of HEPES buffer was added as a control, and the orientation of excitatory and inhibitory neurons in the well were altered to control for position of cell type with the device.

Comparison of Neuroligin-3 overexpression with respect to synapse number

Neuroligin-3 (NL3) has been shown to increase synapse number mouse neurons.[107] Additionally, mutations in NL3, such as R451C have been implicated in autism.[108, 109] We sought to use the effect of NL3 on synapse number as a paradigm to demonstrate the utility of the 96 well plate microdevice to perform synaptogenesis/morphological assays. To perform this assay, we infected excitatory neurons with three different lentiviral vectors. SV-2-GFP was used for one population of excitatory neurons, which were seeded in the left-hand side of each well. On the right hand side, three different excitatory neuronal populations were seeded: wild-type excitatory neurons as a control, neurons with lentiviral infection for wild-type NL3, and neurons infected with NL3 with mutation R451C. These cultures were maintained for approximately 5 weeks, and then fixed and stained. MAP2 (M1406 Sigma, 1:1000) and synapsin (E028, a gift from the Südhof laboratory, 1:3000) were stained for as the primary metric to quantifying synapse number. To quantify neuroligin-3, the viral constructs contained HA-tags for staining. Neurons were stained using anti-HA antibodies (Sigma, rat IgG1, 1:1000-3000), and all neuronal staining was followed by the appropriate secondary antibodies. Images were taken

on the IN Cell Analyzer 6000 using a 40X objective. Two-four fields were acquired from each side of a well. Three-four wells were collected for each condition. Synapse quantification was performed using *Intellicount*, which is an automated program described further in Chapter 4.

These methods were used to produce the devices and experiments described in the following chapters. First, I describe the formation of a 5-chambered device, followed in Chapter 5 by the extension of this technology to a high-throughput system.

CHAPTER 3: FUNCTIONAL MULTI-CHAMBERED DEVICE FOR STUDY OF THREE-WAY CIRCUITS

The figures and captures in this chapter are reproduced from Fantuzzo et al. 2017.[2]

Circular 5-chambered device

The goal of the circular device is to provide two main features: an open central chamber for patch pipette access and the capacity for forming a three-way circuit. Four outer chambers surround the one large central chamber, allowing axonal projections from the outer chambers to enter the central chamber (and vice versa). This approach was designed primarily to model the mesolimbic dopamine pathway, specifically, the projections to the nucleus accumbens. Altering the orientation however can change the cell type in the center, and therefore, the circuit modeled. We began co-culture studies using mouse neurons (no data shown), but soon moved into using human induced neurons after demonstrating successful device cultures. Induced neurons survive in culture up to 4 weeks *in vitro* in both 200 μm and 500 μm devices and project axons through microchannels to neurons on the other side (Figure 3.1). We seeded outer chambers with excitatory neurons infected with GFP lentivirus and dopaminergic neurons stained for tyrosine hydroxylase. Interestingly, dense bundles of axons are seen traversing the microchannels toward the DA-ergic central chamber (Figure 3.1c-e), where they are seen interacting with central chamber neurons. This demonstrates that we are able to generate induced neurons that interact in a defined way with the structure of the device and with each other through microchannels. Importantly also, neurons seeded within one compartment

remain in their compartment, while neurites alone project through the microchannels.

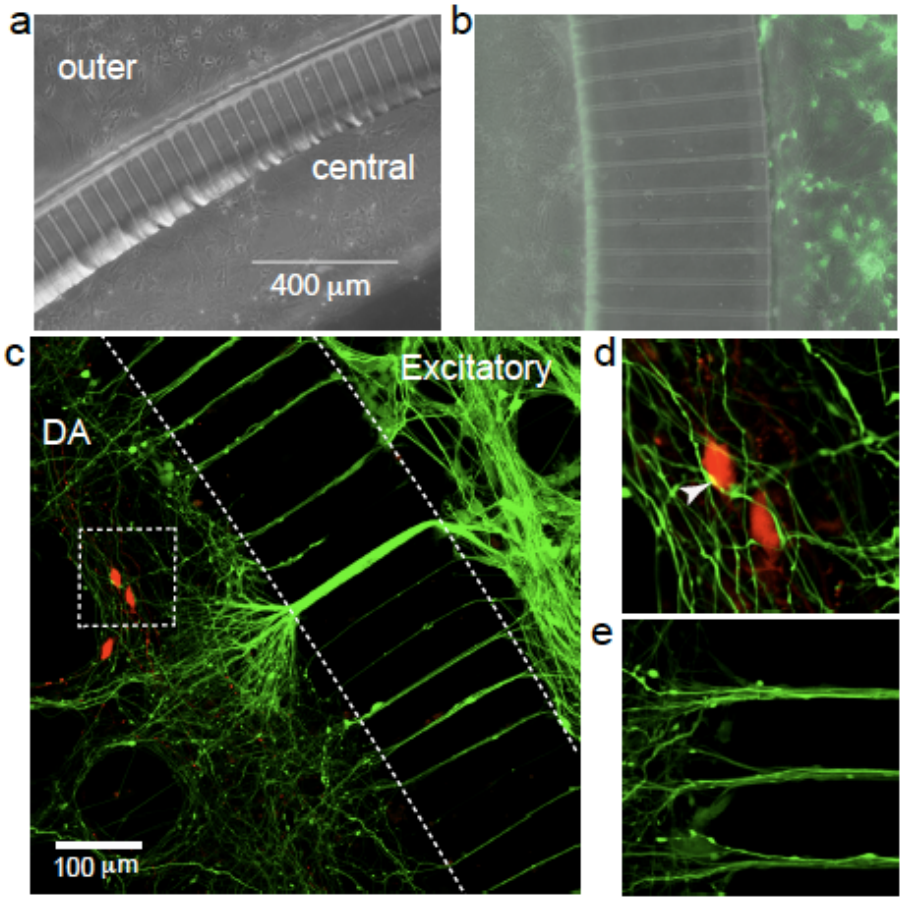

Figure 3.1. **Human neuronal culture within the microdevice.** (a) Induced neurons (iNs) cultured within a 200 µm walled device. (b) GFP-positive neurons cultured in a 500 µm walled device across from non-fluorescent iNs in the central chamber. (c–e) GFP-positive excitatory neurons exhibit extensive axonal projections to the central chamber and interact with TH-positive (red) DA-ergic neurons. Dashed area in (c) is showing in (d). Arrowhead showing a possible synaptic contact.

We next sought to establish a model of the nucleus accumbens and two of its arriving projections from the PFC and VTA. To construct this model, inhibitory neurons, analogous to NAc medium spiny neurons (MSNs), were produced and seeded in the central chamber. In an alternating fashion, excitatory neurons, similar to those found in the PFC and DA-ergic neurons similar to those found in the VTA

were seeded in the side chambers. After 4 weeks *in vitro*, the cells were fixed and stained for both pan-neuronal markers such as MAP2, Tuj1, and synapsin. Additionally, we stained compartments for subtype-distinctive markers (Figure 3.2).

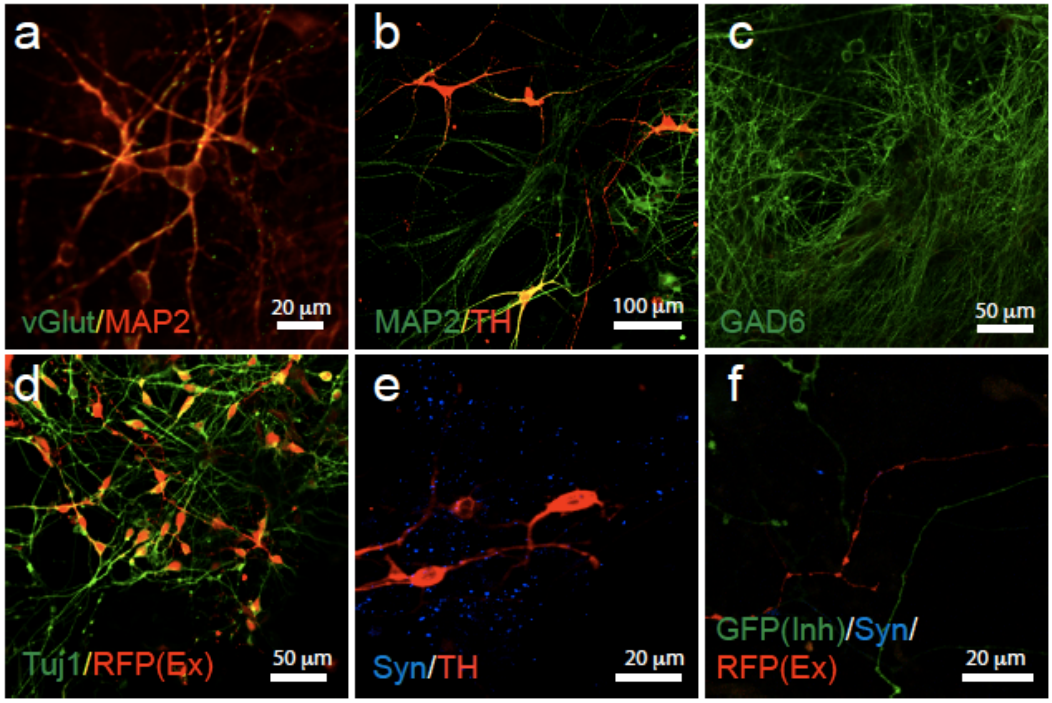

Figure 3.2. Morphological analysis. (a) Excitatory neurons express pan-neuronal marker MAP2 and vGlut2, an excitatory marker. (b) Dopaminergic (DA) neurons express MAP2 and synapsin, and tyrosine hydroxylase (TH), indicative of a DA phenotype. (c) GABAergic neurons express GAD6, indicative of an inhibitory phenotype. (d) Excitatory neurons infected with GFP express pan-neuronal marker β-III-tubulin (Tuj1). (e) DAergic neurons co-localizing with synapsin-positive boutons. (f) Interaction of inhibitory (green) and excitatory (red) neurons with synapsin-positive boutons.

Excitatory neurons were positive for vGlut, DA-ergic neurons were positive for tyrosine hydroxylase, an enzyme involved in the processing of neurotransmitter dopamine. Similarly, inhibitory neurons were positive for GAD6, an enzyme involved in processing the neurotransmitter GABA. While compartments were stained for their individual markers, diffusion between compartments through mi-

crochannels likely distributed all antibodies to every compartment during the staining process. This morphological analysis demonstrates that all three subtypes were generated, that they are indeed neurons, and that compartmental neuronal identities are largely preserved. Throughout the course of these experiments, there were a few neurons in any given device that did traverse the microchannels. These were few and likely had little to no impact on experimental design and analysis.

Establishment of a three-way circuit

Now that we have shown that induced neurons possess the morphology of neurons and interact with the microchannel structures of the device in a defined way, we sought to establish that the multiple compartmental design of the device can specifically facilitate the formation of a 3-way circuit. Previous studies have shown the formation of 2-way or binary circuits, where communication is established between two distinct subtypes.[1, 88] While three-compartment devices have been previously established, they were not designed to assay the functional connectivity between subtypes[84], at least by means of electrophysiology. Importantly for our purposes, a three-way circuit must be established between two side chamber neuronal subtypes and the central chamber, housing a third, distinct subtype. To demonstrate the utility of the device for such studies, we cultured three different populations of excitatory neurons in three chambers. GFP-labeled iNs were seeded in two side chambers and ChR2-tdTomato-labeled iNs were seeded in the other two side chambers, such that GFP and tdTomato iNs were in alternating compartments. Non-labeled iNs were seeded in the central chamber. Neurons were cultured for four weeks and then fixed and stained for MAP2 and synapsin. After four weeks,

excitatory neurons from the side chambers projected axons through the microchannels into the central chamber (Figure 3.3a). Interestingly and conveniently, axonal projects extend up to millimeter lengths into the central chamber and wrap around

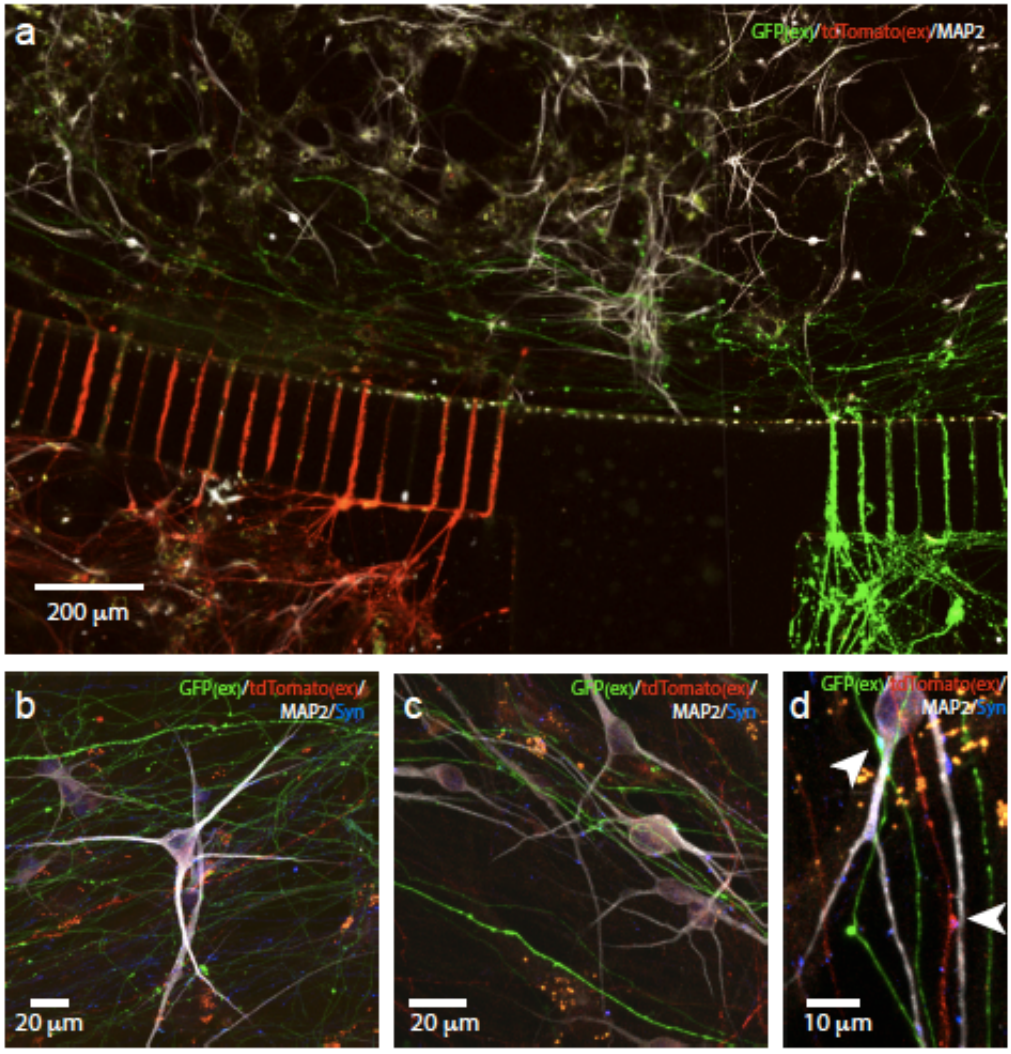

Figure 3.3 Three-way circuit connectivity among neurons cultured in different compartments. (a) Two side chambers project axons into the central chamber. GFP-labeled induced neurons (iNs) were seeded on the right side and tdTomato-labeled iNs were seeded on the left. (b–c) Central chamber neurons interact with processes from both GFP and tdTomato-labeled side chamber iNs. These iNs stain positive for synapsin (blue) and MAP2 (white). (d) A MAP2-positive neuron receiving projections from both tdTomato-positive and GFP-positive axons. White arrowheads indicate synapsin-positive boutons.

the side walls, matching the structure of the central chamber. Projections from both tdTomato iNs and GFP iNs can be seen in the central chamber, with extensive in-

teraction with MAP2-positive iNs (Figure 3.3b,c). It is important however than projections not just enter into the central chamber, but that they interact with neurons in such a way that suggests synaptic formation between all three neuronal subtypes. This occurred within the central chamber, such that cells were seen forming this defined 3-way circuit (Figure 3.3c, white arrows indicate synaptic boutons).

Additionally, to facilitate greater axonal extension and interaction between side chambers and central chamber, we seeded a greater number of side chamber neurons (45,000 iNs/side chamber), and did so three days prior to seeding central chamber neurons. This gives side chamber neurons the initial chance to attach and access microchannel space prior to competing with central chamber neurons. This seeding approach greatly increased the number of projections through the channels (Figure 3.4a) and enhanced the interaction with central chamber neurons (Figure 3.4b,c).

Having demonstrated that we can establish a model of morphologically-distinct induced neurons from patient-specific stem cells, we wanted to confirm the functionality of the iNs, and verify their connectivity as a circuit. As mentioned above, the central chamber is specifically designed to allow access for patch pipette, enabling electrophysiological analysis (Figure 3.5a). This is one of the unique features of this microfluidic device. We plated excitatory neurons in the outer chambers and inhibitory neurons in the central chamber. Upon recording spontaneous activity, inhibitory neurons demonstrated the ability to fire action potentials (Figure 3.5b). We wanted to evaluate the response of the iNs to steps in current and voltage. Current steps induce action potentials once the cell was

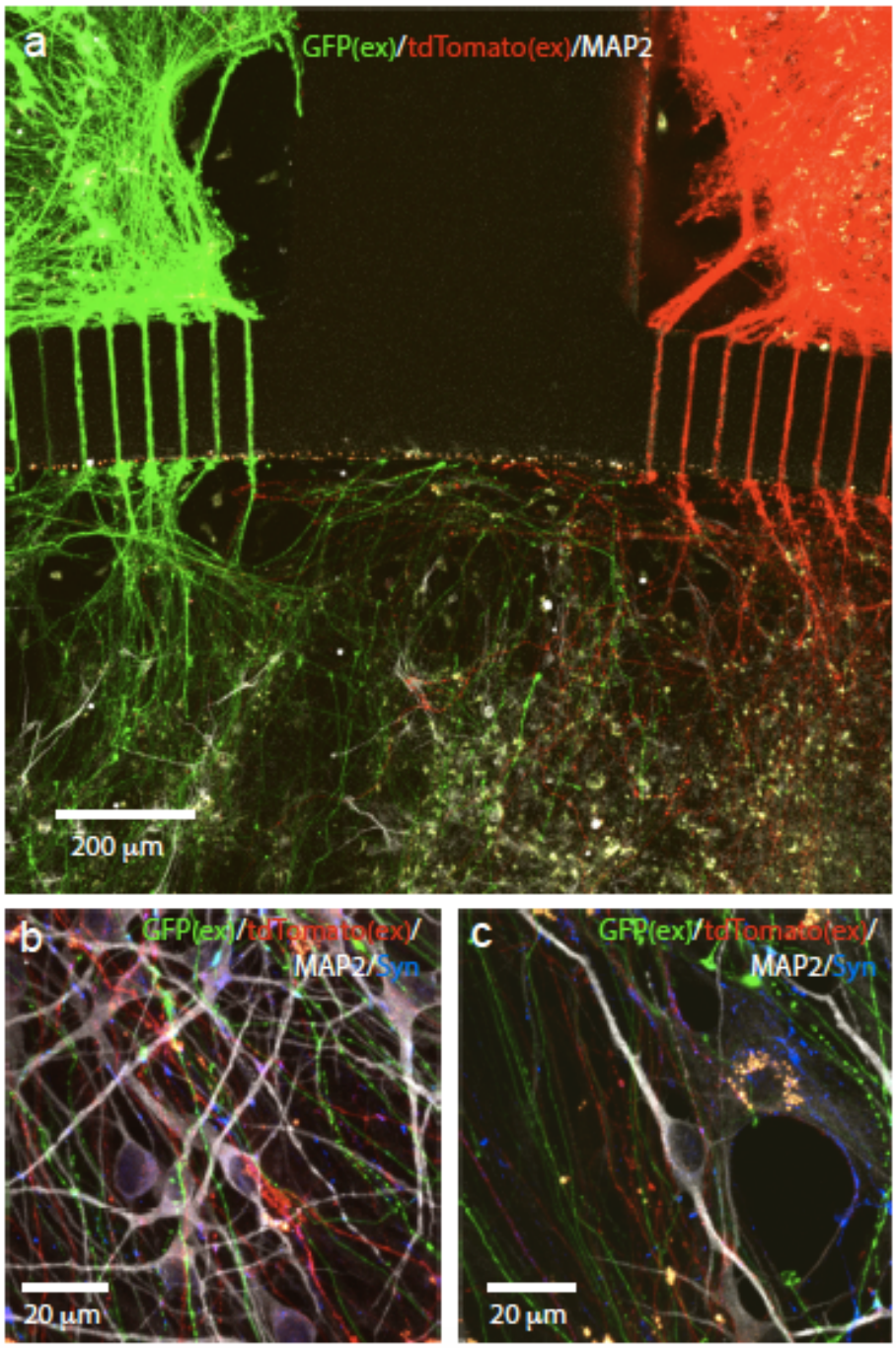

Figure 3.4. Three-way circuit with increased side chamber density. (a) Side chambers were seeded with 45,000 induced neurons (iNs) expressing either GFP or ChR2-tdTomato. Axons densely project from the side chambers into the central chamber. (b–c) tdTomato-positive and GFP-positive projections interact with iNs in the central chamber. iNs were stained with MAP2 (white) to show dendrites and synapsin (blue) to show synaptic boutons.

depolarized to its threshold. The iNs demonstrate a robust response to step currents (Figure 3.5c). Step voltage gives similar but additional information: action potentials are generated, but reveal aspects about the nature of the membrane channels. The initial drop reflects the opening of sodium channels and the corresponding rise in intracellular positive charge. The return to baseline indicates the presence rectifying potassium channels. These iNs displayed the presence of both channel types, further validating their neuronal phenotype (Figure 3.5).

Having demonstrated that the induced neurons are capable of spontaneous activity and possess the proper channels for action potential propagation, we next wanted to confirm that central chamber neurons were receiving inputs from side chamber excitatory neurons. We set up the experiment such that we could alter excitatory input from the side chambers onto the inhibitory neurons in the central chamber by CNQX, a glutamate receptor antagonist. We recorded spontaneous post synaptic currents (PSCs) from inhibitory neurons (Figure 3.5e). After the addition of 20 μM CNQX, no PSCs were observed (Figure 3.5f). This suggests that central chamber inhibitory neurons received glutamatergic input from side chamber neurons. Importantly also, these data show that a circuit has formed between excitatory and inhibitory neurons and that the circuit can be manipulated using specific receptor blockers.

While we demonstrated that we can block spontaneous network activity between chambers with glutamate receptor blockers, it was important also that we can probe the established circuit to induce activity. We took advantage of a common optogenetic approach which uses light-sensitive channels to depolarize cells.[21]

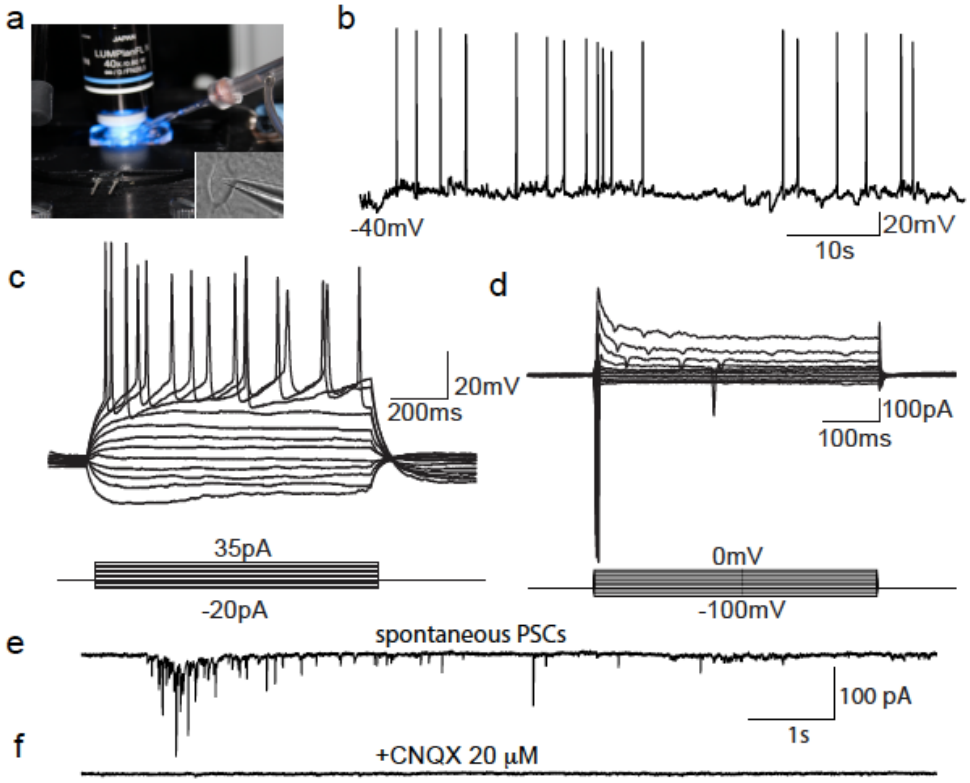

Figure 3.5. Basal functional characterization of human neurons in the microdevice. (a) Microdevice under electrophysiology patch clamp recording setup. (b) Spontaneous action potentials were recorded showing functional maturation of iNs. (c) Step current experiment performed on GABAergic neurons. They fi re repetitive action potentials upon depolarization. Step size is 5 pA. (d) Whole-cell currents were recorded in these cells showing a fast activation and inactivation sodium currents and outward potassium currents. Step size is 10 mV. (e) Spontaneous post-synaptic currents recorded from central chamber (GABAergic neurons). (f) Spontaneous post-synaptic currents (PSCs) recorded from central chamber could be blocked by 20 µM CNQX indicating glutamatergic transmission.

Excitatory neurons were infected with channel rhodopsin 2 (ChR2)-tdTomato and cultured in the four outer chambers. Inhibitory neurons were cultured in the central chamber. Excitatory projections could be seen entering the central chamber at four weeks in culture (Figure 3.6a,b).

Indeed, a vast network of projections were seen entering into the central chamber, suggesting a strong excitatory influence on central chamber neurons. To test the circuit connections, devices were placed on an electrophysiology rig and

central chamber neurons were patched. To stimulate excitatory neurons, we exposed channel-rhodopsin 2 to blue light (470 nm). A single pulse induced a single post synaptic current (PSC) in central chamber inhibitory neurons (Figure 3.6c), indicating the establishment of a connection between the two subtypes, and importantly, that the connection can be stimulated to produce a synapse-mediated response. When a train of light is provided to the excitatory neurons, a train stimulation is seen (Figure 3.6d). Lastly, we wanted to demonstrate that the circuit connections established in the central chamber were indeed glutamatergic and that we can silence the communication with CNQX. Once again, we recorded PSCs in central chamber neurons under train stimulations. Interestingly, asynchronous activity was seen after the train stimulation, indicating that the circuit as a whole is responding to the stimulation, not only the one patched cell (Figure 3.6e). When 20 μM CNQX is added to the central chamber, all optogenetic-mediated signaling from the side chambers was silenced (Figure 3.6f). Taken together, this demonstrates that we can create a defined circuit, in this case, excitatory → inhibitory, that we turn the circuit "on" through optogenetic stimulation, and that we can turn it "off" through chemical intervention (e.g., CNQX).

Lastly, we sought to investigate the diffusion of small molecules from side chamber to center. Chemical distinction between chambers is an important aspect for some studies of neural circuits, as researchers may want to treat one population of neurons separately from another. For example, drug addiction studies may want to expose one population of neurons with a drug and measure the readout on the circuit in its corresponding chamber. One difficulty with the current approach is

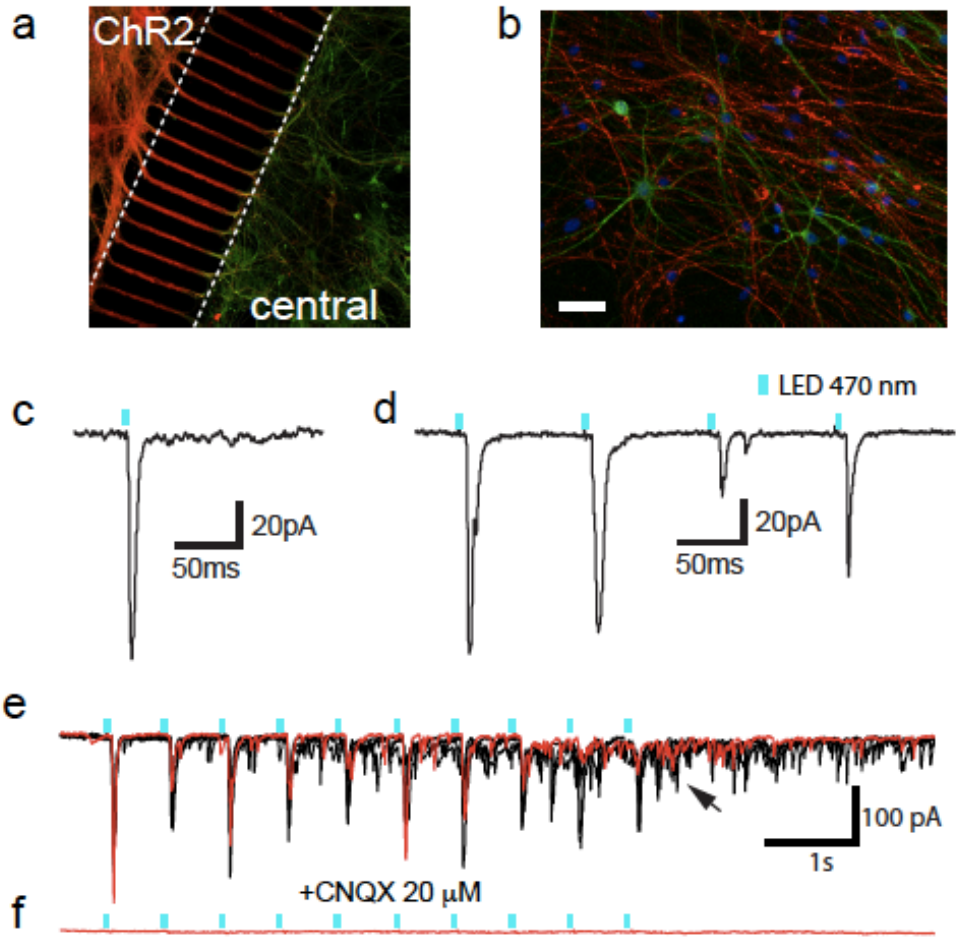

Figure 3.6. Optogenetics-aided synaptic functional analysis for outer-to-center neurocircuitry. (a) Device wall with microchannels. ChR2-tdTomato (red)-infected excitatory neurons project to β-III-tubulin-labeled inhibitory neurons (green). (b) Extensive excitatory projections inside the central chamber co-localize with MAP2-labeled neurons (green). Nuclei labeled with Hoechst (blue). Scale bar 50 µm. (c) Response to single pulse of blue light (470 nm). (d) Response to pulse train stimulation. (e) Post-synaptic currents (PSCs) recorded from central chamber neurons after excitation of terminals from projecting side chamber excitatory neurons with blue light. Arrow indicates asynchronous synaptic activity. (f) Addition of 20 µM CNQX eliminates AMPAR-mediated response to light pulse. Red traces show a single trace for visualization.

the presence of microchannels. These channels allow for diffusion between compartments, leading to the exposure of all neurons to the compound of interest. To test our device, we used fluorescein at 1mM final concentration, and measured the diffusion rate from the side chamber to the central chamber. Fluorescein was gently dispensed into the side chamber well, and images were taken approximately

every 15 seconds. Within a minute, fluorescein was seen entering the microchannels and crossing the other side to the central chamber (Figure 3.7c). When fit to a least-square model, the predicted time for compartment entry is approximately 45 seconds. While this time is short, it would allow for a brief window for small molecule study. Also, doubling the length of the microchannels would cause a quadrupling of the time for mass transfer, according to the equation for diffusivity $l = \sqrt{4Dt}$. Also, if the liquid heights are altered such that the head pressure creates a convective flow to oppose diffusion, this will also extend the time for analysis[83], although a patch pipette in the central chamber may disturb this concentration difference.

Discussion

Establishing *in vitro* models of defined neural circuits is an approach that can aid in the detection of disease-relevant phenotypes and mechanisms. Previous reports on compartmentalized systems have largely utilized rodent primary cells to establish functioning circuits, but this still does not account for species differences that may hide important neuronal activity or properties. Human induced neurons and the developing technology that allows the formation of distinct subtypes has opened new opportunity for disease modeling and genetic studies. We therefore used this technology to generate distinct subtypes of neurons, to generate a defined neural circuit, in this case, a model of the reward pathway targeted in substance abuse.

Our device has four outer chambers and one large central chamber. This allows for an experimental setup where three populations of neurons can interact and

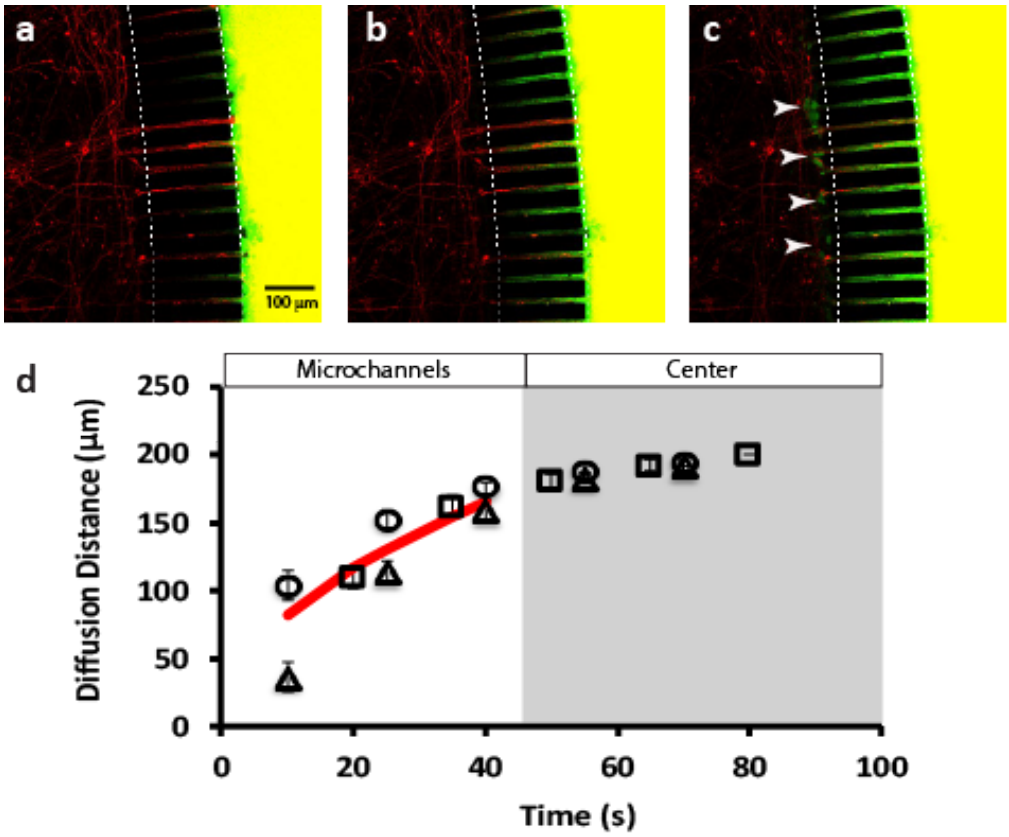

Figure 3.7. Fluorescein diffusion between the outer and central chambers. Fluorescein (1 mM final concentration) was added to side chamber and diffusion was measured through the microchannels. (a) Diffusion through channels at 20 seconds. (b) Diffusion through channels at 1 minute, 20 seconds. (c) Diffusion through channels at 6 minutes, 35 seconds. Red processes are ChR2-tdTomato-labeled excitatory neurons. Arrowheads indicate fluorescein breakthrough to central chamber. (d) Distance of di fusion down microchannels as measured from channel entry to diffusion front over time. Average time to reach central chamber was 45 seconds. Red line generated using a least-squares fi t on data points before breakthrough. Circles, squares and triangles indicate data points from three separate experiments.

form a functional circuit. We decided to seed excitatory neurons in the outer chambers for most studies, as these neurons mature quickly and fill microchannels with axonal projections, providing a partial directionality to the neural circuit model. This does not preclude however projections from other neurons from the central chamber to the outer chambers. To harness a stricter directionality in the circuit, one of the techniques described in Chapter 1 (Figure 1.4) can be applied. In many cases however, reciprocal connections may be desired, and the existing microchan-

nel structures will be sufficient to model such cases. One of the unique features of our device is its large, open central chamber, allowing patch pipette access. While there are other means of detecting circuit activity, electrophysiology remains the gold standard, and we therefore designed the system in such a way as to include all options. Importantly also, regarding addiction studies, minor changes in synapse formation and plasticity may not be visible with calcium imaging, but rather electrophysiology, and therefore such studies as collection of AMPA/NMDA receptor ratio data is only possible where electrophysiology can be performed.

While the setup of four outer chambers to the one inner chamber enables up to five populations of cells to be seeded, the device best handles situations of three connected populations. This is because of the size of the central chamber. Excitatory neurons can project axons millimeters in length into the central chamber, it is unlikely that neurons from outer chambers opposite each other will traverse the distance of the central chamber interact with the same population of central chamber neurons. We therefore limited the extent of the circuit to a three-way circuit. To demonstrate the formation of this three-way circuit, we cultured three populations of excitatory neurons in different chambers. Two of the excitatory neurons were labeled with fluorescent markers and the other was unlabeled. By demonstrating the utility of the device to form this three-way circuit (Figures 3.3 and 3.4), we show the ability to model complex circuits as found in the reward pathway.

In addition to proper neuronal morphology and device compartmentalization, this model must also be meaningful as a functional circuit. We demonstrated that we can create an excitatory neuronal circuit and that we can control the func-

tional connection between the two populations. Addition of CNQX blocks excitatory input from outer chambers, showing that not only have we produced the desired circuit, but also can disrupt neuronal firing between chambers in a defined way. Furthermore, we used optogenetics as a means of probing the circuit. We demonstrated that we could record inter-chamber activity. Between altering activity with CNQX and stimulating it with optogenetic approaches, we can create a tunable, controllable circuit that can house defined populations of neurons as defined by the experimenter.

This approach still has some limitations. It is difficult to control the number of axonal projections the central chamber neurons receive, and therefore recording any given cell will likely result in a large variation. This device, while including mouse glia, does not have all glia present in the brain, such as oligodendrocytes and microglia, which also may play a role in circuit formation and maturation. As discussed above, single chamber chemical treatments are currently limited due to the rapid diffusion through microchannels. This could be improved by increasing the length of the channels to extend the diffusion time. Lastly, with only four outer chambers, this leaves four regions whereby a three-way can be formed, namely the areas located near the outer chamber dividing walls. The number of these areas can be increased by expanding the number of outer chambers to eight.

The inclusion of human-derived induced neurons into compartmentalized devices holds promise for circuit modeling. Additional work must be performed to demonstrate the presence of unique endophenotypes drawn out by these circuit models which are directly connected to disease pathology. Here however, we have

shown as proof of principal the production of a three-way circuit model whose function can be probed to investigate neuronal circuit firing. As regards screening studies, this device does not currently lend itself as a high-throughput platform, however this approach can be expanded toward that format. We have built off this approach to generate a high-throughput platform, which is discussed in Chapter 5. To enable such studies, different tools and analysis programs must be generated to process such large amounts of circuit data. Some of these tools will be described in the next chapter.

CHAPTER 4: INTELLICOUNT AND OTHER TOOLS FOR HIGH-THROUGHPUT CIRCUIT STUDIES

High-throughput circuit studies results in the production of a vast amount of data, both morphologically in the form of images and functionally with calcium imaging stacks or MEA data. Furthermore sample replicates in the experiment further amplifies the data output. Automated programs and systems must be generated to handle this output. We have developed one system to accommodate synaptic puncta images – Intellicount – which is a MATLAB-based analysis program. This program will be discussed in detail below, followed by a discussion on the use of GCaMP6f for calcium imaging and the cloning of a DREADD (hM3D) for Lentiviral infections of induced neurons.

Intellicount – High-throughput synaptic puncta analysis using machine learning

The following statements and figures contained within brackets were taken from Fantuzzo and Mirabella et al. 2017, eNeuro[110], with the exception of footnote (v).

[*Introduction:*

The mammalian brain is composed of billions of neurons connected to each other by trillions of synapses, which govern information flow in the brain and thus control cognition and brain-related behaviors. Aberrant synapse formation has been implicated in a wide range of neurodevelopmental and neuropsychiatric disorders, including autism spectrum disorders, schizophrenia, and many others[111-113]. Morphologically, the synaptic connections composed of both presynaptic and postsynaptic components under light microscopy appear as puncta-like structures, often

called “synaptic boutons”. Considerable effort has been invested in developing techniques and platforms to accurately identify and quantify synapse numbers and other characteristics of synaptic proteins in order to unravel the molecular mechanisms by which synapses form and function under normal and abnormal conditions. Although some of these techniques can be very specialized, analysis of synaptic puncta by imaging of synaptic proteins by immunofluorescent (IF) labeling is among the most established and commonly used technique because it is informative, and relatively easy to perform. This type of analysis offers insight into the number, distribution within subcellular compartments (pre- or post-synaptic, dendritic spines, shafts and somatic), and other characteristics of synaptic protein complexes. The synapse density (number of synapses per unit length or area of dendrite), intensities of the synaptic protein IF signals, and the sizes of synaptic puncta often correlate with functional synaptic parameters as measured by electrophysiology [114-117]. Indeed, the size and intensity of the excitatory postsynaptic density protein 95 (PSD-95) puncta tend to correlate with measures of synaptic strength [118]. A handful of useful tools have been developed to facilitate image-based analysis of protein puncta associated with neural structures [119, 120].

However, several major limitations of existing tools available for analyzing synaptic protein puncta include the accuracy and reliability as well as the ease of use for performing such analyses, particularly when large data sets are involved. Commonly used methodologies often involve manual or semi-automated object tracing and region of interest (ROI) measurements to identify relative differences between experimental conditions. Experimenter-assisted manual quantification

methods [121] are often cumbersome and require tedious repeated work. While this approach can be accurate, it can be subject to human error and bias and depends on the skill of the experimenters. Therefore, several commercial (e.g., Metamorph, Molecular Devices) and open-source semi-automated software programs (e.g., ImageJ, with different customized modules) have been developed. These platforms generally employ thresholding and segmentation paradigms to identify puncta and neural processes [119]. Recent work has extended semi-automated processing techniques to include multiple thresholds [120], which significantly improves separation of adjacent IF puncta clusters. However, for puncta whose full area is occupied by a broad grayscale range, simple thresholding may alter the size, shape and intensity because the thresholds required to separate adjacent puncta can eliminate the low intensity pixels which may actually demarcate the true synapse boundary. Specifically, use of higher thresholds, if left non-optimized by the user, can artificially underestimate puncta size since the threshold required to separate closely adjacent puncta tend only to capture the highest intensity pixels of an ROI and *vice versa*. Additionally, most existing platforms are considered semi-automated, because they require interaction by a user with the program at multiple processing and preprocessing steps (often with each image) and do not allow automated batch processing of multiple nested folders (i.e., folders organized by condition within a single directory) or directories with images collected from different conditions. Moreover, most programs are normally not integrated with statistical capabilities. Therefore, analysis of synaptic protein puncta is often tedious and prone to experimenter bias.

To address these limitations, we developed a novel machine learning (ML)-based image processing paradigm and software program, *Intellicount*, which dramatically reduces the time required for analysis, improves processing artifacts generated by simple image thresholding, and allows image processing to proceed without the need for carefully set thresholds. We have applied this in different experimental conditions. Additionally, *Intellicount* is packaged into an intuitive graphical user interface (GUI) that is equipped with commonly used statistical analysis and graphical figure representation, further increasing the efficiency by which quantitative analyses can be performed and data can be represented. As such, we provide the research community with an open-source, easy-to-use tool for quantification of fluorescent synaptic protein puncta. This open-source platform aims to improve the reproducibility and reliability in performing such analyses.

Materials and Methods:

Immunofluorescent (IF) sample preparation and image collection

Both mouse and human induced neurons (iNs) at different culture densities were used in this study. Specifically, low/medium density human iN cultures (~100,000 neuronal cells/78.5 mm^2) were prepared from male H1 embryonic stem cells (NIH registry WA01) as described previously for excitatory iNs [47]. Inhibitory iN subtypes were derived from C12 induced pluripotent stem cell (iPSC) lines as described previously [46]. C12 is an iPSC line originally created from a male subject from the COGEND collection [122, 123] of nicotine abuse as described previously [29]. It carries a minor allele variant in the OPRM1 gene (N40D), unrelated to the current study.

Coverslips were fixed at 6 weeks *in vitro* for IF experiments. Work with human embryonic stem cells was approved by the Rutgers Embryonic Stem Cell Research Oversight (ESCRO) committee. Mouse hippocampal neurons at relatively high density (~200,000 neurons/78.5 mm^2) were isolated from postnatal 0-1 C57/BL/6 background male newborn pups as described previously [124, 125] and fixed at the different time points after culturing (4, 6, 8, 10, 12, 16 days in vitro, DIV). Fixation was performed with 4% paraformaldehyde diluted in phosphate buffered saline (PBS) for 10 minutes at room temperature, washed well in PBS, blocked and permeabilized for 30 minutes in PBS containing 4% Bovine Serum Albumin (BSA), 1% normal goat serum, and 0.2% Triton-X100. Coverslips were then incubated with rabbit anti-synapsin (1:3,000, E028, a gift from the Südhof lab); rabbit anti-vGAT (1:500, Millipore Ab5062P, *RRID*:AB_2301998), mouse anti-MAP2 (1:500, Sigma M1406, *RRID*: AB_477171 and 1:1,000 Millipore AB5543, RRID: AB_571049) primary antibodies for 1 hour, washed well, and incubated in appropriate secondary antibodies (1:500, AlexaFluor 546-conjugated anti-rabbit and 488-conjugated anti-mouse, Invitrogen). All steps were conducted at room temperature. Coverslips were then mounted onto slides using Fluoroshield™ media containing DAPI (Sigma). Approximately 101.6 × 101.6 μm^2 Z-stack images (1024 × 1024 pixel resolution, 8-bit grayscale depth for human and mouse cultures were acquired at 1× digital zoom using a 63× water immersion objective by laser-scanning confocal microscopy (Zeiss LSM-700, Carl Zeiss, Dublin, CA). Mouse culture images for synaptogenesis time course were taken with 16-bit grayscale depth. All images were acquired using identical laser intensity, digital gain, and offset background

within each data set. Maximum intensity projection images were then constructed and images were exported in TIFF format for analysis in *Intellicount* or Fiji, which is a distinct package of ImageJ [126]. Subfields (~20 x 20 μm^2) were cropped from induced neuron images using Fiji for analysis by manual tracing to identify puncta ROIs. Fiji – fixed thresholding was performed using threshold settings 55 for lower threshold and 255 for upper threshold. For both manual and fixed thresholding methods within Fiji, ROI properties were analyzed using Analyze Particles.

Full, uncropped images from mouse cultures were used for analysis of synaptogenesis time course. For synaptogenesis time course, a total of 29-33 images were obtained from randomly sampled fields distributed evenly over two coverslips each obtained from two independent cultures. For high density vs. low neuronal density comparisons, images were taken from the same batches of hippocampal cultures at DIV 8. Fields with high cell density (more than 5 cell bodies) were selected for high density, and fields with low cell density (1-2 cell bodies) for low density images. For the calmodulin knock-down experiment, images were obtained from the authors of Pang et al. [3] which were acquired at dimensions of 71.3 x 71.3 μm^2 taken at 652 x 652 pixel resolution.

Image processing

Intellicount was developed using MATLAB 64-bit R2017a. The ML process uses a looped algorithm that optimizes traces against gradient images. Segmentation is performed in most cases on a filtered image (unless the user opts to forego the filter due to high background). Images are converted to a format with a normalized intensity range from 0 to 1 for all processing. Puncta IF intensities are re-

scaled to a 0-255 (8-bit images) range for display. Three thresholds (analogous to 8-bit grayscale values of 30, 70, 220) are then applied to the filtered image to generate three binary images. Next, the two upper threshold binary images are dilated according to the ML-defined dilation size. Following dilation, a 'background removal factor' is applied in order to reduce the capture of background signals from any threshold level. This serves to remove ROIs that do not have a significantly high gradient level. We hypothesized that true signals would have a gradient value greater than the average background signal. Therefore, any ROI that did not have an average gradient intensity higher than the background removal factor (on a 0.0 to 1.0 intensity scale), was removed from the binary image. Increasing this factor creates a stricter environment for puncta identification, and is recommended for high background images.

After dilation, the binary images are processed through a watershed transform to separate closely located puncta. Next, if selected, the MAP2 signal segmentation and correlation is performed. MAP2 segmentation is guided by Otsu's method [127], which determines optimal threshold values based on histogram variance of grayscale pixel intensities. An additional dilation of 1.5 mm (or other distance specified by user) is added to the width of segmented dendrites to capture puncta located near dendrites. Somata are also segmented from the MAP2 signal and either included or excluded from the correlation (as specified by the user). Remaining puncta undergo size discrimination.

While synaptic structures range in size from approximately 200 nm to 500 nm [128] as identified by electron microscopy [129], protein puncta visualized by confo-

cal microscopy generally range from 0.4 to 4 μm in diameter, based in part on the diffraction limit of light and inability to optically resolve closely adjacent terminals or spines. We established area cutoffs of 0.16 μm^2 and 6.25 μm^2 consistent with ranges used in a previous protocol [130]. This upper size limit can be altered within the GUI.

Since high intensity, non-optimized thresholds tend to capture only the brightest pixels of an ROI (Figure 4.1A,B), we applied our ML algorithm to improve ROI traces by comparing the overlap of all puncta traces of the image with

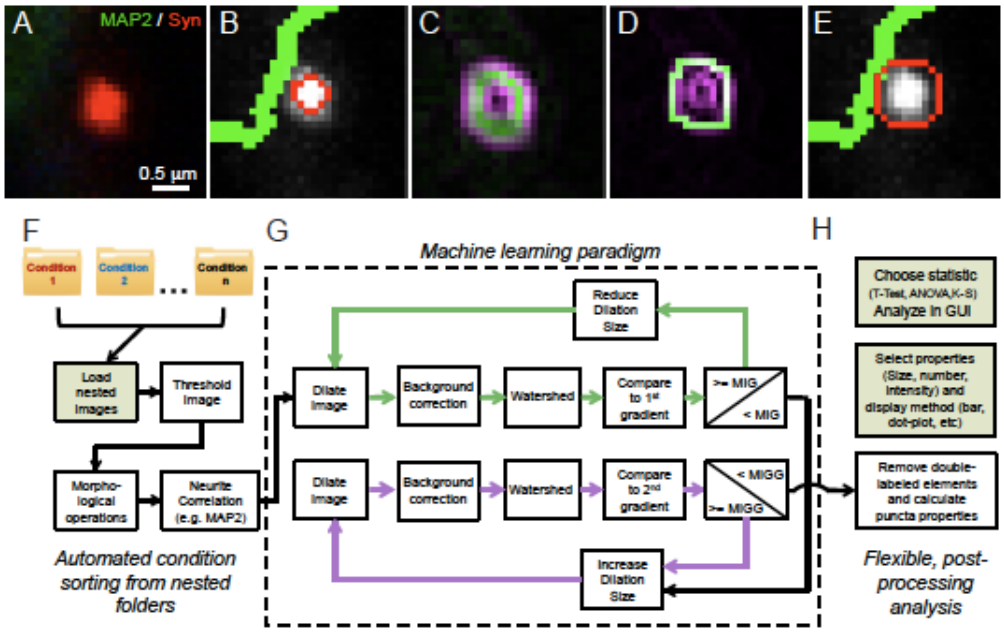

Figure 4.1. Machine learning facilitates high-throughput image puncta analysis. (A) Example synaptic puncta (synapsin in red) juxtaposed to a dendrite (MAP2 in green) and (B) a trace provided by thresholding. (C) First and second gradient (green and purple, respectively) provide a template. (D) Trace boundary is improved by structure-guided machine learning (optimized trace in green) overlaid on the second gradient (purple). (E) The improved puncta trace as a result of machine learning. (F) Nested folder input for image pre-processing sorted by data round (i.e., condition). (G) Structure-guided machine learning algorithm runs multiple dilation iterations to optimize traces (green and pink loops indicate processing against the first and second gradients, respectively). (H) Puncta properties are extracted and stored in matrix form, allowing flexible post-processing representation and analysis by the user (refer to Figure 6 for statistical output and data display). Note, this overall paradigm allows user to interact with the program at fixed beginning and end steps (highlighted in green shaded boxes).

the gradient images. Gradient images reflect the magnitude of the gradient of the original image using the imgradient command with the Sobel operator, which is a convolution mask applied to the image as described elsewhere [131]. Two gradient images are obtained: the first gradient which results in a single circular peak for each puncta (Figure 4.1C, green pixels), and the second gradient which results in two circular traces (Figure 4.1C, purple pixels). In the first round of ML, each successive ML loop alters the dilation size until there is maximum overlap between the ROI trace and the first gradient. The mean intensity value of the overlap with the first gradient is called the mean intensity gradient (MIG):

$$MIG = \frac{1}{n}\frac{1}{m}\sum_{i=1}^{n}\sum_{j=1}^{m}\nabla(\mathrm{I}_{i,j}) \cdot \mathrm{SI}_{E,i,j}$$

where $\mathrm{I}_{i,j}$ is a single pixel from the original grayscale image of the puncta channel and $\mathrm{SI}_{E,I,j}$ is a pixel from the edge-image of the segmented puncta (i.e., the puncta trace). The mean is determined using the mean of overlap for all pixels. Similarly, the second derivative (MIGG) is

$$MIGG = \frac{1}{n}\frac{1}{m}\sum_{i=1}^{n}\sum_{j=1}^{m}\nabla^2(\mathrm{I}_{i,j}) \cdot \mathrm{SI}_{E,i,j}.$$

Once the highest MIG value is found, the algorithm now increases the dilation size until the mean of the puncta trace multiplied by the outermost second gradient is maximized (Figure 1D). The trace that produces this maximized MIGG is used for all subsequent analysis, and the program considers the traces now optimized (Figure 1E). This process begins with threshold 2 and is repeated for threshold 3.

To ensure puncta identified by multiple thresholds are not duplicated in the final analysis, all multi-labeled elements produced from the multiple thresholds (puncta labeled by more than one threshold) are then removed by identifying objects underneath the highest threshold that identified the object. The results are then flattened into one binary image. From here, the MATLAB command regionprops was used to find properties of all identified puncta. The entire process is performed automatically, allowing the user to upload image folders into the program, and after selecting the "Start" button, performing plotting and statistical analyses (Figure 4.1F-H). The user may upload a single folder of images, or a folder containing subfolders of images, which we refer to as "nested folders". This expedites the analysis process by reducing user time uploading new batches of images for processing.

Computational run time analysis

This analysis was conducted on 10 cropped images. To collect run times for *Intellicount*, MATLAB functions tic and toc where utilized. For Fiji-fixed threshold, a macro within Fiji was recorded and run over the 10 images. The getTime command was used to capture the start and end times. The Fiji-manual approach was conducted using a manual step to optimize threshold selection. The threshold selection was timed separately outside of the macro for each of the 10 images. The identified thresholds were then added to the macro code, and the macro was run. The computational time and the threshold selection time were summed to capture total time for the Fiji-manual approach.

Statistical analysis

Data are presented as mean ± S.E.M. and statistical analyses were performed using one-way ANOVA with Tukey-Kramer post-hoc testing. Student T-tests in Figure 4 were performed in Excel using two-tailed equal variance. vGAT parameters expressed in text as mean +/- SEM.

Code Accessibility

The code/software described in this paper is freely available online at http://license.rutgers.edu/technologies/2018-013_intellicount. The code is available as Extended Data.

Results

Intellicount was primarily designed to allow IF image processing for quantification of synaptic puncta to proceed without the need for an experimenter to carefully set thresholds of IF signals and pre-select image subfields for analysis. Building off a previous approach using multiple thresholds [120], *Intellicount* uses a combination of multiple thresholding and puncta trace optimization aided by structure-guided ML. Multiple thresholds facilitate the separation of closely-located IF puncta and the inclusion of a greater range of intensities over variable background levels. Higher thresholds tend to capture the brightest regions (usually the center) of an IF punctum, leaving the less intense areas unaccounted for (Figure 4.1.B). Using the gradients as a structure guide (Figure 4.1C), we optimized puncta traces against the gradient (Figure 4.1D) to improve ROI identification (Figure 4.1E). Furthermore, *Intellicount* allows users to import full image fields arranged in folders according to experimental condition or different timings (Figure 4.1F). It then per-

forms image pre-processing to correlate to neural structures (dendrites) prior to ML (Figure 4.1G) and subsequently quantitatively analyzes the data and extracts the data for further statistical analyses with built-in statistics (Figure 4.1H). This highly-efficient approach greatly reduces the number of human interactions and thus lesser (or no) human bias and errors would be introduced by a user (user interaction points shown as green shaded boxes in Figure 4.1F,H).

Intellicount improves ROI tracing and quickly quantifies puncta number and properties

To test the accuracy of the synaptic structure identifications (tracing of the puncta) based on IF signals of defined synaptic proteins, we compared the synaptic IF puncta properties (synapsin and MAP2 IF images provided by *Intellicount* against manual, human traces and single thresholding methods in Fiji). Synapsin is a well-defined presynaptic marker and was used to quantify synaptic numbers in many recent publications [132-134]. Manual tracing for ROI identification was performed using ImageJ and Fiji [126]. First, we blindly identified all discernable IF puncta under high magnification, which enabled us to trace the ROI with accuracy down to the single pixel level. *Intellicount* was then run under three different conditions: no ML, i.e., simple thresholding using its default three thresholds; watershed only, which applies a watershed algorithm to thresholded images; and the *Intellicount* default (ML condition), which applies structure-guided ML with a watershed algorithm to the thresholded images. We also compared traces obtained using two different Fiji approaches: manually-selected thresholds for individual fields and a single, manually-fixed threshold (55 lower, 255 upper), with the Analyze Particles

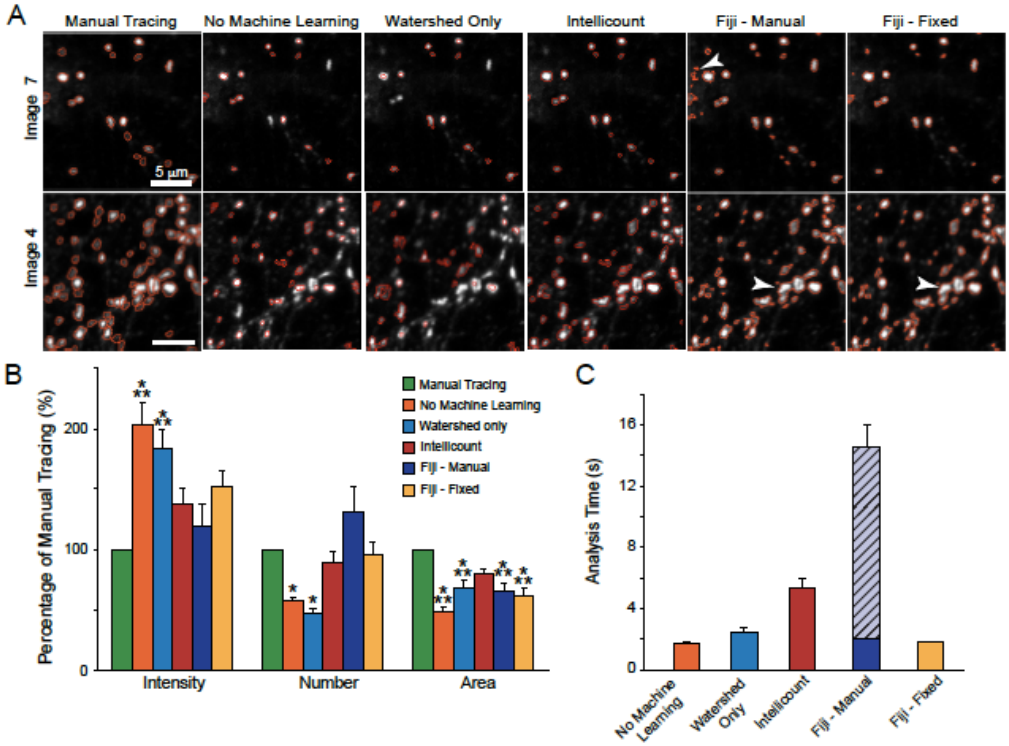

Figure 4.2. Comparison of *Intellicount*'s machine learning with manual traces and with Fiji. (A) Representative traces (red) provided by a manual tracing by a human observer, three processing conditions of *Intellicount,* and user adjusted variable- or fixed-threshold analysis in Fiji. Representative low (Image 7) and high (Image 4) puncta density fields are shown. White arrows indicate background included as region of interest (ROI, top row) and merged puncta (bottom row). Note, 'No Machine Learning' and "Watershed Only" provide traces obtained in *Intellicount* using default thresholds (without and with selection of a watershed algorithm, respectively) and without application of the machine learning. (B) Comparison of these processing techniques normalized to values obtained by manual tracing. Results are displayed as mean ± SEM from analysis of 10 random fields, * = $p<0.05$, *** = $p<0.001$ using ANOVA with post-hoc Tukey-Kramer, as compared to manual trace. (C) Total analysis time per cropped image performed on 10 fields. Computational analysis time is shown in solid bars, and was recorded either from MATLAB (for No Machine Learning, Watershed Only, and *Intellicount*) or Fiji macro. Diagonally-lined section of bar in Fiji-manual condition highlights the fraction of analysis time used for manual threshold selection.

tool within Fiji. We compared four parameters: number, area, and IF intensity, as well as average analysis time per image, over all six tracing approaches (Figure 4.2A**)**. Data were expressed as ratios compared to the manual trace. As expected, the machine learning (ML) version of *Intellicount* outperforms non-ML and watershed versions of the program on the three parameters for IF puncta (Figure 4.2B).

As compared to Fiji ROI segmentation, *Intellicount* performs comparably. Our program, however, largely circumvents common problems with single thresholds even when thresholds are carefully selected, namely, inclusion of background pixels and merging of closely located puncta (Figure 4.2A second row, white arrows). Multiple thresholds with watershed improved the separation of closely located synaptic puncta, while single thresholds can merge puncta together, which are then evaluated as a single, large ROI. *Intellicount* improves upon this, but does not fully separate all puncta as compared to manual tracing. While the areas quantified by Fiji and *Intellicount* were different from the manual trace, they were not significantly different from each other, although *Intellicount* may offer slight improvement over Fiji approaches.

In addition to defining the accuracy of *Intellicount*, we also compared computational processing time per image between methods performed in Fiji and *Intellicount* with the same set of 10 IF images. To evaluate one currently available method (single threshold segmentation using Fiji) against *Intellicount*, we used a macro within Fiji to quantify the computational run time. While runs of *Intellicount* with ML take slightly longer compared to runs without ML and to the Fiji macro, the timescale is within the same range of the other approaches[v], and provides the user with a greater amount of information in the process, such as data graphs (Figure 4.2C). To show the impact of manual operations on run time, we also added a thresholding selection step to the Fiji macro run time. The addition of

[v] While analysis time is within the same range for these images, it likely differs with images with more puncta. In general, the more puncta identified, the longer the Intellicount analysis.

this manual step, while only on scale of 10-20 seconds (diagonally-lined bar), significantly lengthens the time for processing images. This demonstrates that user interaction can slow data analysis time and that fully automated methods for large data sets are preferable. Furthermore, when considering full image analysis with MAP2 correlation, the differences between automated and manual approaches will likely be further extended, since automated approaches, and specifically *Intellicount*, have been designed specifically for this type of analysis and performs it automatically without optimizing other image channels or the need to crop subfields from full images. Therefore, *Intellicount* performs puncta IF analysis automatically while offering both accuracy and efficiency, with immediate data readout.

Intellicount identifies puncta over a wide range densities and intrinsic characteristics

To demonstrate the utility of the program to handle large data sets and its ability to discern puncta covering a wide range of sizes, intensities and densities, we performed a time course analysis of synaptogenesis and synaptic maturation using primary mouse hippocampal neurons. The total data set consists of 189 images generated from two different batches of cultures collected after increasing time spent in culture (4, 6, 8, 10, 12, and 14 DIV) with IF for synapsin (pre-synaptic marker) and MAP2 (dendritic marker), organized into six nested folders (each containing 29-33 images). Note that the number of the images in each nested folder can be increased dramatically as long as images could be acquired with the same parameters and format. The program ran these images with a MAP2 + Soma correlation, which includes puncta located within a defined distance from the MAP2 IF

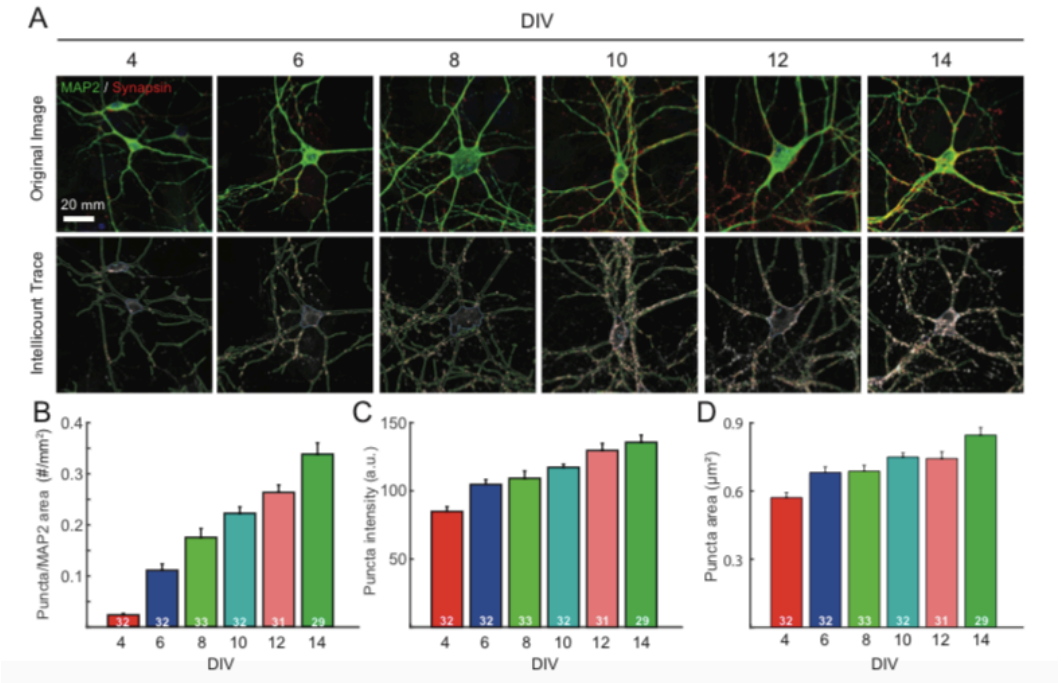

Figure 4.3. *Intellicount* recapitulates analysis of increasing synaptogenesis over time in cultured hippocampal neurons. (A) *Upper panels:* Representative images taken at increasing numbers of days in culture. *Lower panels:* Corresponding traces provided by *Intellicount* (red: correlated puncta synapsin traces, green: segmented dendrite traces in MAP2 channel, blue: trace of soma segmented from MAP2 channel. Display of the MAP2 channel was de-selected in the lower panels facilitate visualization of puncta. For synaptogenesis time course, a total of 29-33 images were obtained from randomly sampled fields distributed evenly over two coverslips each obtained from two independent cultures. (B-D) Quantification and graphical representation of (B) synapse number, (C) mean fluorescence intensity, and (D) area provided by *Intellicount* with minor adjustments in Adobe Illustrator® (renaming of "rounds" to appropriate conditions and thickening of stroke width for representation of graph and bar lines). Colors displayed are default in the program. Data are displayed as mean ± SEM. Numbers within bars indicate the number of images processed from that time point. Statistical comparisons were performed using Student T's test, * = $p>0.05$, *** = $p<0.001$.

signal-positive dendrite, as well as the segmented soma. The processing was completed in approximately 2.5 hours using an iMac with a 2.5 GHz processor. The background removal factor was increased from the default 0.175 to 0.25 to accommodate higher backgrounds found in later time points due to higher signal intensity. For output image traces, *Intellicount* displays the puncta channel in grayscale and the MAP2 channel at 50% brightness in grayscale (which can be toggled off, Figure 4.3), with the trace color matching the original color of the puncta channel. MAP2

traces are also shown in their original channel color, however the soma sizes are shown using a third unused channel color. Here, synapsin IF signal was shown in red (with red program traces in lower panel), and MAP2 IF signal in green (with green program traces in lower panel) (Figure 4.3A). Somata, which do not have a distinct channel, were traced in the unused RGB color, blue. An increase in synaptic density (number of puncta per unit MAP2 area) (Figure 3B), as well as increases in synapse area (Figure 3C) and synapsin fluorescence intensity as a function of time spent in culture were observed (Figure 4.3D). These results are consistent with previously published data on synapse maturation in a neuronal culturing system [124, 135].

Intellicount can be used under varied culture conditions and antibodies

To further demonstrate the robustness and reliability of the program to quantify synapses in images from different treatment conditions, we tested the program over three alternative conditions: 1) high vs. low neuronal densities, 2) IF imaging data collected by another research group with a defined molecular manipulation, and 3) images obtained using a different primary antibody, anti-vGAT with an alternative anti-MAP2 antibody. Fields with high and low neuronal densities were imaged from the same coverslip derived from mouse hippocampal cultures at DIV 8 of our synaptogenesis time course. High cell density images were considered dense if there were more than 5 cell bodies and MAP2 positive structures in the images. Low density images were considered low if there were only one or two cell bodies present and limited MAP2 positive area. *Intellicount* was able to detect puncta in both images (Figure 4.4A,B), showing comparable puncta area (Figure

4.4C). The program did however detect a slight difference in intensities between the groups. Interestingly, while the program did detect the increase in MAP2-positive area with the high density images, the synapse density was inversely correlated with MAP2-positive area (Figure 4.4C), which is consistent with a previous report [136].

To further validate the program, we obtained IF images from a previous report [3] to be processed in *Intellicount*. The original report demonstrated that there was no significant impact on synaptic properties after calmodulin (CaM) knock-down compared with control. To validate the program against this finding, we obtained approximately 50 images from both conditions, which were stained for MAP2 and synapsin (Figure 4.4D). *Intellicount* was able to accurately identify synaptic puncta within these images as well as MAP2 correlations (Figure 4.4E). The program did not detect any significant changes between all three synaptic parameters, as well as MAP2 area between control and CaM knock-down conditions (Figure 4.4F), confirming the finding from this report. The reproduction of this data serves as further validation for *Intellicount* and demonstrates its ability to reliably identify synaptic structures under different experimental conditions and culture types.

Lastly, we sought to demonstrate that alternative antibodies against synaptic proteins other than synapsin that could be used for tracing of synaptic puncta using *Intellicount*. We immunostained inhibitory human iNs for vesicular GABA transporter (vGAT) and MAP2 (Figure 4.4G,H). Sixty images were obtained from three different culture samples. Similar to synapsin quantification, vGAT IF puncta

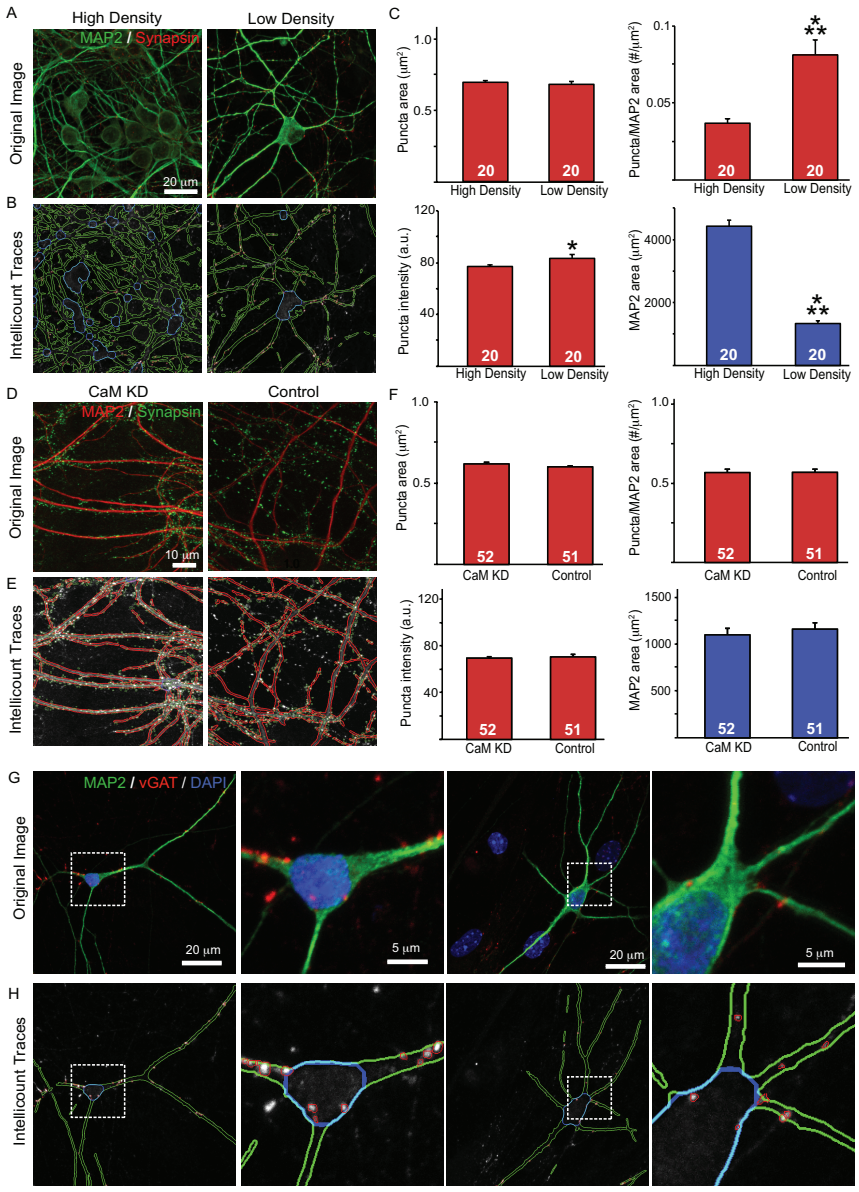

Figure 4.4. Validation of *Intellicount* under different culture and staining conditions. (A) Representative input images of high (left panel) and low (right panel) neuronal densities. (B) Corresponding traces provided by *Intellicount* demonstrating differences in segmented MAP2-positive areas. (C) Quantification of puncta number and properties (red graphs) provided by *Intellicount* under high and low neuronal densities. Total segmented MAP2-positive area shown in blue graph; n = 20. (D) Representative fields for lentiviral-infected calmodulin knock-down (CaM KD) and control (empty viral vector) expressing hippocampal neurons and (E) traces provided by *Intellicount*. Here, MAP2 "Show Correlation" is selected, which highlights MAP2 signal at 50% intensity level. (F) Quantification as in (C) displaying no differences in synapse formation as described previously[3]; n = 52 and 51 for calmodulin knock-down and control respectively. (G) vGAT staining (red) and MAP2 staining (green) in inhibitory human induced neurons. (H) *Intellicount*'s trace of vGAT puncta and MAP2. A total of 60 images were analyzed. White boxes show cropped areas for visualization. Numbers in bars indicate the number of images processed from that condition. Data are displayed as mean ± SEM. Statistical tests were performed using two-tailed Student's T-test, where * = $p<0.05$ and *** = $p<0.001$.

could be identified with apparent accuracy, quantified, and normalized to MAP2 signal (Figure 4.4G,H). The average area over the 60 images was 0.57 ± 0.11 μm^2 and the intensity was 72.7.±13.2 a.u.

Taken together, these data demonstrate the robustness of *Intellicount* to handle different sets of images collected, and that *Intellicount* can be used for a reliable quantification from different culture types and experimental conditions.

Intellicount automates post-processing analysis and data representation

To facilitate quantitative analysis of large data sets such as those demonstrated, we designed *Intellicount* to feature a user-friendly GUI, with automated figure generation and statistical output (Figure 4.5). Raw data can be exported directly to Microsoft Excel, which includes folder name, file name, and all averaged properties for each image, including MAP2 and soma characteristics. The "Save" button additionally allows the user to collect all raw data in a single, 4-dimensional

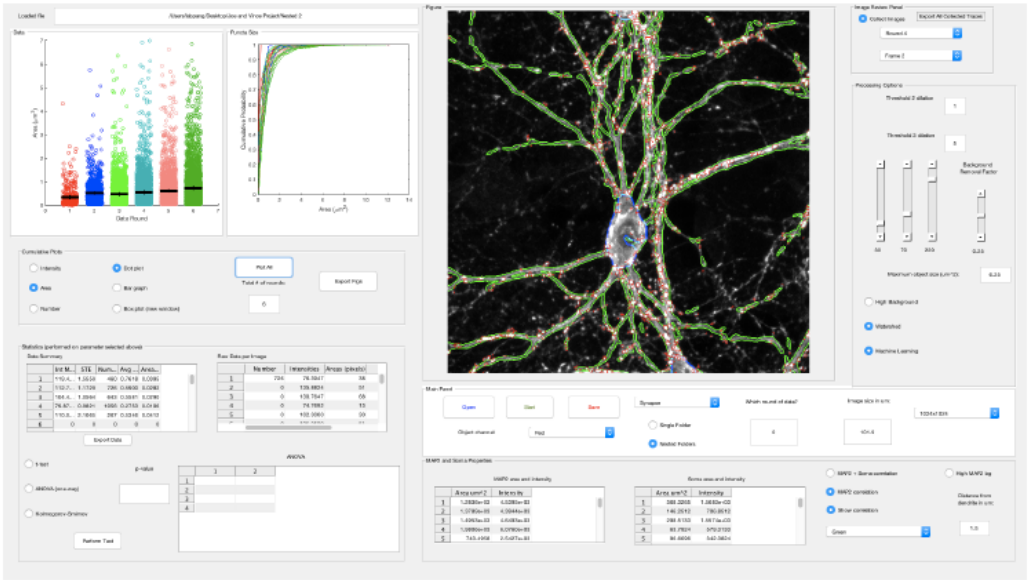

Figure 4.5. *Intellicount's* graphical user interface. Screenshot of the *Intellicount* analysis platform displaying results for synapse size from the synapse formation time course (Data Panel, upper left panels) depicted as dot and cumulative plots and an example analyzed field (Figure panel, upper middle pane). For details on operation, please refer to the user guide accompanying the software.

matrix retaining raw data of individual puncta associated with each image. Traces of images can be collected and exported using the "Collect Images" function, for display (as shown in Figure 4.3A, bottom row).

We designed *Intellicount* to provide a single user-friendly platform for immediate statistical analysis and graphical representation. Our program provides to the user three options for plotting data for each parameter measured (intensity, area, and number). The parameter and the output mode can be selected in the GUI prior to plotting. It can also display data as a bar graph, dot plot or box plot, as well as depict the mean and 95% confidence intervals of individual rounds for visual analysis of potential group differences (Figure 4.6). To highlight these plotting features, we utilized the area data obtained from the synaptogenesis time course in cultured mouse hippocampal neurons. The dot plot displays all individual results, showing the overall trend toward a corresponding increase in area over time (Figure 4.6A). Data round, which refers to the order of nested folders, is the default x-axis label. In this case, Round 1 is DIV 4, Round 2 is DIV 6, etc. Additionally, the data can be plotted as a cumulative fraction curve (Figure 4.6B) or as a box plot (Figure 4.6C). Boxplots are generated using MATLAB's boxplot command, where the red line indicates the median, the box edges are first and third quartiles. The dashed line edges, "whiskers", show the range of non-outliers. Outliers are plotted as single points in red. For individual images, a histogram of puncta area is automatically generated during analysis. Overlaying histograms for a single image from rounds 2, 4, and 6, shows again the trend toward a greater number and proportion of larger puncta (Figure 4.6D). Taken together, these features allow users to visually compare how

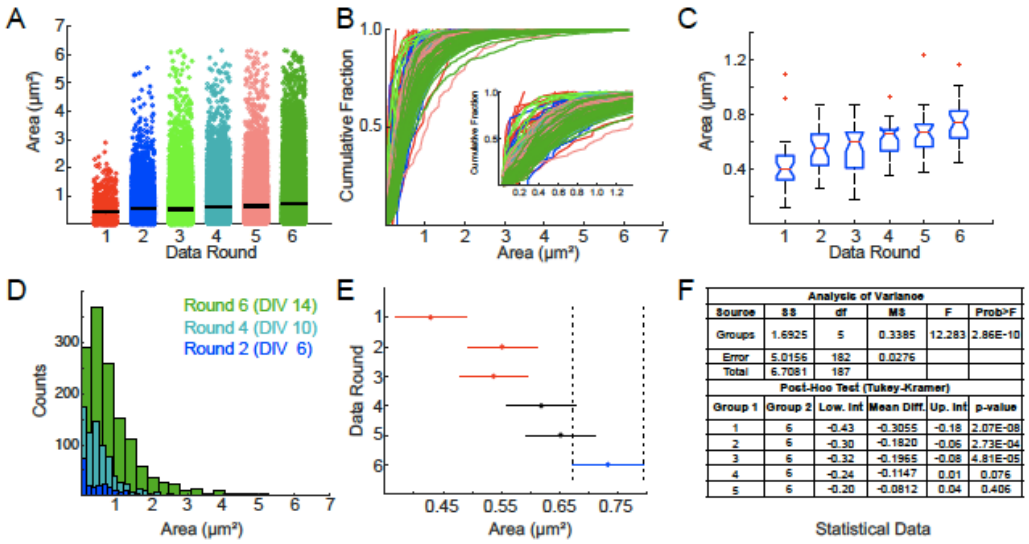

Analysis of Variance

Source	SS	df	MS	F	Prob>F
Groups	1.6925	5	0.3385	12.283	2.86E-10
Error	5.0156	182	0.0276		
Total	6.7081	187			

Post-Hoc Test (Tukey-Kramer)

Group 1	Group 2	Low. Int	Mean Diff.	Up. Int	p-value
1	6	-0.43	-0.3055	-0.18	2.07E-08
2	6	-0.30	-0.1820	-0.06	2.73E-04
3	6	-0.32	-0.1965	-0.08	4.81E-05
4	6	-0.24	-0.1147	0.01	0.076
5	6	-0.20	-0.0812	0.04	0.406

Figure 4.6. ***Intellicount*** **provides a multifunctional analysis platform with commonly used graphical data representation and statistical methods.** (A-C) In addition to bar graphs, data distribution can be directly visualized and exported as (A) dot, (B) cumulative fraction (for puncta area and intensity), or (C) box-and-whisker plots. Note, rounds here are reported according to folder nesting order and correspond to increasing time points in the synapse formation analysis presented in bar graph form previously (see Figure 3). (D) Histograms for areas of identified puncta are collected for each image for three increasing time points. Here, one image taken from three different rounds are overlaid to demonstrate the shift toward larger puncta during maturation. (E) Statistical comparisons can be directly performed in *Intellicount*'s analysis platform allowing visualization of significantly different groups. Rounds highlighted in red are significantly different from the round selected by the user in blue. (F) Computation of statistical test data including p-values for one-way analysis of variance and post-hoc analysis (Tukey-Kramer). Note, box notches (in C) and line lengths (E), define the boundary of 95% confidence intervals for the data and the mean for each round, respectively. Thus, in E, rounds colored with red (rounds 1-3) are statistically different (at $p<0.05$) from the round selected in blue (round 6), while rounds colored in black (rounds 4-5) are not.

puncta are distributed between rounds and within images. Additionally, when ANOVA is selected as the statistical test, the ANOVA table will display in the GUI. *Intellicount* also automatically runs the multcompare command, which performs a post-hoc Tukey-Kramer test for multiple comparisons between individual groups. This command generates a new window with a plot that allows the user to select individual groups (Figure 4.6E, blue line), displaying which groups have sig-

nificant differences (Figure 4.6E, red lines). Lastly, it will provide a table displaying the 95% confidence interval of the mean differences between groups and associated p-values between groups (Figure 4.6F), enabling the user to evaluate the level of statistical significance for all possible pairwise comparisons.

Discussion

Validated, high-throughput techniques allow researchers to generate, test, and evaluate hypotheses more rapidly and thus greatly advance scientific discovery. They also provide an unbiased, standardized platform for analyzing data sets and hence facilitate scientific rigor and data reproducibility. User-friendly bioimaging processing software tailored for specific platforms is in great need [137] and quantification of synaptic protein puncta visualized by IF (or a fluorescent tag) remains a widely used technique in neuroscience that is often cumbersome and prone to bias and human error. Semi-automated methods speed up this process, although there can sometimes be a trade-off between accuracy in tracing signals and processing speed. Importantly, thresholding methods may artificially reduce puncta size, capture background signal as ROIs, or miss low intensity puncta containing pixels beneath the threshold. To address these drawbacks, we developed *Intellicount* as an analysis paradigm and software program, which performs synaptic protein analysis of IF puncta via ML on a series of images of any size, providing data on the puncta number, mean area and fluorescence intensity. As we demonstrate, this platform provides an efficient and largely unbiased analysis of synaptic IF puncta that can be used for analyzing synapse formation across a wide range of puncta densities and properties under different experimental conditions.

ML for improved puncta identification

We developed *Intellicount* to employ an unsupervised structure-guided algorithm (i.e., guided by mathematical optimization equations rather than an empirical teaching approach) which corrects traces based on IF image gradients (Figure 4.1). Gradient magnitudes, which *Intellicount* uses as a structural template, are generated through application of a Sobel gradient operator. This approach focuses the puncta trace toward the periphery of the structure, immediately before an upward slope in signal occurs. Puncta size cutoffs and MAP2 correlation are applied prior to ML optimization, so that only the puncta of interest undergo ML optimization. By conjoining puncta identification with the MAP2 correlation, puncta over a wide range of IF intensities can be traced within a short distance of dendrites or neuronal somata.

Also demonstrated, *Intellicount* provides a rapid, multi-threshold analysis which is at least comparable to thresholding approaches in Fiji, however, providing improvements on puncta segmentation and background pixel inclusion (Figure 4.2). When compared to a manual trace, *Intellicount* was not able to re-capture the full area. While manual traces capture all (even very low intensity) pixels in the ROI tracing, *Intellicount* optimizes the trace according to the outermost second gradient, which may not include those very low intensity pixels. Furthermore, since the mean overlap between the trace of a puncta and the gradient is used to determine optimization, traces are most optimized for the average-shaped puncta in the image. Therefore, oddly shaped puncta, which can be traced with precision manually, may not be precisely traced using this approach. Nevertheless, the overall benefit of the

ML and image segmentation paradigm is evident by its ability to discriminate differences between experimental conditions efficiently and reliably without image cropping or carefully set thresholds.

Intellicount performs a robust analysis of different data sets

We also demonstrated that *Intellicount* is capable of handling a large data set of different experimental conditions (time points, molecular manipulations, culture densities and antibodies). Using synaptogenesis time course experiments (Figure 4.3) in cultured hippocampal neurons, we demonstrate that *Intellicount* can recapitulate relative differences between time points as shown in previous reports using other image-processing methods [124, 135]. Here, increases in both fluorescence intensity and puncta area are consistent with increases in synaptic maturation over time as can be observed by electron microscopy as increases in the length of synaptic contact zones and number of vesicles per synapses [138]. *Intellicount*'s ability to detect this increase demonstrates its utility for quantifying relative differences between conditions over a range of puncta densities and intrinsic puncta characteristics. The program captures low-intensity puncta from earlier time points as well as high intensity puncta of later time points, which is likely due to the use of multiple thresholds. Furthermore, *Intellicount* is able to recover most of the lost area through its ML optimization, which would likely be lost simply through default threshold-based segmentation alone (Figures 4.1,4.2). However, our program reaches a limit in its ability to segment puncta when the signal becomes saturated, a limitation of any imaging software that bases it's processing on signal intensities. If closely located puncta have saturated pixels with little intensity distinction between them, *In-*

tellicount will probably see these puncta as one. This is likely a caveat of any automated synaptic analysis program, and can be improved or eliminated through careful imaging technique and acquisition methods that do not result in significant signal saturation.

We further validated the program under different experimental conditions and reagents (Figure 4.4). *Intellicount* is able to comparably identify puncta from images containing regions of high and low neuronal densities derived from the same specimen (Figure 4.4), suggesting it is not substantially impacted or biased by cell density in ROI identification. In this analysis, we did observe a significant increase in the number of MAP2-correlated puncta in the low density condition, consistent with a previous report suggesting an inverse relationship between synapse density and neuronal number[136]. Furthermore, this experiment demonstrates that *Intellicount's* MAP2 segmentation function is capable of reporting differences in neuronal densities which can be a useful additional comparator for analyses (Figure 4.4C, lower right graph). To demonstrate that *Intellicount* can reproduce existing data sets and detect non-differences between conditions, as well as handle data obtained by other methods, we processed images from Pang et al. [3] in an automated format. Importantly, *Intellicount* was able to reproduce these data demonstrating that calmodulin knock-down does not significantly alter synapse formation in hippocampal neurons cultured at similar cell densities (Figure 4.4 D-F). Finally, to test the validity of *Intellicount* in tracing IF puncta visualized by a different antibody against a different synaptic protein, we performed vGAT staining on inhibitory in-

duced neuronal cultures [46] and observed punctate signals correlated to neuronal structures.

Collectively, these analyses demonstrate that the program is capable of running a variety of image sets obtained with varied neuronal densities, image acquisition methods, and primary antibodies for puncta analysis, with little adjustment in processing settings. Importantly, these results, just as those obtained from our synaptogenesis time course experiment, were obtained from full images without cropping images to capture specific locations or subfields and thus removing potential biases from the analysis.

GUI aids usability for data analysis and presentation

Immunofluorescent staining for synaptic markers often includes some diffuse signal in the cell nucleus or proximal neuronal processes, which can cause aberrant ROI identification. Therefore, we have also included a 'background removal factor' which discriminates ROIs using a gradient intensity image. True puncta signals should have a significant rise over background and a quick decay, which produces a high gradient intensity, which can be used to filter non-specific ROIs. Application of this background removal factor is most important when considering more saturated images and analyses where the somata are included. If it is set too low, it may include smaller background ROIs in the analysis, reducing the average puncta size. If set too high, the program will remove true puncta from the analysis. We therefore recommend that all users optimize this parameter prior to running data sets.

The "*Plot All*" option allows the user to visualize the data of the experiment in three ways for three puncta measurements (intensity, area, and number). These figures can be exported and saved as a variety of image types to assist in figure preparation. For data export, we have built in a button ("*Export Data*") which allows the user to capture data from all rounds and images. The data are compiled into a Microsoft Excel sheet, which is saved with a time stamp into the original directory, where the .m-file (MATLAB file) is located. This enables the user to capture data from a run for additional/alternative statistical analyses or other analysis outside of the GUI. Graphs produced in the GUI can also be exported. Overall, the GUI is designed to be as inclusive as possible, allowing a user to upload a full data set of either 8-bit or 16-bit RGB images and conduct a statistical analysis on that data set, all within a short time period.

We sought to provide the user with an easy-to-use interface (Figure 4.5) featuring common graphing options to compare groups, as well as built-in statistics for testing differences. Significantly, running individual images or individual folders adds time to processing a series of images, even in semi-automated programs. To maximize the efficiency of data processing, we implemented a nested folder input paradigm, which allows the user to upload a folder containing grouped subfolders of all images to be analyzed. *Intellicount* can be used for most common image formats (e.g., TIFF, JPEG). Resolution and image size (X and Y dimensions in microns) must be set prior to running the program directly in the graphical user interface. Importantly, there are no restrictions on field size or shape, which allows precropped images (from the same original dimensions and resolution) to be run to-

gether simultaneously, even if the cropped dimensions differ between images. For display of these cropped images in the GUI, *Intellicount* zero-pads the smaller images until they reach the largest column and row sizes of any given image. Therefore, a user can prepare a data set where each folder contains a different condition for analysis, and upload the entire experiment into the GUI at once, rather than sets of images individually. After the run is completed, the user can investigate individual images from each round in the GUI or export them by organized round into folders to evaluate the accuracy of traces of the identified puncta and MAP2.

Intellicount offers three statistical tests: Student's T-test, ANOVA, and the Kolmogorov-Smirnov (K-S) test for normality. Selecting ANOVA will also provide the user with automatic post-hoc comparison between groups using the Tukey-Kramer post-hoc test (Figure 4.6E). The K-S test can currently only be applied to single image area data. This option offers the opportunity to see whether the identified areas provide a sample of puncta from a normal distribution, as required for T-tests or ANOVA analyses.

Based on the design strategy, *Intellicount* has some limitations. While ML greatly improves identification of most IF puncta, not every punctum may be perfectly traced. The optimization is focused around the average-sized, rounded puncta and functions best on the brightest puncta where gradients are clearly defined. Secondly, since *Intellicount* utilizes thresholding as its primary means of segmentation, bright IF signals with low background are recommended for optimal processing, as is likely true for any IF image analysis program. Also, while the background removal factor can drastically improve high-background image results, there may be

a trade-off between puncta captured at the low intensity end if the background correction is set too high, and capturing some background pixels as ROIs if set too low. The user must determine how strict to set this cutoff for ROI identification, and some optimization may be required before running an image set. Also, we demonstrated that *Intellicount* is also able to segment dendrites and somata for correlation with identified synaptic puncta. Segmentation of dendrites and soma are performed based on the correlation channel staining. While *Intellicount* often successfully identifies somata in low density cultures, it may not as accurately segment them from high density cultures (Figure 4.4A,B), since closely-located dendrites may appear to the program as a distinct cell body. Inaccurate segmentation of somata may also occur when a MAP2 stain is used, as the intensity is often lower in the cell body than the dendrites. Thus, soma segmentation may not be optimal under all conditions (for example high density cultures, Figure 4.4B) and can be toggled on or off according to user preference. It is also important to note that the reported value for soma area is only the largest soma segmented from the image (see Additional comments in the User Guide). This is to reduce the impact of smaller, non-specific objects biasing the soma area results, which can be erroneously segmented from the MAP2 channel. Lastly, because the machine learning algorithm uses a built-in watershed segmentation, it can be subject to the plateau problem [139], resulting in the possible inflation of puncta number. If puncta tracing and number appear artificially inflated, this can be improved by toggling the "*Watershed*" option off, but at the risk of not achieving full separation between closely-located puncta.

Intellicount was designed to be a user-friendly, fully-automated program to perform synapse quantification and analysis. Built-in graphical and statistics features based off the MATLAB *Image Processing* and *Statistics* toolboxes offer a range of features for the user to automate data analysis without transferring raw data to a separate program. The nested folder option also greatly improves processing of large amounts of data. All these options taken together provide a robust program for high-throughput quantification of synaptic puncta.

Future Directions

While *Intellicount* is already fully-automated in its current capabilities with different imaging formats and conditions, we plan to expand its function to include co-localization and high-content imaging analyses. Furthermore, since *Intellicount* is primarily designed for quantification of puncta, only puncta number, area, and intensity can be displayed and analyzed in the user interface. We plan to improve soma segmentation and incorporate analysis within the GUI. Moreover, *Intellicount* features limited but commonly used statistical and graphical functions which can likely be extended in future versions. Finally, while *Intellicount* is optimized for identifying synaptic protein puncta in neurons imaged by laser scanning confocal microscopy, we would like to extend its versatility to be scalable to other imaging modalities (e.g., super-resolution microscopy) and applications such as cell counts and sub-cellular organelles, which will likely require further refinements in the ML design. Moreover, since we provide the research community *Intellicount* in an open source format, it can be used as a foundation for further improvement by the community.

Conclusions

We have developed and tested a novel program, *Intellicount*, which automates synaptic puncta analysis. Machine learning, which is built into the program, improves puncta tracing and minimizes operator error or bias. Furthermore, a nested folder analysis option and built-in statistics and graphical representation provide the user with a robust experimental analysis of puncta properties. All these features are contained within a single open-source GUI found online at http://license.rutgers.edu/technologies/2018-013_intellicount along with a simple user guide and thus offer a powerful platform for analysis of synaptic properties which will hopefully aid in the dissection of synapse formation under normal and disordered conditions.]

Production of hM3D Lentiviral Vector for Chemogenetic-based circuit stimulation

hM3D is a modified human muscarinic receptor type 3 designed to be exclusively activated by Clozapine-n-oxide (CNO). This DREADD approach enables researchers to activate a population of cells that uniquely express the receptor of interest. In the case of our devices, it serves as an analogous tool with optogenetics for circuit stimulation. Since the 96 well plate requires calcium imaging as its mode of activity readout, the FITC channel (488 nm) is occupied by the calcium indicator (GCaMP6). This conflicts with the excitation wavelength for channelrhodopsin 2 (ChR2), which is 470 nm. Therefore, recording calcium activity would

result in the constant stimulation of ChR2-positive cells, and no basal activity could be determined. To circumvent this issue, we chose to use hM3D/CNO instead of ChR2 for circuit stimulation. This also provides us with a means of demonstrating device utility in performing dose-response experiments.

Associated adenovirus (AAV) vector for hM3D was obtained from AddGene (pAAV-hSyn-hM3D(Gq)-mCherry, #50474), which contains hM3D under a human synapsin promoter, along with mCherry as a fluorescent reporter. Initial attempts at infection did not produce a measurable level of mCherry expression. Also, due to our extensive experience and success using lentiviral vectors, we decided to transfer the hM3D plasmid from the AAV into a lentiviral construct using a novel strategy called the Gibson Assembly.[140] Through this technique, we cloned

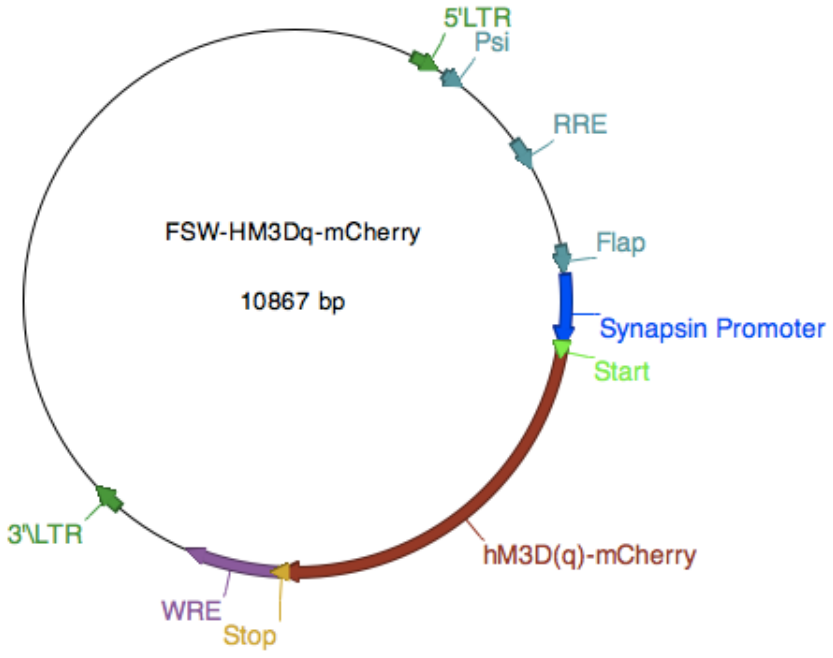

Figure 4.7. Lentiviral construct for hM3D as produced by Gibson Assembly. The hM3D with reporter and promoter were removed from the AAV backbone and cloned into a lentiviral backbone, according to this map.

the hM3D vector along with its promoter and fluorescent reporter into an empty lentiviral backbone (Figure 4.7).

Once the vector was produced, the virus was generated using the calcium phosphate transfection protocol described in Chapter 2. The virus was added to differentiating iPSC cultures, at a ratio of 100 μl/ml.

GCaMP6f was produced in a similar fashion and lentivirus was produced in the same manner. This virus was added to differentiating iPSC cultures at 200 μl/ml. Functional activity was seen within a few weeks (~3 weeks) after infection.

Together, these tools facilitate the high-throughput experiments described in Chapter 5. *Intellicount* was used for image processing, and GCaMP6f and hM3D lentivirus provided the means of recording and stimulating neuronal activity by calcium imaging.

CHAPTER 5: GENERATION OF A HIGH-THROUGHPUT 96 WELL PLATE MICRODEVICE FOR MORPHOLOGICAL AND FUNCTIONAL SCREENING STUDIES.

I have previously demonstrated that induced neurons can be co-cultured in distinct compartments of a microdevice. We have expanded this approach to develop a high-throughput circuit-based assay system which design for high-throughput screening (HTS) and compatible with HTS instrumentation.

Introduction

The use of human-derived neurons for modeling neurological disorders has grown in popularity, largely due to the ease of production and maintenance of induced pluripotent stem cells, as well as the capacity to preserve human genetic information relevant to disease. Much of the focus of human neurons has been toward mechanistic studies, uncovering disease etiology and the role of genetic variants in mediating disease phenotypes. This is important work, as greater understanding of mechanism will lead to improved therapeutic development.[33] In the brain however, neurons do not exist in as single populations alone, but rather in complex connected networks known as neural circuits. To further the end of improved therapeutic development, it is also important to consider neurons within this circuit context. For neuropsychiatric diseases, this is especially important since effects in one brain nucleus impact the total circuit function. Preservation of neural circuitry is an advantage of using *in vivo* models, but is done so at the expense of removing the human element from the study. Furthermore, given the lack of translation of psychiatric drugs through clinical trials due to efficacy issues, it behooves

the research community to develop novel *in vitro* models that can bridge the gap between single population and rodent models.

Many of these circuit models take their point of departure from work out of the Jeon group previously at UC Irvine.[82, 83, 141] While this compartmentalized device was designed for axonal injury studies, it demonstrates the utility of microfluidics as a tool for creating similar devices for neuronal communication studies. Since then, a variety of devices have been developed based on the same approach for neuronal injury and circuit studies.[1, 2, 88, 94, 142] These however have largely been proof-of-concept devices, and have not yet translated the function of these circuits to drug screening or disease-specific models.

Recognizing the need to scale up neuronal cell assays, human neurons have begun to utilized in high-throughput screening platforms.[41, 143-146] High-throughput systems have primarily been used for single cell populations, again focused toward extracting functional or morphological endophenotypes from an array of culture wells. These culture plates (e.g., a traditional 96 well plate) is limited when it comes to circuit studies, since it is difficult to compartmentalize small wells. While HTS of neuronal cultures offers the ability to screen more cells lines and more conditions, it comes with additional challenges. First, it produces a large amount of data that likely can only be analyzed with computer programs, of which is there is also a need for further development.[137] Second, electrophysiology of many cell lines and conditions becomes difficult without significant man-power, as the number of cells analyzed increases exponentially. There must therefore be analogous approaches for capturing the activity of cells in a network. The easiest method for

functional analysis in such systems is calcium imaging, since it does not require the use of expensive, multiple electrodes (in the case of MEAs) or multiple patch pipettes. Furthermore, performing the experiment is most easily done with an imaging system coupled to a liquid handling system, which is capable of introducing reagents into the wells in an automated format.

To address some of these limitations, we have created a neural circuit screening device designed to be coupled with a microscope/liquid handling system, the GE IN Cell Analyzer 6000. We used microfluidic technology to design a novel 96 well plate bottom which introduces two distinct compartments into a single well of a 96 well plate, separated by a series of microchannels. We demonstrate that different neuronal populations can be seeded in the different compartments, and that these cells can be used for functional and morphological screening assays. For a functional readout, we utilize genetically-enconded calcium indicator GCaMP6f, a fast acting indicator which fluoresces in response to increased intracellular calcium. To stimulate the circuit, we took advantage of a chemogenetic approach using designer receptors exclusively activated by designer drugs (DREADDs). Specifically, we used a mutated human muscarinic receptor type 3 (hM3D) which is a G-coupled protein receptor producing an excitatory effect upon stimulation by its designer drug, Clozapine-n-oxide (CNO). We demonstrate that we can achieve a circuit-level readout of calcium activity in excitatory-inhibitory two-way circuits, and that this circuit can be modified with receptor blockers or CNO. We also perform a synaptic quantification assay testing the role of neuroligin-3 overexpression on increased synaptogenesis. These assays are performed in a GE IN Cell Analyzer

6000, which is an automated confocal microscope with a liquid handling apparatus for reagent dispensing. Creation of this plate for the IN Cell system demonstrates the utility of microfluidics along with recent developments in genetic methods for neuronal stimulation and signal readout to serve as a platform for neural circuit studies and therapeutic development.

Results

Fabrication of the microdevice described in this chapter is discussed in detail in Chapter 2. Each well within the device contains two separate compartments, which form a binary circuit. The devices were seeded by adding 10 μl of suspended cells to a particular side, and 10 μl of a second type of cells to the other side. Five hours were given to the cells to complete their attachment to the surface. After five hours, medium was added to the well. Since the microwell compartments were small, and only a small volume could be added while seeding, we wanted to confirm that neurons did not cross the microchannel-wall either during seeding or after medium is added. To test this, one excitatory neuronal population was seeded against other. Neurons in the left chamber were infected with red fluorescent protein (RFP) lentivirus, to aid in visualization of their position within the two-compartment device. After approximately 4 weeks in culture, RFP-labeled axonal projections were seen traversing the microchannels. Importantly, these RFP-labeled neuronal cell bodies were contained to the left side of the device (Figure 5.1a,b). Examination of an entire well revealed that the seeded neurons spread out within the entire chamber but do not cross into the opposing chamber (Figure 5.1c). This validated the seeding protocol in generating this compartmentalized model.

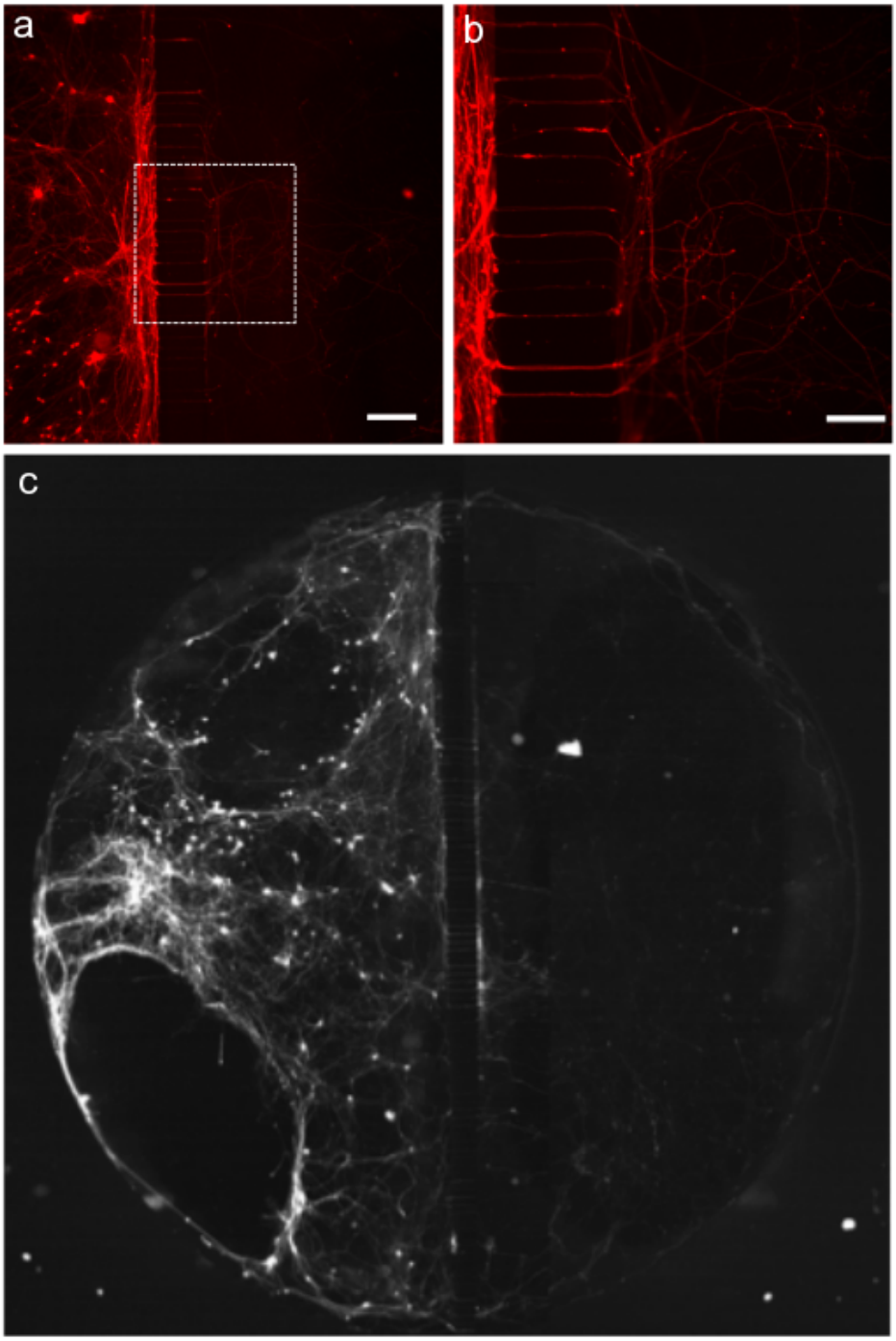

Figure 5.1. Seeding protocol preserves compartmentalization of distinct neuronal populations. a) RFP-infected excitatory neurons in left side of well project axons through microchannels but no cell bodies cross to the other chamber. b) Inset of a). c) Full well of 96 well device stitched together for visualization. RFP-labeled excitatory neuronal identity in the left side only is preserved at 4 weeks of culture. Scale bar represents 100 μm.

We next wanted to determine the functionality of the circuit formed between the two chambers. To do so, we paired excitatory neurons with inhibitory neurons in each well. Both neuronal populations were infected with GCaMP6f, which enables visualization of calcium signaling. Neuronal circuit within the plate were cultured for 5-6 weeks prior to analysis. In order to use calcium imaging as a high-throughput readout, it is convenient to have access to a semi-/fully-automated system for data collection. For these experiments, we used the IN Cell Analyzer 6000, an automated confocal microscope with limited liquid handling operation. To capture both chambers in the excitatory-inhibitory circuit, we used a 2048 x 2048 window spanning the 500 μm width of the microchannels and capturing approximately 200 μm additionally on either side of the wall. This provided enough cells within the field to measure circuit activity from both neuronal populations. Baseline activity was captured for 2 minutes. After 2.2 minutes, CNQX was added to the chamber at a final concentration of 20 μM, and an additional 3.3 minutes were recorded. During the recording of basal activity, neurons in both chambers were seen showing individual spontaneous activity as well as circuit activity (Figure 5.2). Importantly, this circuit activity was coordinated between chambers, indicating that axons have traversed the microchannels and formed synaptic contacts on neurons within the opposing chamber, while maintaining subtype distinction within individual compartments. Excitatory neurons demonstrated low frequency circuit bursts that influenced inhibitory neuronal circuit firing. Inhibitory neurons were seen showing more frequent activity, but most of their firing was due to coordinated

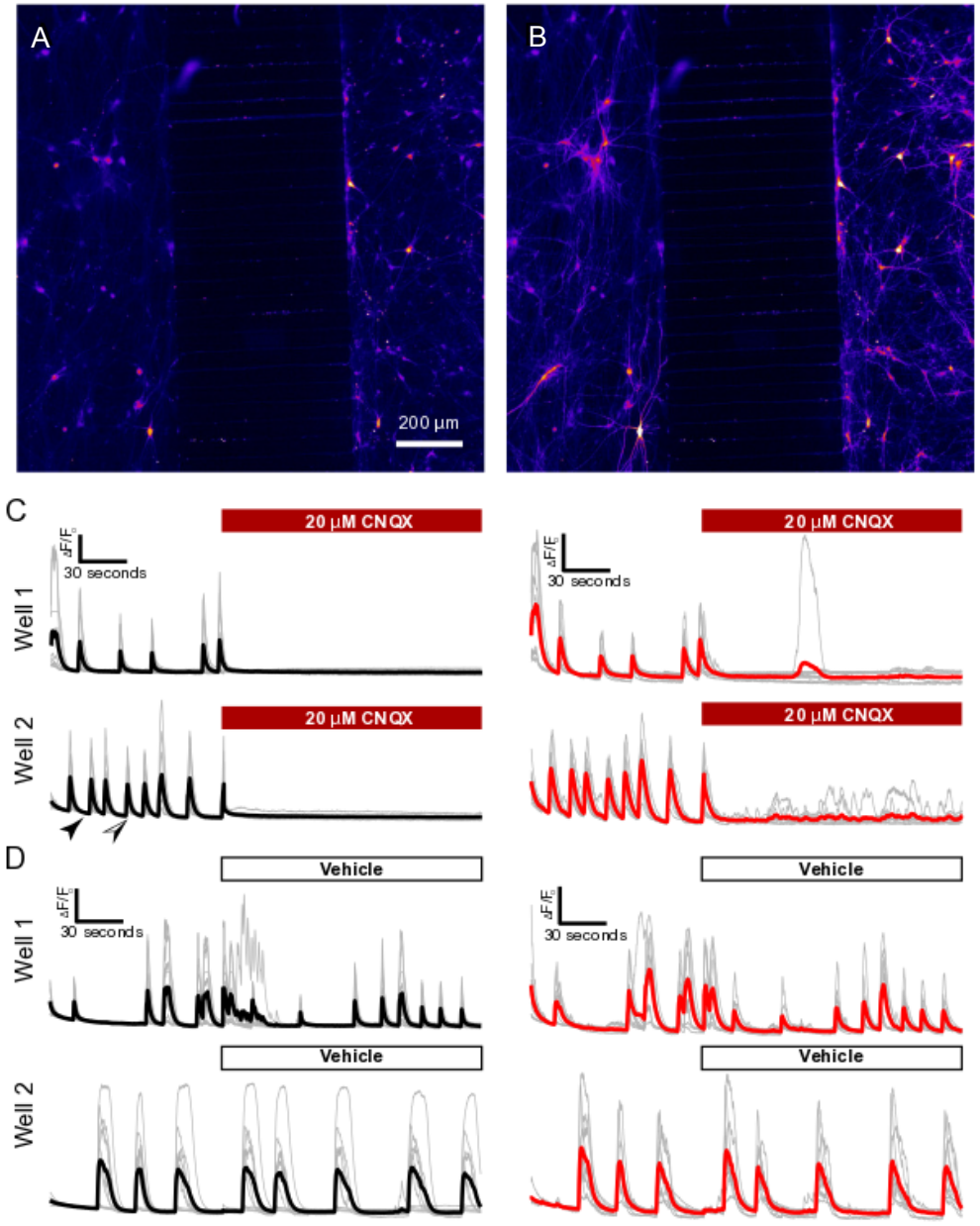

Figure 5.2. Spontaneous circuit activity and disruption by CNQX. A-B) Excitatory neurons cultured on left side, inhibitory neurons on right side. Frames correspond to specific times indicated in C. Black arrow corresponds to time at frame in A, and black/white arrow corresponds to frame B. C-D) Traces acquired from representative cells in two different wells. Average trace for excitatory neurons shown in black, with gray traces indicating the cells averaged. Inhibitory neurons shown in gray, with a red average trace. CNQX or vehicle added after 222 seconds.

stimulation from the excitatory side. This basal activity was maintained over resting conditions. With the addition of glutamate receptor (AMPAR) antagonist CNQX, the circuit was disrupted, and excitatory neurons were no longer able to coordinate large circuit bursting activity. Inhibitory neurons were secondarily impacted by the CNQX, as they were not receiving excitatory output from the other chamber. They were however still able to regain basal activity, but in a non-coordinated format. In some cases, inhibitory neurons displayed a regular pulsing activity, which was maintained in the presence of CNQX, but this was not seen in all experiments.

Utilization of DREADDs to demonstrate drug screening capability

Receptor blockers demonstrate the ability to manipulate a neural circuit according to a defined mechanism. This shows that we have created a functional neural circuit model that can be manipulated by the experimenter. Next, we wanted to show the capacity for stimulating the circuit through the addition of small molecules or drugs. To demonstrate the utility of the device for drug screening, we took advantage of a chemogenetic approach. Previously, we had demonstrated that neural circuits can be manipulated using optogenetics. In the microplate, however, calcium indicators must be used for functional readout, since there is not enough space for patch clamp and since electrophysiology is difficult to scale as a high-throughput method. Optogenetic receptors (here, ChR2) requires an excitatory stimulus of 470 nm, which is too close to the stimulation wavelength of GCaMP6f (470 nm), or other commonly used fluorophores such as Fluo-4AM. DREADDs uses an analogous technique through G-protein coupled receptors instead of ion

channels. Typically, the response is not immediate to the presence of the drug (CNO), as there is time needed for the receptor's downstream cascade to activate the cell.[62] To use the DREADD hM3D, we first cloned the hM3D sequence along with its mCherry reporter into a lentiviral construct. We infected excitatory neurons with hM3D, and paired them within the circuit model with unlabeled inhibitory neurons. Both sides were stained for MAP2 and vesicular GABA-transporter (vGAT), a marker for inhibitory neurons. Inhibitory neurons stained positive for MAP2 and vGAT puncta, but were negative for the mCherry reporter (Figure 5.3). The excitatory side was also positive for MAP2, but negative for vGAT and positive for mCherry. This confirms the presence of two distinct populations of neurons cultured in the same well while in different compartments, and that excitatory neurons express the hM3D-mCherry construct.

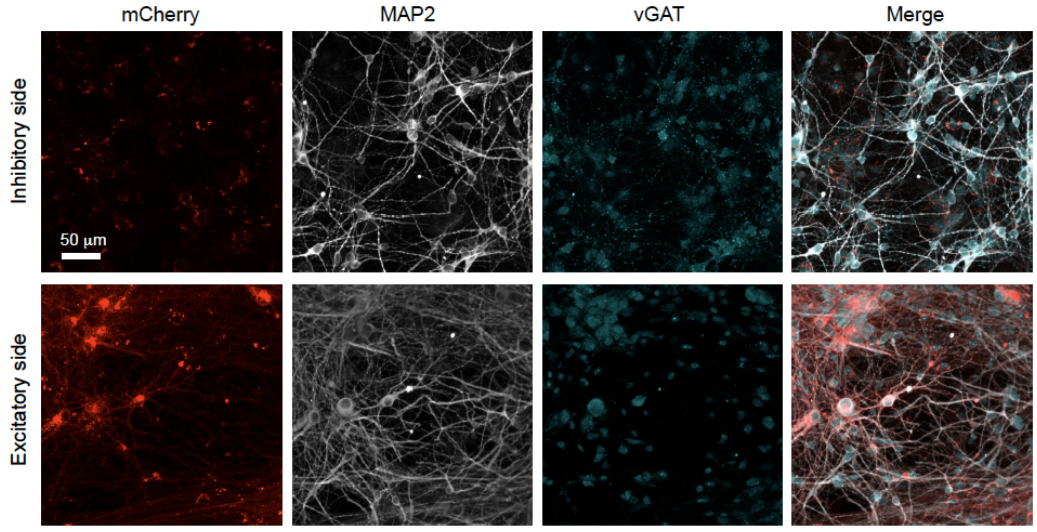

Figure 5.3. Morphological analysis of DREADD-based circuit model. Inhibitory and excitatory neurons were stained for MAP2 and vGAT. mCherry reporter indicates presence of hM3D. Excitatory neurons, infected with hM3D lentivirus, were mCherry-positive and MAP2-positive, but vGAT-negative. Inhibitory neurons were MAP2- and vGAT-positive, but mCherry negative.

Clozapine-N-oxide (CNO) at varying concentrations, Clozapine, or vehicle were added to the system to measure network stimulation. CNO concentrations ranged from 500 nM to 0.8 nM; Clozapine was added at 500 nM final concentration. The blank vehicle was a small percentage of DMSO mixed with HEPES, which was designed to match the maximum volume of DMSO present in 500 nM sample conditions of CNO and Clozapine. Calcium imaging was performed in the same manner as described above. Basal activity was recorded for 100 seconds, after which the drug was added. An additional 2.75 minutes were then recorded to capture the effect of the drug. After image collection and merging, region of interest tracing was performed manually using ImageJ. Individual cells were processed as $\Delta F/F_0$ by using the minimum intensity value from the first 200 frames. For quantification before and after the addition of the drug, two 90 second windows were captured. The pre-window was from 8.8 seconds to 98.8. The post-window was from 173.8 seconds to 263.8 seconds. Signals obtained from each window were processed by a custom MATLAB script. The number of peaks were difficult to quantify, since there were either large bursts of activity spanning 10s of seconds and likely were several action potentials merged together, or no network bursts seen prior to drug addition. When there are no peaks before drug addition, it is impossible to establish a ratio of firing based on peak number. Area can also be used as a quantification of total charge transfer. It may also be subject to inflation if there were no network peaks prior to drug addition, however small basal activity can still be quantified by area. To normalize all signals to the baseline, I used built-in MATLAB function `msbackadj` followed by `trapz`, which uses the trapezoid

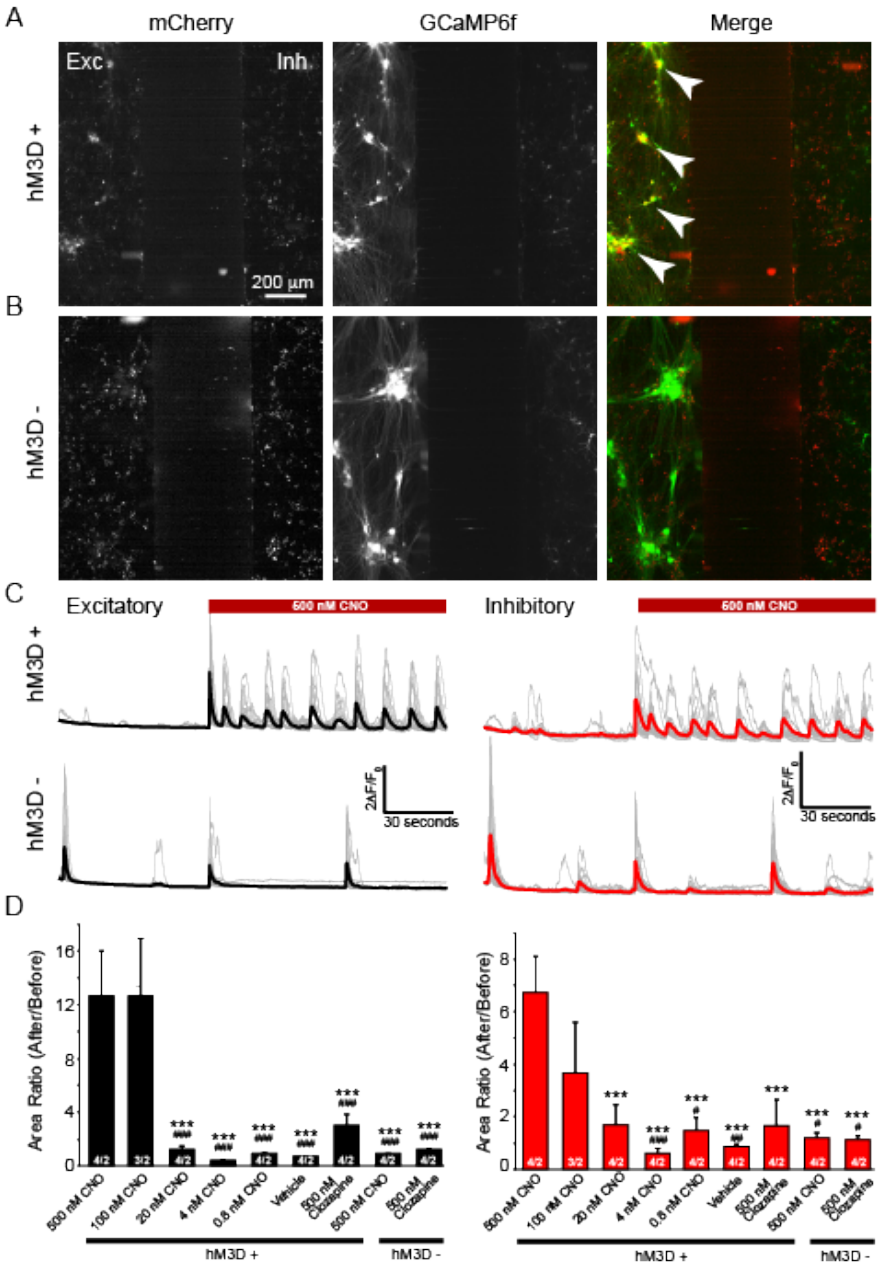

Figure 5.4. Use of hM3D to screen different concentrations of CNO and Clozapine. A) Representative frames from a hM3D-positive well. mCherry served as the reporter for the hM3D receptor. GCaMP6f is present in functional neurons. The Merged images show co-localization between mCherry and GCaMP6, indicating functional neurons expressing hM3D. White arrows reference regions of co-localization. B) The same set of frames from an hM3D-negative well. No co-localization is seen. C) Traces from hM3D-positive and negative cells. Gray traces show individual cells. Solid traces show average for identified cells. Excitatory neurons are averaged in black and inhibitory neurons in red. CNO is added at 100 seconds (frame 900). D) Area ratio quantification for Excitatory neurons (black bars) and inhibitory neurons (red bars). Ten cells were processed from 3-4 wells over 2 plates. *** indicates $p<0.001$, as compared to the 500 nM CNO with hM3D data, ### for $p<0.001$, ## for $p<0.01$, and # for $p< 0.05$ as compared to the 100 nM CNO with hM3D data.

rule to integrate signals. Results were processed as (area of post-drug)/(area of pre-drug) over all conditions (Figure 5.4). While there was much variation between wells of the same condition, concentrations 500 nM and 100 nM of CNO showed significantly ($p<0.01$) larger bursting activity after CNO addition compared to controls. Other concentrations did not show any significant results. Clozapine at 500 nM did show an increase in area, but was not significantly different from the vehicle. Importantly, high concentrations of CNO showed significant differences from both vehicle with hM3D-positive cells and 500 nM CNO with hM3D-negative cells. Responses to drug of any kind were however quite varied. This is likely due to intrinsic variability in the culture model. Inhibitory neurons showed a similar response. Higher CNO concentrations showed significant differences compared to vehicle and hM3D-negative cells (Figure 5.4D).

Lastly, we desired to demonstrate the utility of the device for a morphological assay on neurons with defined genetic backgrounds. A previous report has demonstrated a substantial increase in synapse number with increased neuroligin-3 wild type, but not neuroligin-3 with point mutation R451C.[107] We decided to use lentivirus to deliver wild type neuroligin-3 (NL3-WT) or neuroligin-3 with R451C (NL3-R451C). Control iPSC lines were infected to produce excitatory neurons. Induced neurons then underwent additional infections. Synaptic-vesicle 2 with conjugated GFP (SV2-GFP) was used to pair against all different NL3 conditions in the opposing chamber. SV2-GFP enables visualization of axonal projections from one chamber to the other for synapse formation. Three populations of excitatory neurons were paired against SV2-GFP neurons: NL3-WT, NL3-R451C, and an ex-

citatory control which did not have any additional NL3 expression. All NL3 lentivirus also possessed an HA tag, for identification by staining. Devices were cultured for 5 weeks prior to staining for MAP2, synapsin, and HA. Unfortunately, the HA stain produced high background between all three groups and was not used in the quantification or for qualitative validation of NL3 expression. Synapse number as defined by synapsin-positive puncta co-localized within a defined region of MAP2 signal (1.5 μm away from dendrite) was used as the metric for synapse number. Two batches of cells were used quantification: batch 1 contained 3 wells per condition and batch 2 contained 4 wells per condition. Between 2-4 images were taken as Z-stacks from each side of the well in the IN Cell Analyzer 6000. Images were merged and formatted as maximum intensity projections. The left side containing SV2-GFP neurons served as an internal control for synapse number. (Since NL3 is a post-synaptic marker present on dendrites, it did not have an impact on the number of synapses within the SV2 neuron chamber, therefore making it a meaningful internal control.) I used the previously described *Intellicount* program for quantification of synaptic puncta. A background correction factor of 0.25 was used to prevent the inclusion of the high background in the synapsin channel. The quantification was able to reproduce a trend consistent with previous literature, however there was no significant differences between any groups (Figure 5.5). Variation between and within wells was large enough to impact group differentiation. However, this experiment demonstrates the use of the device to perform a morphological assay within the IN Cell Analyzer 6000.

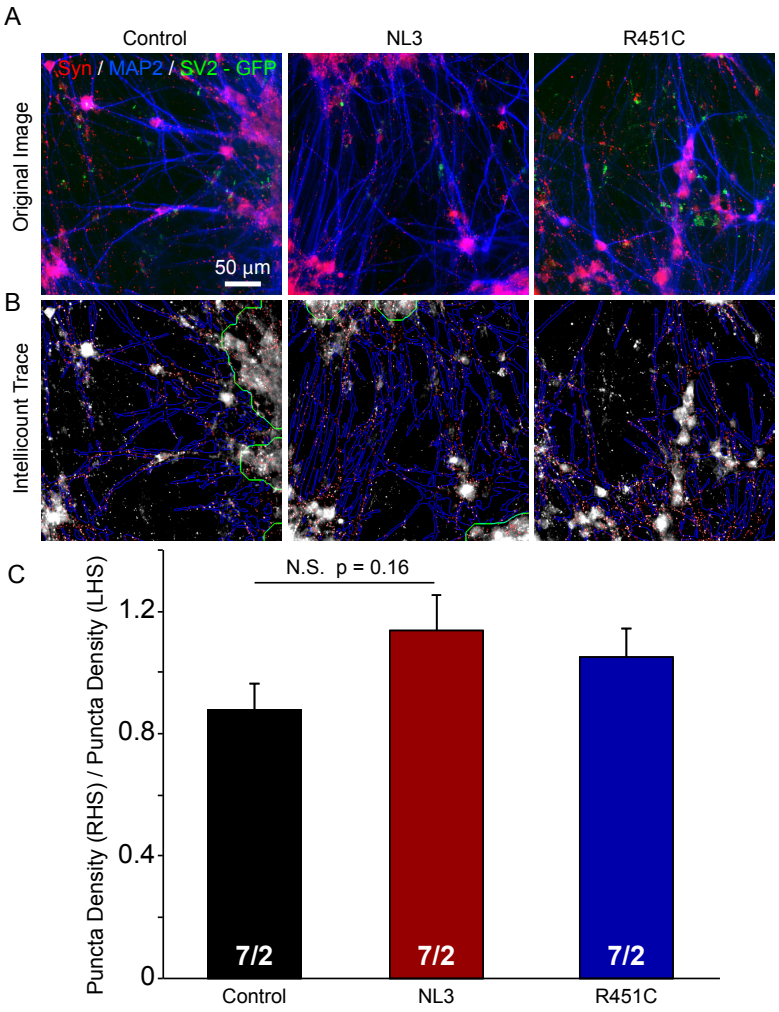

Figure 5.5. Neuroligin-3 synaptic quantification experiment. A) Original traces obtained from the IN Cell Analyzer 6000. B) Traces produced from Intellicount. Synaptic puncta identified are traced in red, MAP2 in blue, and identified somata in green. C) Quantification of the puncta density. Right-hand sides (RHS) were divided by their corresponding left-hand sides (LHS) to produce the density ratio. N.S. indicates non-significance.

Discussion

The advent of induced neuronal technology has provided an important step towards the understanding and modeling of neuropsychiatric diseases. Progress has been limited, and much of our understanding is based off animal models or brain imaging. This indeed provides some information with respect to the brain regions

which are targeted and the role of affected neural circuits, but in spite of this progress, there has not been significant translation of effective therapeutics from the pharmaceutical industry to those in suffering from disease. To bridge this gap, greater understanding of disease mechanism within human neurons, produced from iPSC lines, and better modeling systems are in dire need. To that end, we have developed a high-throughput compartmentalized system for circuit studies. This device builds on previous approaches using microchannels to segregate cell bodies while enabling axons to communicate between chambers.[1, 2, 82, 83, 94, 141] To our knowledge, these previous compartmentalized devices have not been used for high-throughput screening studies. Our device has two-compartments built into each well within a 96 well plate. Neurons seeded into the device remain in distinct compartments up to 7 weeks in culture after plating (Figure 5.1). Importantly, these neurons establish functional synaptic contacts and coordinate network activity between and within compartments (Figure 5.2). We demonstrated, through the addition of AMPA receptor blocker CNQX, that glutamatergic activity can be disrupted within the circuit, and that this disruption impacts the networks ability to coordinate signals, even in the inhibitory neuronal chamber. Since the IN Cell Analyzer 6000 is physically adding reagent to a still well, we wanted to confirm that the addition of liquid itself was not disturbing the system. We therefore delivered vehicle (HEPES buffer) in the same volume to the microwells. Delivery of vehicle only did not effect the circuit, which was able to maintain ongoing microwell-wide network activity. Additionally, we also wanted to confirm that there were no differences between left and right chambers in the way the IN Cell Analyzer handles neu-

ronal cultures and captures images. We therefore altered the orientation of the circuit (e.g., excitatory on the left and inhibitory on the right and vice versa). The orientation had no impact the outcome of the experiment. Both orientations produced the same effects with regard to addition of CNQX (and CNO/hM3D) treated cultures Interestingly, while CNQX remains in the well for the duration of the experiment after the addition, there was one instance where after approximately 2.5 minutes, excitatory neurons were able to coordinate activity to produce network signaling. This is likely to due the adjustment of the neurons to the presence of the CNQX and the reestablishing basal activity.

We designed the device to function as a screening system for therapeutic development. To that end, we tested specific receptor-ligand interaction. We did not want to choose a receptor that would be present in neurons within both sides of the device. That way, there would be no opportunity to stimulate neurons of one chamber versus the other. To control the cells we were stimulating, we utilized the technique designer receptors exclusively activated by designer drugs (DREADDs), specifically hM3D/CNO. DREADDs have been used for a variety of studies, but have recently come under skepticism, since the exact mechanism of action has been unknown.[55, 56, 58-60] Gomez et al. recently demonstrated the differences between Clozapine-N-oxide (CNO) and Clozapine, a metabolite of CNO. They demonstrate using both human embryonic kidney cells (HEK293) *in vitro* and mouse *in vivo* experiments, that Clozapine has a much greater reactivity and affinity for the hM3D receptor than does CNO. CNO, they argue, likely only reacts with hM3D at high concentrations due to its ability to convert to significant Clozapine levels for bind-

ing hM3D. We therefore included Clozapine within our drug screening study to investigate its activity over against CNO.

Originally, we obtained an AAV-hM3D from AddGene (pAAV-hSyn-hM3D(Gq)-mCherry, Plasmid # 50474 deposited by Roth Lab). After several infected attempts, we were not able to demonstrate the presence of mCherry within infected induced neurons. To create a lentiviral construct, we used Gibson Assembly to transport the hM3D-mCherry sequence from the AAV backbone to the lentiviral backbone. Having successfully completed the cloning, we next wanted to show expression of hM3D-mCherry lentivirus, and that neurons infected with the DREADD virus remained within their distinctive compartments. To do so, we fixed and stained microwells for vGAT and MAP2 and imaged both chambers within the well. Excitatory neurons only showed the presence of mCherry throughout the entire neuron, indicating successful cloning of the hM3D-mCherry sequence as well as the ability to co-culture infected iNs with non-infected iNs in the same microwell. These neurons demonstrate a robust response to high concentrations of CNO, but little to no reaction to doses lower than 100 nM (Figure 5.4). This is consistent with Gomez et al., in that it accords with their determined EC50 value of 85+/-17 nM established in HEK293 cells. Clozapine however did not have as substantial of an effect, although predicted by results from Gomez et al. There may be a slight increase in activity in DREADD-infected neurons, but not enough to generate a statistically significant response. One point of difference between our experimental setup and that of Gomez et al. is that we are performing this experiment in induced neurons cultured within a network. The basal function of the network gov-

erns the overall functionality of the circuit, and, even under conditions of disruption or alteration, such as adding a drug, neurons within a circuit still control the level of network output in the culture. This is not the case with HEK cells, which do not form circuits, but are primarily used as a heterologous expression system. Also, Gomez et al. infected cells with associated adenovirus (AAV), whereas we used lentivirus. Lentivirus is capable of greater infection rates, and so it is difficult to compare the number of receptors present on any given cell, and therefore that cell's response to CNO or Clozapine. The report by Gomez and colleagues provides a beneficial and interesting comparison, highlighting the need for further investigation of the role of hM3D, CNO, and Clozapine. In spite of these differences, our goal was to demonstrate the formation of neural circuit model within a microdevice that can be subjected to high-throughput screening assays conducted within an automated instrument.

In addition to functional analyses, we wanted to demonstrate the capacity of the plate to serve as a morphological screening platform. To do so, we used lentivirus to over-express neuroligin-3, both wild type and R451C (Figure 5.5). We used fluorescent synapsin puncta correlated to MAP2 as a metric for synapse density. Our program, *Intellicount*, was able to discern differences between culture conditions, but the assay did not produce statistically different results. This is likely not a caveat of the microplate as an assay system, but rather a limitation of the lentiviral constructs and cell culture setup. Furthermore, we were not able to confirm the presence of over-expressed NL3 in any condition. Also, it is likely that the cell density plated into each compartment was too high for morphological analysis.

Reduced cell densities would serve to elucidate the precise synaptic contacts being formed rather than saturating each chamber with synapses.

While the 96 well plate device has advantages over other systems, it also possesses some drawbacks which require optimization. One element of the approach of using different neuronal subtypes in high densities, is that there is a lot of intrinsic variation within each well. This may be due to well location within the plate, but more likely it is a product of biological variation or differences between stem cell infection rates. This could be resolved by increasing the number of wells per condition, but at the expense of lengthy experimental run times. It would be best to regulate as much as possible the production of the device and production of induced neurons (iNs). With consistent devices and iNs, variation may be reduced. Furthermore, since the IN Cell is not capable of complex liquid handling operations, many manual steps must be performed during calcium imaging analysis. These steps further extend experimental run times, keeping the cell cultures in HEPES buffer at room temperature for up to 6 hours. While cultures still demonstrated spontaneous activity in a consistent format over several hours, experiments performed over this time frame would benefit from being kept at 37°C and 5% CO_2. This would require additional robotics to remove the plate lid (which prevents media evaporation at 37°C), but which is not present within the IN Cell Analyzer. Lastly, higher image acquisition rates may be able to resolve differences between experimental groups that are more subtle, enabling peak counting rather than area to be used as a metric. Here, we were limited by a 9 Hz acquisition rate, which

is not able to resolve single action potentials, even though GCaMP6f kinetics enable their resolution.

Overall, we have demonstrated the formation and use of a high-throughput circuit screening model. We have shown that distinct neuronal pairs can form a functional circuit, and that the circuit can be manipulated according to defined and established approaches.

Conclusion

Using microfluidics and induced neuronal technology, we have created a high-throughput screening platform for neuronal circuit studies using human induced neurons. iNs form functional circuits which can be probed by small molecules, and the system can be analyzed either by calcium imaging or fluorescent staining in the IN Cell Analyzer 6000. Here, we provided proof-of-concept for further development circuit based models, with a goal of creating a high-throughput screening platform to aid in pharmaceutical drug development. We hope that this platform can serve as a tool for therapeutic development, and ultimately assist in finding lasting treatments for neuropsychiatric disorders.

CHAPTER 6: CONCLUSIONS AND FUTURE WORK

Building on previous approaches using compartmentalized systems, we have demonstrated the utility of microfluidics for generating neural circuit models. We incorporated neurons from patient-derived stem cell lines to form circuit models of known genetic background. While we did not directly investigate the role of genetic mutations contained in some iPSC lines, we did provide a proof-of-concept for stem cells forming such circuits. This expands previous work that has focused primarily on neurons from mouse hippocampus or other primary cultures. These studies, within the context of microfluidic circuit models, provide the basis for this continuing work. Here, we have demonstrated the successful fabrication of compartmentalized devices and their use for neuronal studies. In addition to the novelty of using different subtypes of human induced neurons, we developed a circular model which contains a large open central chamber. This central chamber is open to patch clamp apparatus, making the device susceptible to rigorous and informative functional studies. This is particularly important when network changes are subtle, involving plastic changes at synaptic terminals, as in drug addiction.[22, 23, 96] These alterations to neural circuits may be investigated through the measurement of AMPA/NMDA receptor ratio, which is indicative plastic changes involved in learning. We also demonstrated the ability of optogenetics to stimulate neural activity within a circuit context. This is a powerful tool which can be used to provide initial stimulus within the network. Importantly also, we showed that the device is capable of establishing a three-way circuit, enabling more complex circuit-based studies. While we did not show the capacity of our model for specific chamber chemi-

cal treatments, this has been demonstrated previously[83], provided that the hydrostatic head from one chamber counters the diffusion from the other.

We also expanded this circuit system into a high-throughput model built within a 96 well plate. Due to size constraints, we reduced the number of chambers to two, which still allows two distinct neuronal populations to be investigated. Excitatory and inhibitory neurons were chosen as those were the easier of the three (along with dopaminergic) neurons to produce and since the excitatory to inhibitory circuit interaction is common in many brain regions (e.g., VTA-NAc). Shifting the functional readout to calcium imaging, we were once again able to demonstrate that across the microchannels, neurons can generate spontaneous activity, and that this activity can be altered either in the presence of either receptor antagonists or chemogenetic stimulation. Modulation of the circuit in a defined manner enables the researcher to dissect precise neuronal communication patterns and to measure the adaptation of the network over time. Here, we were able to silence out-going excitatory transmission to the inhibitory neuronal chamber with the addition of CNQX. Also, the addition of CNO or Clozapine to a hM3D-infected culture produced network activity above basal levels. While we desired to demonstrate our setup as a drug screening platform, we were limited by the capacity of the liquid handling apparatus of the IN Cell Analyzer 6000, as well as the image acquisition parameters to discern subtle network activity. Nevertheless, inter-chamber network activity was still established and probed in a defined manner. Regarding the ability to perform morphological assays, we also demonstrated the ability of the device to culture different neuronal populations for disease-related studies. Mutations affect-

ing the function neuroligin-3 have been implicated in autism spectrum disorders[18, 19, 108], and we sought to use the device as a means of screening synapse number in a neuroligin-3 over-expression assay. The assay did not produce a significant difference between conditions, but we did demonstrate that individual populations were cultured in their respective chambers, along with a "same-well" control, which can serve to normalize synaptic numbers within wells.

As regards chemically-distinct chambers, inability to provide distinct chemical treatments to a well remains a caveat of the 96 well plate setup. The circular device has the advantage of extending PDMS wall heights to provide barrier for increased liquid levels. The 96 well plate is limited by the skirt height of the plate to which it is fixed, and cannot be extended beyond that height without impacting the IN Cell Analyzer's plate handling and recognition. One option for overcoming this drawback is to redesign the device to include an extended wall that protrudes up through the microwell (Figure 6.1). This extended wall would provide additional height barrier between cellular compartments, and may enable a chemical barrier between compartments through the use of hydrostatic pressure differences. Alternatively, a 3D printed device can be used, as long as we can achieve resolution low enough for the 3 μm-high microchannels. A combination device of a 3D printed template and microfabricated device may serve as the ideal platform for future studies, provided that it is compatible with the IN Cell Analyzer or other apparatus.

Taken together, these two devices offer useful, and yet different information for the study of psychiatric disorders with respect to neural circuits. On the one hand, high-rigor studies can be performed on human induced neurons in a three-

way circuit using patch clamp electrophysiology. On the other hand, network activity can be screened in a high-throughput manner for more pronounced circuit-level effects detectable by calcium imaging.

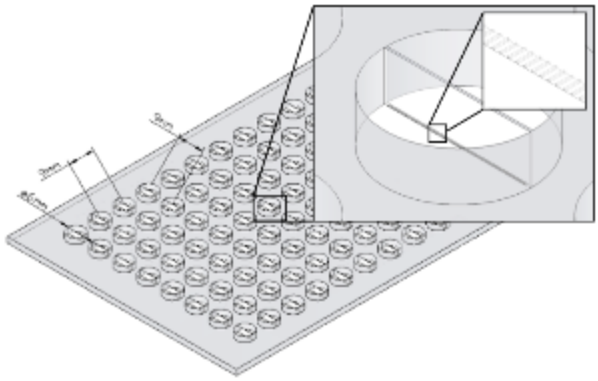

Figure 6.1. Extended central wall microdevice. A CAD drawing showing the extended central wall. This would make chemically-distinct compartments feasible by allowing the experimenter to build a hydrostatic head on one side to oppose diffusion from the other.

With regard to these high-throughput morphological studies, it is important to have useful computational tools enabling the processing of large amounts of data in a timely manner. We therefore developed *Intellicount*, a MATLAB-based GUI designed to perform synapse analysis. Our program can handle large datasets and provide meaningful information on full image sizes with relative speed. This, and other computational tools, are required for the analysis of large data sets as those collected for the 96 well plate neural circuit model.

As we further our study of neuropsychiatric diseases, with the goal of providing improved modeling systems for drug development, it is imperative to use human model cells, given the important link between genetics and disease onset.[27-29, 122, 147] As mentioned previously, a single nucleotide polymorphism (SNP) in the post-synaptic neuroligin-3 gene (R451C) has been implicated in autism.[108, 109] With

regard to substance abuse, a variety of genes have been suggested to play a role in mediating disease.[148] Specifically, a SNP in the alpha 5 subunit of the nicotinic acetylcholine receptor (CHRNA5) has been identified as a mutation that mediates addiction risk with respect to nicotine.[149, 150] The mu-opioid receptor (MOR) also possesses a SNP mediating addiction risk. The OPRM1 mutation, which converts an asparagine to an aspartic acid (N40D) has been implicated having a role in opioid addiction as well as nicotine and alcohol. The precise role and degree of risk provided by these mutations is the subject of further mechanistic study and likely has subject variability. At this point, it is important to understand how these SNPs alter normal physiological activity and how they impact the reward circuit as a whole. Certainly, there is much more information to be gained through these studies at both the single and neural circuit levels. Human induced neurons serves as a point of departure for these studies, as patient specific lines, that is, cell lines with and without the point mutation, can be obtained and maintained for *in vitro* studies. We propose our circuit models to assist in the investigation and identification of network-based changes. In some cases, network activity may be significantly altered and therefore visible by calcium imaging. In other cases, alterations may only be detected by more sensitive methods such as electrophysiology. Due to the inherent biological variation between cell lines, and the perhaps the additional variation present in human induced neurons as a result of the infection protocol, it is important that any research using this approach accommodate a wide range of distinct cell lines to establish normal or "wild type" conditions. In such cases, where multiple cell lines are being analyzed in replicate, high-throughput methods may be more

suitable. Our 96 well plate design may accommodate these studies, providing both morphological and functional readouts in a two-way circuit model. There is however a trade-off to be mentioned: if multiple conditions/cell lines need to be run to accommodate intrinsic cell line variability, the cellular readout may be too subtle or obfuscated by biological variation to be seen within any high-throughput platform. In such cases, this highlights the need for improved instrumentation to facilitate more sensitive measurements and improved experimental design to enable the acquisition and processing of such data. The research presented here demonstrated the utility of a high-throughput system to discern network level effects, but was limited by both camera acquisition rates and liquid handling robotics. More rigorous liquid handling systems are available as well as high speed cameras capable of capturing single action potential events. The combination of these technologies in our 96 well plate may provide additional functional information on a par with electrophysiology while maintaining its high-throughput methodology.

Regarding liquid handling, the IN Cell Analyzer 6000 offered useful but limited operations. The system requires that the lid of the culture plate be removed for all experiments. This is a limitation since the experiment must be run at room temperature to mitigate evaporation over several hours of image collection. If the lid could be removed and placed back on after chemical treatment, the experiment could be run at 37°C, enabling the cultures to be more stable over time. Furthermore, a full set of 96 wells could be processed if the system could be kept at standard culture conditions. The IN Cell Analyzer 6000 is also limited in the number of reagents that can be transferred into the culture plate within a single run. The user

can either transfer a reagent from the reagent plate (in a well-to-well format only, e.g., A1➔A1) or the reagent bottle. The user is not allowed to transfer two distinct reagents into a single well in one experimental run. In order to capture the effect of a treatment and addition of KCl for neuronal identification, two separate experimental runs must be performed and concatenated to get the full image set. With more processing and liquid handling options, these experiments would be able to be greatly extended and extrapolated to the full number of wells. Ideally, acquisition rates greater than 30 Hz in a well plate maintained at 37°C in 5% CO_2 would increase sensitivity for detecting minor group differences while reducing culture variability between microwells.

Recommendations for improved device microfabrication

I have already mentioned above one design recommendation for the 96 well plate, which could enable chemical distinction between chambers. Regarding device production and design, two additional elements of the device can be altered to improve experimental processing. First, the plate bottom is not perfectly flat and consistent across the plate. This requires the user to make manual focus adjustments between each run. The IN Cell Analyzer has the capacity to perform experiments on subsequent runs in a single well with an autofocus option, but the plate variation is too high for this feature. Therefore, the user must be present to re-focus the new well after each experimental run (as well as exchange reagent plates). The need to re-focus can be reduced with more consistent and streamlined PDMS casting techniques. One approach would be to spin PDMS onto the wafer, which provides a consistent PDMS thickness across all wells and between devices. The

thickness must, however, be large enough to hold enough media during cell plating, and must cover all photoresist features. Currently, the highest photoresist layer is approximately 320 μm, but this layer could be reduced if PDMS spin-coating is desirable but not able to overcome this thicker SU-8 layer. Alternatively, a casting mold could be designed which holds a wafer in place in a defined orientation and which provides a consistent PDMS thickness. For manufacturing these devices in a commercialized setting, injection molding would be the ideal platform, provided it can achieve the necessary resolution for 3 μm deep recessed microchannels.

Second, regarding the formation of defined neural circuits, further culture restrictions facilitated by device design and setup could aid in data interpretation. We have demonstrated successful compartmentalization of distinct neuronal subtypes. The circuit established between the two populations is defined by the ability of outgrowing axonal projections to traverse the microchannels and synapse with neurons on the opposing side. There are, however, differences between the maturation and projection distance of different subtypes. Excitatory neurons mature quicker and produce axons and dendrites earlier in the differentiation protocol than do inhibitory neurons. This makes excitatory neurons more likely to fill microchannels over against inhibitory neurons in the same well. But these features of the differentiation process makes the circuit somewhat undefined. For example, it is difficult to know how many inputs a single neuron is receiving from its own side and the other side of the device. This becomes more convoluted when both excitatory neurons and inhibitory neurons are cultured against each other. One cannot know whether a cell is more likely to receive glutamate or GABA in response to a

network burst. Two strategies may reduce the complexity of the system. As mentioned above in Chapter 1, there are microfabrication approaches to building in directionality into these systems. Directionality reduces the complexity of the system by providing a single "emitting" side and a single "receiving" side. With these approaches, the experimenter can be confident that projections from the "receiving" side are not biasing the output from the "emitting" side. This would aid in reducing the complexity of the system, although it may be subject still to unknown synaptic formation on the "receiving" side. It is near impossible to know for certainty how many synapses a receiving neuron has formed from an emitting neuron compared to neighboring receiving neurons. A second strategy to this point to reduce complexity is to optimize (and likely reduce) the number of neurons seeded in a given chamber. This setup would provide a more straightforward visualization of axonal projections and their targets. This comes at the cost however of not being able to generate a strong enough circuit effect (either by DREADDs or other means) to transmit to the other chamber. I.e., the benefit of dense cultures is dense axonal bundles traversing the microchannels to provide a robust net signal to the opposing chamber. These parameters must be optimized for future experiments to aid in interpretation of data.

Modeling the mesolimbic dopamine pathway for drug addiction studies

I have previously mentioned that the five-chambered, circular device was originally designed to model the mesolimbic dopamine pathway which is affected by drugs of abuse. We have been able to generate excitatory, inhibitory, and dopaminergic neurons which serve as the primary subtypes found in this circuit. The

central chamber of the device is the chamber from which neurons can be recorded, and therefore is the chamber of interest. Building in directionality from the side chambers to the central chamber would reproduce a scenario where a brain nucleus, e.g. the Nucleus Accumbens (NAc), receives inputs from two different neuronal populations. With directionality focused toward the central chamber, we can isolate the effects of excitatory and dopaminergic neurons projecting to the central chamber inhibitory neurons. To create more locations for a three-way circuit interaction, 8 side chambers instead of 4 should be used (Figure 6.2). This would result in more locations for three-way circuit formations. This is particularly important

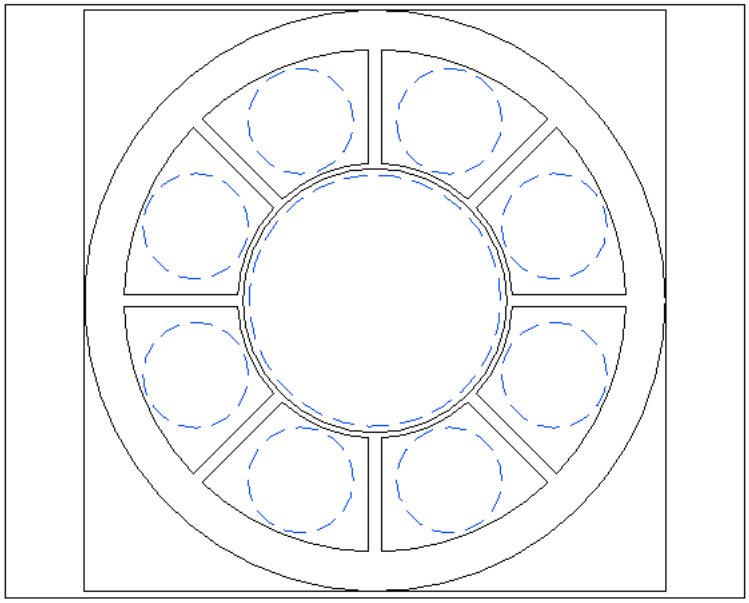

Figure 6.2. Altered microdevice to contain eight side chambers. Black lines indicate PDMS walls between compartments or coverslip location. Blue lines show hollow punch locations. Eight chambers allow for the formation of a greater number of 3-way circuits in the central chamber.

for electrophysiology studies, since it is ideal to create as many opportunities for patching cells receiving inputs from both side chambers. Furthermore, as mentioned above in Chapter 3, the PDMS may be poured sufficiently high to take ad-

vantage of convective forces to counter small molecule diffusion. This would enable chemical distinction between the side chambers and central chamber and therefore the ability to screen small molecules against the circuit. With chemical distinction and directionality built in, the circuit now has a very narrowly defined and highly controllable set of parameters for experimentation, leaving only intrinsic biological variability.

When considering the role of genetics in mediating addiction risk, CHRNA5 is known to contain a single nucleotide polymorphism, D398N, which affects reward circuit function, through a decrease of the aversive effects of drugs of abuse.[28, 29, 122, 149, 150] This polymorphism exists within the alpha 5 subunit of the nicotinic acetylcholine receptor (nAChR), which finds its placement in the prefrontal cortex.[151, 152] As part of the reward pathway, aberrant function in the prefrontal cortex may affect decision making and reward evaluation. Circuit-based endophenotypes can be investigated in the circular microdevice described above, which may shed light into the role of CHRNA5 D398N and its downstream effects on the synaptic targets of excitatory neurons. The prefrontal cortex is primarily populated by excitatory neurons. These neurons can be seeded in alternating side chambers, along with dopaminergic neurons to investigate the role of modulation of the excitatory to inhibitory circuit (analogous to the ventral tegmental area and its input to the nucleus accumbens). The central chamber would be seeded with inhibitory neurons. Side-chamber excitatory neurons would be either from a control cell line, or possessing the D398N SNP. Nicotine, which binds nAChR, can be added to side chambers, and recordings or calcium imaging studies can be performed to investi-

gate the impact of D398N on excitatory neuronal response, as measured by downstream inhibitory neurons in the central chamber.

The role of synaptic plasticity in addiction is also important, as this generally renders the addict less likely avoid drug seeking behaviors. This altered "learning" through substance abuse can be seen through electrophysiology as a measure of the AMPA/NMDA receptor ratio.[23, 153, 154] During long term potentiation, AMPA receptors get inserted into the post-synaptic membrane, increasing the AMPAR/NMDA receptor ratio. Capturing this shift could open the door to serving as a meaningful therapeutic target for those suffering with drug addiction. For example, therapies could be screened which protect or reverse the AMPA/NMDA receptor ratio in response to nicotine. Also, the role of modulatory DA-ergic neurons can be investigated in this system. More or less dopaminergic tone in the central chamber (via stimulation of DA-ergic neurons with glutamate or optogenetically) could provide additional information into the function of the reward pathway. While this experimental proposal has focused on inhibitory neurons as the output or target, this scenario may be shifted to include DA-ergic neurons in the central chamber, or a combination of subtypes. The important factor is that the device be designed in such as a way as to mitigate additional influences, either from inter-chamber diffusion, or binary circuits with no directionality. These elements (lack of directionality and inter-chamber diffusion) may have their advantages in some cases, but it is in the best interest of the researcher to keep the system as simple as possible, until the circuit is better understood and performs in a predictable way.

Screening the response to opioids: high-throughput studies on the reward pathway

In recent years, opioid abuse and related deaths have been on the rise. Often, what begins as prescription pain treatments turns into substance abuse. There is therefore a great need to further our understanding of the role of opioids and investigate measures of preventing or reducing opioid abuse. Opioids are molecularly similar to endogenous signaling molecules such as endorphins or enkephalins, and they compete for the same receptor, most notably, the mu-opioid receptor (MOR). The mu-opioid receptor exists in many different parts of the central nervous system, but with respect to substance abuse, it is found in inhibitory neurons within the VTA.[155] The current hypothesis of action is that opioid binding to MOR causes a decrease in inhibitory neuron activity[vi] and therefore disinhibits VTA DA-ergic signaling to the nucleus accumbens.

To perform a high-throughput screen of this circuit, dopaminergic neurons can be seeded in one compartment and inhibitory neurons in the other. Again, directionality will be important here so as to reduce unnecessary systemic variation. In such a system, different types of opioids, e.g, morphine or DAMGO, can be used to investigate the cellular response and robustness of response in different cell lines. Additionally, there is a single nucleotide polymorphism that has identified as a risk factor for addiction: A118G in OPRM1 which is analogous to N40D in the mu-opioid receptor.[27] If the impact of this SNP is of interest, iPSC lines with and without the SNP can be cultured with DA-ergic neurons. Then, an equal concentration

[vi] Stimulation of the mu-opioid receptor results in a decrease in activity since the receptor is a G_i-coupled protein receptor.

of opioid can be applied to each cellular condition to examine the effects. An alternative approach would be to mix the DA-ergic and inhibitory neurons in the same compartment. This would form a circuit similar to the VTA ➔ NAc projections, where the mixed culture (as in the VTA) could project to a single population of inhibitory neurons in the other chamber (as in the NAc). The net signal then, would be influenced by inhibitory neurons altering DA-ergic neuronal firing into the other chamber. If differences are seen between SNP and control, pharmacological interventions can then be used with a goal of "rescuing" the altered functionality. One drawback to this approach however is that it is difficult to know the impact of any percentage of inhibitory neurons co-cultured with DA-ergic neurons. This system setup would likely need to be optimized.

Concluding remarks

Compartmentalized systems offer promising platforms for therapeutic development. The combination of these systems with human stem cells overcomes many of the limitations of primary cultures with respect to disease modeling. It is important however to carefully design the experimental system to reduce variability. This can be done through careful device production, circuit directionality approaches, and consistent stem cell differentiation. As the field evolves, stem cell production will likely become more streamlined, enabling greater consistency between infections. There is still a great deal of work to be done to bridge the gap between single cell models of disease and animal models, but the work presented above demonstrates two novel devices as a proof-of-concept for using human stem cells as circuit models. As the work continues, we hope that one day the stigma of

suffering from neuropsychiatric diseases will be gone, and treatments will be available to all who need them. Until then, we continue to press forward toward the goal of growing in scientific understanding of these diseases and creating model systems that will aid in therapeutic development.

REFERENCES

1. Renault, R. et al. Combining microfluidics, optogenetics and calcium imaging to study neuronal communication in vitro. *PLoS One* **10**, e0120680 (2015).
2. Fantuzzo, J.A. et al. μNeurocircuitry: Establishing in vitro models of neurocircuits with human neurons. *Technology* **5**, 87-97 (2017).
3. Pang, Z.P., Cao, P., Xu, W. & Sudhof, T.C. Calmodulin controls synaptic strength via presynaptic activation of calmodulin kinase II. *J Neurosci* **30**, 4132-4142 (2010).
4. Trautmann, S., Rehm, J. & Wittchen, H.U. The economic costs of mental disorders: Do our societies react appropriately to the burden of mental disorders? *EMBO Rep* **17**, 1245-1249 (2016).
5. Akil, H. et al. The Future of Psychiatric Research: Genomes and Neural Circuits. *Science Medicine* **327**, 1580-1581 (2010).
6. Pankevich, D.E., Altevogt, B.M., Dunlop, J., Gage, F.H. & Hyman, S.E. Improving and accelerating drug development for nervous system disorders. *Neuron* **84**, 546-553 (2014).
7. Coughlin, S.S. Anxiety and Depression: Linkages with Viral Diseases. *Public Health Reviews* **34**, 92-104 (2012).
8. Gratten, J., Wray, N.R., Keller, M.C. & Visscher, P.M. Large-scale genomics unveils the genetic architecture of psychiatric disorders. *Nat Neurosci* **17**, 782-790 (2014).
9. Nestler, E.J. & Hyman, S.E. Animal models of neuropsychiatric disorders. *Nat Neurosci* **13**, 1161-1169 (2010).
10. Yuste, R. From the neuron doctrine to neural networks. *Nat Rev Neurosci* **16**, 487-497 (2015).
11. Haber, S.N. & Rauch, S.L. Neurocircuitry: a window into the networks underlying neuropsychiatric disease. *Neuropsychopharmacology* **35**, 1-3 (2010).
12. Insel, T.R. Disruptive insights in psychiatry: transforming a clinical discipline. *J Clin Invest* **119**, 700-705 (2009).
13. Insel, T.R. & Wang, P.S. Rethinking Mental Illness. *JAMA* **303**, 1970-1971 (2010).
14. Hyman, S. Mental Illness: Genetically Complex Disorders of Neural Circuitry and Neural Communication. *Neuron* **28**, 321-323 (2000).
15. Bailey, A. et al. Autism as a strongly genetic disorder: evidence from a British twin study. *Psychological Medicine* **25**, 63 (2009).
16. Sullivan, P.F., Kendler, K.S. & Neale, M.C. Schizophrenia as a Complex Trait. *Arch Gen Psychiatry* **60**, 1187-1192 (2003).
17. Keller, M.A. et al. Whole genome association studies of neuropsychiatric disease: An emerging era of collaborative genetic discovery. *Neuropsychiatric Disease and Treatment* **3**, 613-618 (2007).
18. Etherton, M. et al. Autism-linked neuroligin-3 R451C mutation differentially alters hippocampal and cortical synaptic function. *PNAS* **108**, 13764-13769 (2011).
19. Tabuchi, K. et al. A neuroligin-3 mutation implicated in autism increases inhibitory synaptic transmission in mice. *Science* **318**, 71-76 (2007).
20. Aston-Jones, G. & Deisseroth, K. Recent advances in optogenetics and pharmacogenetics. *Brain Research* **1511**, 1-5 (2013).
21. Tye, K.M. & Deisseroth, K. Optogenetic investigation of neural circuits underlying brain disease in animal models. *Nat Rev Neurosci* **13**, 251-266 (2012).
22. Kalivas, P.W. & O'Brien, C. Drug addiction as a pathology of staged neuroplasticity. *Neuropsychopharmacology* **33**, 166-180 (2008).

23. Kauer, J.A. & Malenka, R.C. Synaptic plasticity and addiction. *Nat Rev Neurosci* **8**, 844-858 (2007).
24. Kim, C.K., Adhikari, A. & Deisseroth, K. Integration of optogenetics with complementary methodologies in systems neuroscience. *Nat Rev Neurosci* **18**, 222-235 (2017).
25. Nestler, E.J. in Targeting Gene Regulator in Brain Reward Circuit Eyed as Treatment. (ed. J. Asher) (NIMH Press Office, https://www.nimh.nih.gov/news/science-news/2010/resilience-factor-low-in-depression-protects-mice-from-stress.shtml; 2010).
26. Koob, G.F. & Volkow, N.D. Neurocircuitry of addiction. *Neuropsychopharmacology* **35**, 217-238 (2010).
27. Lee, M.R. et al. Functional polymorphism of the mu-opioid receptor gene (OPRM1) influences reinforcement learning in humans. *PLoS One* **6**, e24203 (2011).
28. Tammimaki, A. et al. Impact of human D398N single nucleotide polymorphism on intracellular calcium response mediated by alpha3beta4alpha5 nicotinic acetylcholine receptors. *Neuropharmacology* **63**, 1002-1011 (2012).
29. Oni, E.N. et al. Increased nicotine response in iPSC-derived human neurons carrying the CHRNA5 N398 allele. *Sci Rep* **6**, 34341 (2016).
30. Robbins, T.W. & Everitt, B.J. Drug addiction: bad habits add up. *Nature* **398**, 567-570 (1999).
31. Lynch, W.J., Nicholson, K.L., Dance, M.E., Morgan, R.W. & Foley, P.L. Animal Models of Substance Abuse and Addiction: Implications for Science, Animal Welfare, and Society. *Comparative Medicine* **60**, 177-188 (2010).
32. Callaway, E. Alzheimer's drugs take a new tack. *Nature* **489**, 13-14 (2012).
33. Hyman, S.E. Back to basics: luring industry back into neuroscience. *Nature Neuroscience* **19**, 1383-1384 (2016).
34. Kesselheim, A.S., Hwang, T.J. & Franklin, J.M. Two decades of new drug development for central nervous system disorders. *Nat Rev Drug Discov* **14**, 815-816 (2015).
35. Carter, M. & Shieh, J. Guide to Research Techniques in Neuroscience. (Elsevier, 2010).
36. Takahashi, K. et al. Induction of pluripotent stem cells from adult human fibroblasts by defined factors. *Cell* **131**, 861-872 (2007).
37. Takahashi, K. & Yamanaka, S. Induction of pluripotent stem cells from mouse embryonic and adult fibroblast cultures by defined factors. *Cell* **126**, 663-676 (2006).
38. Wen, Z., Christian, K.M., Song, H. & Ming, G.L. Modeling psychiatric disorders with patient-derived iPSCs. *Curr Opin Neurobiol* **36**, 118-127 (2016).
39. Avior, Y., Sagi, I. & Benvenisty, N. Pluripotent stem cells in disease modelling and drug discovery. *Nat Rev Mol Cell Biol* **17**, 170-182 (2016).
40. Brennand, K.J. & Gage, F.H. Modeling psychiatric disorders through reprogramming. *Dis Model Mech* **5**, 26-32 (2012).
41. Haggarty, S.J. & Perlis, R.H. Translation: screening for novel therapeutics with disease-relevant cell types derived from human stem cell models. *Biol Psychiatry* **75**, 952-960 (2014).
42. Haggarty, S.J., Silva, M.C., Cross, A., Brandon, N.J. & Perlis, R.H. Advancing drug discovery for neuropsychiatric disorders using patient-specific stem cell models. *Mol Cell Neurosci* **73**, 104-115 (2016).

43. Panchision, D.M. Concise Review: Progress and Challenges in Using Human Stem Cells for Biological and Therapeutics Discovery: Neuropsychiatric Disorders. *Stem Cells* **34**, 523-536 (2016).
44. Li, L., Chao, J. & Shi, Y. Modeling neurological diseases using iPSC-derived neural cells : iPSC modeling of neurological diseases. *Cell Tissue Res* (2017).
45. Pang, Z.P. et al. Induction of human neuronal cells by defined transcription factors. *Nature* **476**, 220-223 (2011).
46. Yang, N. et al. Generation of pure GABAergic neurons by transcription factor programming. *Nat Methods* **14**, 621-628 (2017).
47. Zhang, Y. et al. Rapid single-step induction of functional neurons from human pluripotent stem cells. *Neuron* **78**, 785-798 (2013).
48. Lorenz, C. et al. Human iPSC-Derived Neural Progenitors Are an Effective Drug Discovery Model for Neurological mtDNA Disorders. *Cell Stem Cell* **20**, 659-674 e659 (2017).
49. Han, S.S., Williams, L.A. & Eggan, K.C. Constructing and deconstructing stem cell models of neurological disease. *Neuron* **70**, 626-644 (2011).
50. Boyden, E.S. A history of optogenetics: the development of tools for controlling brain circuits with light. *F1000 Biol Rep* **3**, 11 (2011).
51. Boyden, E.S., Zhang, F., Bamberg, E., Nagel, G. & Deisseroth, K. Millisecond-timescale, genetically targeted optical control of neural activity. *Nat Neurosci* **8**, 1263-1268 (2005).
52. Deisseroth, K. Optogenetics. *Nat Methods* **8**, 26-29 (2011).
53. Pastrana, E. Optogenetics: Controlling cell function with light. *Nature Methods* **8**, 24-25 (2011).
54. Bernstein, J.G. & Boyden, E.S. Optogenetic tools for analyzing the neural circuits of behavior. *Trends Cogn Sci* **15**, 592-600 (2011).
55. Lee, H.-M., Giguere, P.M. & Roth, B.L. DREADDs: novel tools for drug discovery and development. *Drug Discovery Today* **19**, 469-473 (2014).
56. Koehler, S. et al. Single and Transient Ca2+ Peaks in Podocytes do not induce Changes in Glomerular Filtration and Perfusion. *Sci Rep* **6**, 35400 (2016).
57. Cai, D.J. et al. A shared neural ensemble links distinct contextual memories encoded close in time. *Nature* **534**, 115-118 (2016).
58. Ferguson, S.M. & Neumaier, J.F. Grateful DREADDs: engineered receptors reveal how neural circuits regulate behavior. *Neuropsychopharmacology* **37**, 296-297 (2012).
59. Smith, K.S., Bucci, D.J., Luikart, B.W. & Mahler, S.V. DREADDS: Use and application in behavioral neuroscience. *Behav Neurosci* **130**, 137-155 (2016).
60. Gomez, J. et al. Chemogenetics revealed: DREADD occupancy and activation via converted clozapine. *Science* **357**, 503-507 (2017).
61. Meltzer, H.Y. Commentary on "clinical studies on the mechanism of action of clozapine; the dopamine-serotonin hypothesis of schizophrenia." Psychopharmacology (1989) 99:S18-S27. *Psychopharmacology (Berl)* **163**, 1-3 (2002).
62. Dimidschstein, J. et al. A viral strategy for targeting and manipulating interneurons across vertebrate species. *Nat Neurosci* **19**, 1743-1749 (2016).
63. Ji, B. et al. Multimodal Imaging for DREADD-Expressing Neurons in Living Brain and Their Application to Implantation of iPSC-Derived Neural Progenitors. *J Neurosci* **36**, 11544-11558 (2016).

64. Xie, C. & Cui, Y. Nanowire platform for mapping neural circuits. *Proc Natl Acad Sci U S A* **107**, 4489-4490 (2010).
65. Kim, R., Joo, S., Jung, H., Hong, N. & Nam, Y. Recent trends in microelectrode array technology for in vitro neural interface platform. *Biomedical Engineering Letters* **4**, 129-141 (2014).
66. Gullo, F. et al. Multi-electrode array study of neuronal cultures expressing nicotinic beta2-V287L subunits, linked to autosomal dominant nocturnal frontal lobe epilepsy. An in vitro model of spontaneous epilepsy. *Front Neural Circuits* **8**, 87 (2014).
67. Langhammer, C.G., Kutzing, M.K., Luo, V., Zahn, J.D. & Firestein, B.L. A topographically modified substrate-embedded MEA for directed myotube formation at electrode contact sites. *Ann Biomed Eng* **41**, 408-420 (2013).
68. Obien, M.E., Deligkaris, K., Bullmann, T., Bakkum, D.J. & Frey, U. Revealing neuronal function through microelectrode array recordings. *Front Neurosci* **8**, 423 (2014).
69. Wagenaar, D.A., Pine, J. & Potter, S.M. An extremely rich repertoire of bursting patterns during the development of cortical cultures. *BMC Neurosci* **7**, 11 (2006).
70. Quirin, S. et al. Calcium imaging of neural circuits with extended depth-of-field light-sheet microscopy. *Optics Letters* **41**, 855-858 (2016).
71. Yang, W. et al. Simultaneous Multi-plane Imaging of Neural Circuits. *Neuron* **89**, 269-284 (2016).
72. Grienberger, C. & Konnerth, A. Imaging calcium in neurons. *Neuron* **73**, 862-885 (2012).
73. Kwan, A.C. What can population calcium imaging tell us about neural circuits? *J Neurophysiol* **100**, 2977-2980 (2008).
74. Podor, B. et al. Comparison of genetically encoded calcium indicators for monitoring action potentials in mammalian brain by two-photon excitation fluorescence microscopy. *Neurophotonics* **2**, 021014 (2015).
75. Jang, M.J. & Nam, Y. NeuroCa: integrated framework for systematic analysis of spatiotemporal neuronal activity patterns from large-scale optical recording data. *Neurophotonics* **2**, 035003 (2015).
76. Patel, T.P., Man, K., Firestein, B.L. & Meaney, D.F. Automated quantification of neuronal networks and single-cell calcium dynamics using calcium imaging. *J Neurosci Methods* **243**, 26-38 (2015).
77. Artimovich, E., Jackson, R.K., Kilander, M.B.C., Lin, Y.C. & Nestor, M.W. PeakCaller: an automated graphical interface for the quantification of intracellular calcium obtained by high-content screening. *BMC Neurosci* **18**, 72 (2017).
78. Campenot, R.B. Local control of neurite development by nerve growth factor. *Proc Natl Acad Sci U S A* **74**, 4516-4519 (1977).
79. Campenot, R.B. & MacInnis, B.L. Retrograde transport of neurotrophins: fact and function. *J Neurobiol* **58**, 217-229 (2004).
80. Campenot, R.B. & Martin, G. Construction and Use of Compartmented Cultures for Studies of Cell Biology of Neurons. **3rd Ed**, 49-57 (2001).
81. Vikman, K.S., Backström, E., Kristensson, K. & Hill, R.H. A two-compartment in vitro model for studies of modulation of nociceptive transmission. *Journal of Neuroscience Methods* **105**, 175-184 (2001).
82. Park, J.W., Vahidi, B., Taylor, A.M., Rhee, S.W. & Jeon, N.L. Microfluidic culture platform for neuroscience research. *Nat Protoc* **1**, 2128-2136 (2006).

83. Taylor, A.M. et al. Microfluidic Multicompartment Device for Neuroscience Research. *Langmuir* **19**, 1551-1556 (2003).
84. Coquinco, A. et al. A microfluidic based in vitro model of synaptic competition. *Mol Cell Neurosci* **60**, 43-52 (2014).
85. Dolle, J.P., Morrison, B., 3rd, Schloss, R.S. & Yarmush, M.L. An organotypic uniaxial strain model using microfluidics. *Lab Chip* **13**, 432-442 (2013).
86. Karimi, M. et al. Microfluidic systems for stem cell-based neural tissue engineering. *Lab Chip* **16**, 2551-2571 (2016).
87. Shi, P., Nedelec, S., Wichterle, H. & Kam, L.C. Combined microfluidics/protein patterning platform for pharmacological interrogation of axon pathfinding. *Lab Chip* **10**, 1005-1010 (2010).
88. Peyrin, J.M. et al. Axon diodes for the reconstruction of oriented neuronal networks in microfluidic chambers. *Lab Chip* **11**, 3663-3673 (2011).
89. Hasan, M. & Berdichevsky, Y. Neural Circuits on a Chip. *Micromachines* **7**, 157 (2016).
90. Chang, J.C., Brewer, G.J. & Wheeler, B.C. Modulation of neural network activity by patterning. *Biosens Bioelectron* **16**, 527-533 (2001).
91. Marconi, E. et al. Emergent functional properties of neuronal networks with controlled topology. *PLoS One* **7**, e34648 (2012).
92. Lauer, L., Vogt, A., Yeung, C.K., Knoll, W. & Offenhäusser, A. Electrophysiological recordings of patterned rat brain stem slice neurons. *Biomaterials* **23**, 3123-3130 (2002).
93. Pan, L. et al. An in vitro method to manipulate the direction and functional strength between neural populations. *Front Neural Circuits* **9**, 32 (2015).
94. Renault, R., Durand, J.B., Viovy, J.L. & Villard, C. Asymmetric axonal edge guidance: a new paradigm for building oriented neuronal networks. *Lab Chip* **16**, 2188-2191 (2016).
95. le Feber, J., Postma, W., de Weerd, E., Weusthof, M. & Rutten, W.L. Barbed channels enhance unidirectional connectivity between neuronal networks cultured on multi electrode arrays. *Front Neurosci* **9**, 412 (2015).
96. Gerdeman, G.L., Partridge, J.G., Lupica, C.R. & Lovinger, D.M. It could be habit forming: drugs of abuse and striatal synaptic plasticity. *Trends in Neurosciences* **26**, 184-192 (2003).
97. Robison, A.J. & Nestler, E.J. Transcriptional and epigenetic mechanisms of addiction. *Nat Rev Neurosci* **12**, 623-637 (2011).
98. Xia, Y. & Whitesides, G.M. Soft Lithography. *Annual Review Material Science* **28**, 153-184 (1998).
99. Qin, D., Xia, Y. & Whitesides, G.M. Soft lithography for micro- and nanoscale patterning. *Nat Protoc* **5**, 491-502 (2010).
100. Microchem SU-8 2000 Datasheet 2000.5-2015. 1-5 (2017).
101. Aran, K. et al. Microfiltration platform for continuous blood plasma protein extraction from whole blood during cardiac surgery. *Lab Chip* **11**, 2858-2868 (2011).
102. Marro, S. et al. Direct lineage conversion of terminally differentiated hepatocytes to functional neurons. *Cell Stem Cell* **9**, 374-382 (2011).
103. Vierbuchen, T. et al. Direct conversion of fibroblasts to functional neurons by defined factors. *Nature* **463**, 1035-1041 (2010).
104. Tiscornia, G., Singer, O. & Verma, I.M. Production and purification of lentiviral vectors. *Nat Protoc* **1**, 241-245 (2006).

105. Moore, J.C., Sheldon, M.H. & Hart, R.P. Biobanking in the era of the stem cell: a technical and operational guide: The Use of iPSC to Study Genetic Diseases in Mental Health Disorders. (Morgan-Claypool Publishers, 2012).
106. Davies, S.P., Reddy, H., Caivano, M. & Cohen, P. Specificity and mechanism of action of some commonly used protein kinase inhibitors. *Biochemical Journal* **351**, 95-105 (2000).
107. Chih, B., Afridi, S.K., Clark, L. & Scheiffele, P. Disorder-associated mutations lead to functional inactivation of neuroligins. *Hum Mol Genet* **13**, 1471-1477 (2004).
108. Burrows, E.L. et al. Social Isolation Alters Social and Mating Behavior in the R451C Neuroligin Mouse Model of Autism. *Neural Plast* **2017**, 8361290 (2017).
109. Liu, J.J. et al. Neuroligin 3 R451C mutation alters electroencephalography spectral activity in an animal model of autism spectrum disorders. *Mol Brain* **10**, 10 (2017).
110. Fantuzzo, J.A. et al. Intellicount: High-Throughput Quantification of Fluorescent Synaptic Protein Puncta by Machine Learning. *eNeuro* **4** (2017).
111. Tsai, N.P. et al. Multiple autism-linked genes mediate synapse elimination via proteasomal degradation of a synaptic scaffold PSD-95. *Cell* **151**, 1581-1594 (2012).
112. Sekar, A. et al. Schizophrenia risk from complex variation of complement component 4. *Nature* **530**, 177-183 (2016).
113. Südhof, T.C. Neuroligins and Neurexins Link Synaptic Function to Cognitive Disease. *Nature* **455**, 903-911 (2008).
114. Ko, J., Fuccillo, M.V., Malenka, R.C. & Sudhof, T.C. LRRTM2 functions as a neurexin ligand in promoting excitatory synapse formation. *Neuron* **64**, 791-798 (2009).
115. Lee, K. et al. MDGAs interact selectively with neuroligin-2 but not other neuroligins to regulate inhibitory synapse development. *PNAS* **110**, 336-341 (2013).
116. Zhang, B. et al. Neuroligins Sculpt Cerebellar Purkinje-Cell Circuits by Differential Control of Distinct Classes of Synapses. *Neuron* **87**, 781-796 (2015).
117. Chen, L.Y., Jiang, M., Zhang, B., Gokce, O. & Sudhof, T.C. Conditional Deletion of All Neurexins Defines Diversity of Essential Synaptic Organizer Functions for Neurexins. *Neuron* **94**, 611-625 e614 (2017).
118. El-Husseini, A.E.-D., Schnell, E., Chetkovich, D.M., Nicoll, R.A. & Bredt, D.S. PSD-95 Involvement in Maturation of Excitatory Synapses. *Science* **290**, 1364-1368 (2000).
119. Schatzle, P., Wuttke, R., Ziegler, U. & Sonderegger, P. Automated quantification of synapses by fluorescence microscopy. *J Neurosci Methods* **204**, 144-149 (2012).
120. Danielson, E. & Lee, S.H. SynPAnal: software for rapid quantification of the density and intensity of protein puncta from fluorescence microscopy images of neurons. *PLoS One* **9**, e115298 (2014).
121. Ippolito, D.M. & Eroglu, C. Quantifying synapses: an immunocytochemistry-based assay to quantify synapse number. *J Vis Exp* (2010).
122. Saccone, S.F. et al. Cholinergic nicotinic receptor genes implicated in a nicotine dependence association study targeting 348 candidate genes with 3713 SNPs. *Hum Mol Genet* **16**, 36-49 (2007).
123. Bierut, L.J. et al. Variants in nicotinic receptors and risk for nicotine dependence. *Am J Psychiatry* **165**, 1163-1171 (2008).

124. Chanda, S., Hale, W.D., Zhang, B., Wernig, M. & Sudhof, T.C. Unique versus Redundant Functions of Neuroligin Genes in Shaping Excitatory and Inhibitory Synapse Properties. *J Neurosci* **37**, 6816-6836 (2017).
125. Maximov, A., Pang, Z.P., Tervo, D.G. & Sudhof, T.C. Monitoring synaptic transmission in primary neuronal cultures using local extracellular stimulation. *J Neurosci Methods* **161**, 75-87 (2007).
126. Schindelin, J. et al. Fiji: an open-source platform for biological-image analysis. *Nat Methods* **9**, 676-682 (2012).
127. Otsu, N. A Threshold Selection Method from Gray-Level Histograms. *IEEE TRANSACTIONS ON SYSTEMS, MAN, AND CYBERNETICS,* **SMC-9**, 62-66 (1979).
128. Ribrault, C., Sekimoto, K. & Triller, A. From the stochasticity of molecular processes to the variability of synaptic transmission. *Nat Rev Neurosci* **12**, 375-387 (2011).
129. Siksou, L. et al. Three-dimensional architecture of presynaptic terminal cytomatrix. *J Neurosci* **27**, 6868-6877 (2007).
130. Mitchell, N. et al. Sonic hedgehog regulates presynaptic terminal size, ultrastructure and function in hippocampal neurons. *J Cell Sci* **125**, 4207-4213 (2012).
131. Sobel, I. in Machine Vision for Three-Dimensional Scenes. (ed. A. Press) 376-379 (1990).
132. Patzke, C., Acuna, C., Giam, L.R., Wernig, M. & Sudhof, T.C. Conditional deletion of L1CAM in human neurons impairs both axonal and dendritic arborization and action potential generation. *J Exp Med* **213**, 499-515 (2016).
133. Pak, C. et al. Human Neuropsychiatric Disease Modeling using Conditional Deletion Reveals Synaptic Transmission Defects Caused by Heterozygous Mutations in NRXN1. *Cell Stem Cell* **17**, 316-328 (2015).
134. Yi, F. et al. Autism-associated SHANK3 haploinsufficiency causes Ih channelopathy in human neurons. *Science* **352**, aaf2669 (2016).
135. Mozhayeva, M.G., Sara, Y., Liu, X. & Kavalali, E.T. Development of Vesicle Pools during Maturation of Hippocampal Synapses. *The Journal of Neuroscience* **22**, 654-665 (2002).
136. Cullen, D.K., Gilroy, M.E., Irons, H.R. & Laplaca, M.C. Synapse-to-neuron ratio is inversely related to neuronal density in mature neuronal cultures. *Brain Res* **1359**, 44-55 (2010).
137. Carpenter, A.E., Kamentsky, L. & Eliceiri, K.W. A call for bioimaging software usability. *Nat Methods* **9**, 666-670 (2012).
138. Ichikawa, M., Muramoto, K., Kobayashi, K., Kawahara, M. & Kuroda, Y. Formation and maturation of synapses in primary cultures of rat cerebral cortical cells: an electron microscope study. *Neuroscience Research* **16**, 95-103 (1993).
139. Nikodem, J. Plateau Problem in the Watershed Transform. *Computing and Informatics* **28**, 1001-1013 (2009).
140. Gibson, D.G. et al. Enzymatic assembly of DNA molecules up to several hundred kilobases. *Nat Methods* **6**, 343-345 (2009).
141. Taylor, A.M. & Jeon, N.L. Microfluidic and Compartmentalized Platforms for Neurobiological Research. *Critical Reviews in Biomedical Engineering* **39**, 185-200 (2011).
142. Deleglise, B. et al. Synapto-protective drugs evaluation in reconstructed neuronal network. *PLoS One* **8**, e71103 (2013).

143. Darville, H. et al. Human Pluripotent Stem Cell-derived Cortical Neurons for High Throughput Medication Screening in Autism: A Proof of Concept Study in SHANK3 Haploinsufficiency Syndrome. *EBioMedicine* **9**, 293-305 (2016).
144. Desbordes, S.C. & Studer, L. Adapting human pluripotent stem cells to high-throughput and high-content screening. *Nat Protoc* **8**, 111-130 (2013).
145. McNeish, J. et al. High-throughput screening in embryonic stem cell-derived neurons identifies potentiators of alpha-amino-3-hydroxyl-5-methyl-4-isoxazolepropionate-type glutamate receptors. *J Biol Chem* **285**, 17209-17217 (2010).
146. Theodorou, E. et al. A high throughput embryonic stem cell screen identifies Oct-2 as a bifunctional regulator of neuronal differentiation. *Genes Dev* **23**, 575-588 (2009).
147. Ray, L.A. et al. The role of the Asn40Asp polymorphism of the mu opioid receptor gene (OPRM1) on alcoholism etiology and treatment: a critical review. *Alcohol Clin Exp Res* **36**, 385-394 (2012).
148. Le Foll, B., Gallo, A., Le Strat, Y., Lu, L. & Gorwood, P. Genetics of dopamine receptors and drug addiction: a comprehensive review. *Behav Pharmacol* **20**, 1-17 (2009).
149. Chen, L.S. et al. Genetic variation (CHRNA5), medication (combination nicotine replacement therapy vs. varenicline), and smoking cessation. *Drug Alcohol Depend* **154**, 278-282 (2015).
150. Jensen, K.P. et al. A CHRNA5 Smoking Risk Variant Decreases the Aversive Effects of Nicotine in Humans. *Neuropsychopharmacology* **40**, 2813-2821 (2015).
151. Ramsay, J.E., Rhodes, C.H., Thirtamara-Rajamani, K. & Smith, R.M. Genetic influences on nicotinic alpha5 receptor (CHRNA5) CpG methylation and mRNA expression in brain and adipose tissue. *Genes Environ* **37**, 14 (2015).
152. Smith, R.M. et al. Nicotinic alpha5 receptor subunit mRNA expression is associated with distant 5' upstream polymorphisms. *Eur J Hum Genet* **19**, 76-83 (2011).
153. Pitchers, K.K. et al. Natural reward experience alters AMPA and NMDA receptor distribution and function in the nucleus accumbens. *PLoS One* **7**, e34700 (2012).
154. Wolf, J.A. et al. NMDA/AMPA ratio impacts state transitions and entrainment to oscillations in a computational model of the nucleus accumbens medium spiny projection neuron. *J Neurosci* **25**, 9080-9095 (2005).
155. Mathon, D.S. et al. Increased gabaergic input to ventral tegmental area dopaminergic neurons associated with decreased cocaine reinforcement in mu-opioid receptor knockout mice. *Neuroscience* **130**, 359-367 (2005).